First–Principles Investigation of Li Intercalation Kinetics in Phospho–Olivines

by

Rahul Malik
B.Sc., Cornell University (2007)

Submitted to the Department of Materials Science and Engineering
in Partial Fulfillment of the Requirements for the Degree of

Doctor of Philosophy

at the

MASACHUSETTS INSTITUTE OF TECHNOLOGY

June 2013

Signature of Author .....
Department of Materials Science and Engineering
March 2013

Certified by .....
Gerbrand Ceder
R.P. Simmons Professor of Materials Science and Engineering
Thesis Supervisor

Accepted by .....
Gerbrand Ceder
Chair, Departmental Committee on Graduate Students

Abstract

This thesis focuses broadly on characterizing and understanding the Li intercalation mechanism in phospho–olivines, namely $LiFePO_4$ and $Li(Fe,Mn)PO_4$, using first-principles calculations. Currently Li–ion battery technology is critically relied upon for the operation of electrified vehicles, but further improvements mainly in cathode performance are required to ensure widespread adoption, which in itself requires learning from existing commercial cathode chemistries. $LiFePO_4$ is presently used in commercial Li–ion batteries, known for its rapid charge and discharge capability but with underwhelming energy density. This motivates the three central research efforts presented herein.

First, we investigate the modified phase diagram and electrochemical properties of mixed olivines, such as $Li(Fe,Mn)PO_4$, which offer improved theoretical energy density over $LiFePO_4$ (due to the higher redox voltage associated with Mn^{2+}/Mn^{3+}). The $Li_x(Fe_{1-y}Mn_y)PO_4$ phase diagram is constructed by Monte Carlo simulation on a cluster expansion Hamiltonian parametrized by first–principles determined energies. Deviations from the equilibrium phase behavior and voltages of pure $LiFePO_4$ and $LiMnPO_4$ are analyzed and discussed to good agreement with experimental observations.

Second, we address why $LiFePO_4$ exhibits superior rate performance strictly when the active particle size is brought down to the nano-scale. By considering the presence of immobile point defects residing in the 1D Li diffusion path, specifically by calculating from first principles both defect formation energies and Li migration barriers in the vicinity of likely defects, the Li diffusivity is recalculated and is found to strongly vary with particle size. At small particle sizes, the contribution from defects is small, and fast 1D Li diffusion is accessible. However, at larger particle sizes (μm scale and above) the contribution from defects is much larger. Not only is Li transport impeded, but it is also less anisotropic in agreement with experiments on large $LiFePO_4$ single crystals.

Third, we investigate why $LiFePO_4$ can be charged and discharged rapidly despite having to undergo a first–order phase transition. Conventional wisdom dictates that a system with strong equilibrium Li segregation behavior requires both nucleation and growth in the charge and discharge process, which should impede the overall kinetics. Rather, through first-principles calculations, we determine the minimal energy required to access a non-equilibrium transformation path entirely through the solid solution. Not only does this transformation mechanism require little driving force, but it also rationalizes how a kinetically favorable but non-equilibrium path is responsible for the extremely high rate performance associated with this material. The consequences of a rapid non-equilibrium single-particle transformation mechanism on (dis)charging a multi-particle assembly, as is the case in porous electrodes, are discussed and compared to experimental observations.

Thesis Supervisor: Gerbrand Ceder
Title: R.P. Simmons Professor of Materials Science and Engineering

Acknowledgments

I owe many thanks and much appreciation to everyone who helped me throughout graduate school, to those who helped contribute directly to this work and also to those who helped support me along the way. I received a lot of help.

To my parents and sister whose unwavering support over the years kept me afloat, I am proud to join you and make us a family of doctors, and I am especially proud to continue alongside Dad in materials science.

This thesis is the detailed development of just a few of the many ideas seeded by my adviser, Professor Gerbrand Ceder. Over the past several years I have had the privilege to see Gerd in action, generating and communicating ideas on the fly in group meeting, delivering lectures with enthusiasm, and above all generously setting aside time to discuss research with his students. It is always encouraging to work with inspired individuals, and in my time at MIT, there has been no shortage of inspiration in the Ceder Group.

To my research group, I am especially proud to have a place in our lineage, working alongside inspiring and patient mentors and emerging scientific minds. Two mentors in particular, Fei Zhou and Lei Wang, made a significant impact by not only motivating this work with their own scientific contributions (see references),

but also providing indispensible individual advice and guidance. Also, fruitful discussions with Byoungwoo Kang helped me navigate through the experimental literature and integrate theory and modeling with experiment design. Aziz Abdellahi (who joined the group two years after me) was an invaluable resource for his coding expertise and as a sounding board for ideas both scientific and otherwise. My officemates made 13-5025 a collegial and warm environment, and Kathy made the group operate seamlessly.

I consider myself to be incredibly lucky not only for the opportunity to work at a world–class institution like MIT, but also to establish roots in a community of world–class people. Over the past six years, I have relied heavily on the continual support of friends, and our shared memories are the ones I will revisit the most: Cabin Trips in the summer and P–Day Ski Trips in the winter, 4th of July on the Charles on a home-made pontoon with 30 or so of us, BAMF porch sessions, impromptu parking lot snow-cave building during winter storm Nemo, a 37 hour round-trip to Puerto Rico, and evening brainstorming and battery discussions (Triple B's) to name a short few. Above all, I am grateful that you all made my grad school experience a complete one.

Table of Contents

Abstract 3

Introduction to Li-ion Batteries for Electrified Vehicles 11

Motivation and Application 11

Li-ion Battery Components 12

Porous Electrodes 13

Operation 14

Chapter 1: $LiFePO_4$ Background 19

1.1 Crystal Structure, Voltage, and Safety 20

1.2 Bulk and Single-Particle Thermodynamics 23

1.2.1 Bulk Thermodynamics of the Li_xFePO_4 System 23

1.2.2 Bulk Thermodynamics of the Li–Fe–P–O System 27

1.2.3 Equilibrium Within a Single Li_xFePO_4 Nanoparticle 29

1.3 Bulk Kinetics 33

1.3.1 Bulk Li Diffusivity 34

1.3.2 Electronic Conductivity 36

1.4 $LiFePO_4$ Phase Transformation Models 43

1.4.1 Isotropic Two–Phase Models 45

1.4.2 Anisotropic Two–Phase Models 46

1.4.3 Dynamic Amorphization 56

1.5 Remaining Questions 58

Chapter 2: Methods 59

2.1 Ground-State Energies from Density Functional Theory 59

2.2 Cluster Expansion 61

2.3 Monte Carlo Methods 63

2.4 Experimental Agreement 64

Chapter 3: Phase Diagram and Electrochemical Properties of Mixed Olivines from First–Principles Calculations 67

3.1 Methods 68

3.2 Results 70

3.3 Discussion 76

3.3.1 Existence of Single Phase Region 78

3.3.2 Increasing transition voltage 80

3.3.3 Reduced Polarization 81

3.3 Conclusions 82

3.5 Appendix: Determining Voltage Shifts in Mixed Olivines 83

Chapter 4: Particle Size Dependence of the Ionic Diffusivity 85

4.1 1D Diffusion and Li Transport in $LiFePO_4$ 86

4.2 Point Defects and Blocked Capacity 88

4.3 Li Cross-over and Effects on Bulk Li Diffusivity 91

4.4 Particle Size Dependence 94

4.5 Conclusions: Why nano–$LiFePO_4$ performs better 95

4.6 Appendices 97

4.6.1 Defect Formation Energies 97

4.6.2 Unblocked Capacity in $LiFePO_4$ Channels Containing Defects 99

4.6.3 Crossover Migration Path 101

4.6.4 1D Random Walk Model 102

Chapter 5: Kinetics of Non-equilibrium Li Insertion in $LiFePO_4$ 105

5.1 Background 106

5.2 Non–equilibrium Solid–Solution Free Energy Calculation 107

5.3 Effect on Electrochemical Charging and Discharging 110

5.4 Conclusions 115

Chapter 6: Implications and Future Work 117

6.1 Equilibrium in a Multi–Particle Assembly 117

6.2 Electrode-Scale (de)lithiation 125

6.2.1 Carbon Coating 127

6.2.2 Ionically Conductive Coatings 128

6.2.3 Electrode Thickness and Dilution 129

6.3 Electrode-Scale Inhomogeneity 131

Conclusions 137

References 141

Introduction to Li-ion Batteries for Electrified Vehicles

Motivation and Application

The vast majority of U.S. greenhouse gas (GHG) emissions come from the combustion of fossil fuels, contributing nearly 87% (5,388 Tg CO_2 equivalent) to all GHG emissions in 2010 according to a study conducted by U.S. Environmental Protection Agency (EPA).[1] Of that, electricity generation and transportation accounted for 2,258 and 1,745 Tg CO_2 equivalent, respectively. To the first issue, renewable energy sources (i.e. solar, wind, etc.) offer the potential to displace the emissions produced from electricity generation, but to address the emissions produced from transport will require the advent of an adequate energy storage and conversion technology that not only avoids petroleum combustion, but also is compatible with the oncoming renewable energy-generating infrastructure. Today, vehicles powered entirely or in part by Li–ion batteries have come to the forefront as the likeliest technology to fill this societal need, with nearly every major auto manufacturer now producing or planning to produce some form of Li–ion battery powered vehicle.[2] Nevertheless, widespread adoption of electrified vehicles will remain difficult without additional significant improvement in battery performance.

Li-ion Battery Components

In its most general form, a rechargeable battery is a device capable of storing energy through reversibly converting chemical to electrical energy and is comprised of three main components: the cathode, anode, and electrolyte (shown below in **Figure 1**).

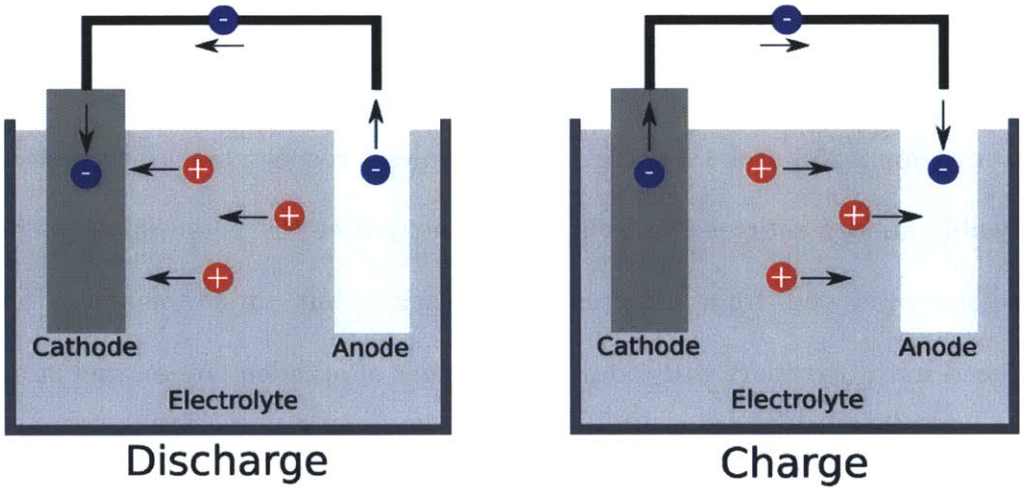

Figure 1: Schematic Illustration of Battery Components and Operation

In today's commercial Li-ion batteries, typically the active cathode material is a ceramic Li transition metal oxide or phosphate (e.g. $LiCoO_2$, $Li(Ni,Mn,Co)O_2$, $Li(Ni,Co,Al)O_2$, $LiMn_2O_4$, or $LiFePO_4$), the electrolyte a Li salt (e.g. $LiPF_6$) dissolved in an organic solvent (e.g. EC/DMC), and the anode graphitic carbon. Both the cathode and anode are Li intercalation materials, which can reversibly incorporate and remove Li from their host crystal structure, but when the Li is in the anode (and the cathode is free of Li), the system energy is higher than when the Li is in the cathode (and the anode is free of Li). This describes the *charged* and *discharged* states, respectively. To extract that energy difference as electricity requires the

presence of an electrolyte, which is a connecting medium between cathode and anode that conducts Li^+ ions but *not* electrons (shown in red and blue, respectively, in **Figure 1**), unlike anode and cathode which must conduct both.

Porous Electrodes

In practice, the Li-ion electrochemical cell architecture is more involved than that described in **Figure 1**. The electrode is usually a porous composite of the active electrode material (typically in powder form), binder (e.g. PVDF, which holds together the active material), and potentially non-active additives (e.g. carbon black, which can be used to improve the electronic conductivity across the electrode) interpenetrated by the electrolyte. Physically, the anode and cathode are now separated by a porous polymeric material (e.g. polyethylene) called a separator. An illustration of a typical Li–ion cell with porous electrode architecture is shown below in **Figure 2**. Half-cells are preferred in lab-scale experiments designed to isolate

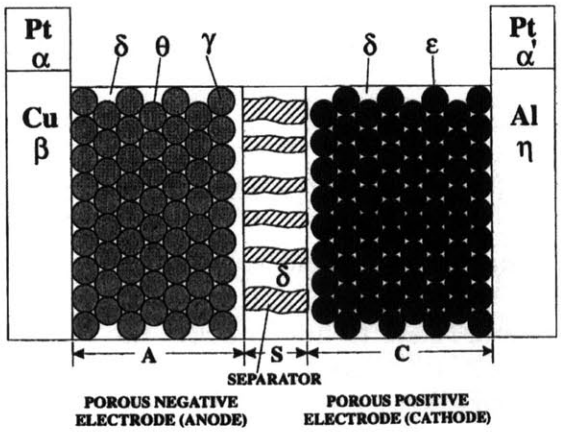

α	Platinum phase (solid) as the anode lead
β	Copper phase (solid), e.g. thin copper foil, as the anode current collector
γ	Anode graphite, Li_xC_6, solid phase particles
δ	Electrolytic solution of a salt (e.g. $LiPF_6$) in an organic solvent (e.g. ethylene carbonate (EC)) or in a mixture of organic solvents (e.g. ethylene carbonate (EC) and dimethyl carbonate (DMC))
S	Microporous polyethylene separator containing electrolytic solution
ϵ	Cathode, $Li_{1-x}MO_2$ (M = Co or Ni), solid phase particles
η	Aluminum phase (solid) as the cathode current collector, for example, thin aluminum foil
α'	Platinum phase (solid) as the cathode lead
θ	Compact, highly passivating and stable film

Figure 2: Schematic Illustration of Li–ion Cell with Porous Electrode Architecture

and characterize cathode performance, and the anode material (typically graphite) is replaced by a Li–metal foil, which remains at constant potential during operation.

Operation

In discharge, Li travels from anode (Li metal) to cathode (Li_xFePO_4 in this work, where $0 \leq x \leq 1$) as described schematically in **Figure 1**. The design feature of separate migration paths to the counter-electrode for Li^+ through the electrolyte and electrons (e^-) through an external circuit (powering a vehicle, for instance) is what facilitates conversion of chemical to electrical energy. The charging process, where electrical energy is converted back to chemical energy, is simply the discharge process in reverse (also described in **Figure 1**). The overall reaction for a $LiFePO_4$ half–cell can be described as follows, where the forward reaction describes discharging and the backward reaction describes charging:

$$x\mathbf{Li}_{metal} + \mathbf{FePO_4} \rightleftharpoons \mathbf{Li_xFePO_4}. \qquad (1)$$

Successful operation of a Li–ion battery (for electrified vehicles) requires a number of interrelated properties to be simultaneously optimized: *energy density* (by mass and volume), *specific power*, *safety*, *cycle life*, and *cost*. The energy density, which determines the electric vehicle's driving range, depends on two main components, the capacity (i.e. how much Li can be stored) and voltage V (i.e. how much energy is stored per Li), and specific power refers to how quickly the energy stored can be converted. Currently, the bottleneck to improved performance in commercial Li–ion batteries resides on the cathode side, which limits both energy

density and assumes a significant portion of cell cost. Moreover, it is largely the materials properties of the active cathode material that dictate the overall performance of the entire Li–ion battery, which therefore frames the problem of improving Li–ion battery performance as specifically a materials science problem.

For instance, the voltage V is coupled to the lithium chemical potential μ_{Li} because the number of electrons that pass through the external circuit (as shown in **Figure 1**) must be identical to the number of Li^+ passing through the electrolyte. This is readily apparent when considering the entire cell at equilibrium, defined by

$$dg^{cell} = 0, \tag{2}$$

and since the electrolyte remains unchanged before and after (dis)charge (in theory), the cell free energy g^{cell} can be separated into

$$dg^{cathode} + dg^{anode} = 0. \tag{3}$$

At constant temperature T, the relevant formulation of the free energy is

$$(\mu_{Li}^{cathode} \cdot dn_{Li}^{cathode} + \phi^{cathode} \cdot dq^{cathode}) + (\mu_{Li}^{anode} \cdot dn_{Li}^{anode} + \phi^{anode} \cdot dq^{anode}) = 0, \tag{4}$$

where n_{Li} refers to the number of moles of Li, Φ is electric potential, and q is electric charge. Remarking that the imposition of the electrolyte ensures that

$$dq^{cathode} = -z \cdot e \cdot dn_{Li}^{cathode} \text{ and } dq^{anode} = -z \cdot e \cdot dn_{Li}^{anode}, \tag{5}$$

where z is the amount of charge transported by Li^+ (i.e., $z = 1$) and e is the charge possessed by an electron. Rearranging the terms in *(4)* reveals

$$[(\mu_{Li}^{anode} - \mu_{Li}^{cathode}) - (\phi^{anode} - \phi^{cathode})]dn_{Li}^{anode} = 0. \tag{6}$$

Therefore, under the condition of equilibrium, the difference in Li chemical potential is directly related to the difference in electrical potential between the anode and cathode (otherwise known as the voltage *V*):

$$\boxed{\Delta\mu_{Li} = -V \text{ (in eV/atom).}} \qquad (7)$$

Given that the cell voltage and capacity are materials properties, **Table 1** lists the average voltage, theoretical capacity, theoretical specific energy, and actual specific energy associated with some of the major commercial Li–ion battery cathode chemistries.

Cathode Material	Voltage (vs. Li metal)	Theoretical Capacity	Theoretical Specific Energy	Actual Specific Energy
$LiCoO_2$	~ 4 V	~ 270 mAh/g	~ 1100 Wh/kg	~ 500 Wh/kg
$LiMn_2O_4$	~ 4 V	~ 150 mAh/g	~ 600 Wh/kg	~ 400 Wh/kg
$LiFePO_4$	***~ 3.4 V***	***~ 170 mAh/g***	***~ 580 Wh/kg***	***~ 500 Wh/kg***

Table 1: Voltages, Capacities, and Specific Energies of Selected Commercial Li–ion Cathode Chemistries

Whereas the energy density is dictated by the Li chemical potential difference between the charged and discharged states (and the capacity), the spatial gradient of μ_{Li} across the electrode as well as the electrode's ionic and electronic conductivity dictate the Li insertion and de–insertion kinetics, which determine not only the specific power delivered in discharge but also the battery recharging time. Because charging and discharging are dynamic and path-dependent processes, characterizing the Li–insertion kinetics is a more involved task than determining the theoretical energy density (which can be determined strictly from equilibrium

materials properties). Although there are other parameters at play, such as cost, safety, and cycle life as discussed earlier, specific energy must be improved without sacrificing power in order for Li–ion batteries to be feasible in both plug–in hybrid (PHEV) and fully electric vehicles (EVs) as seen in **Figure 3**.

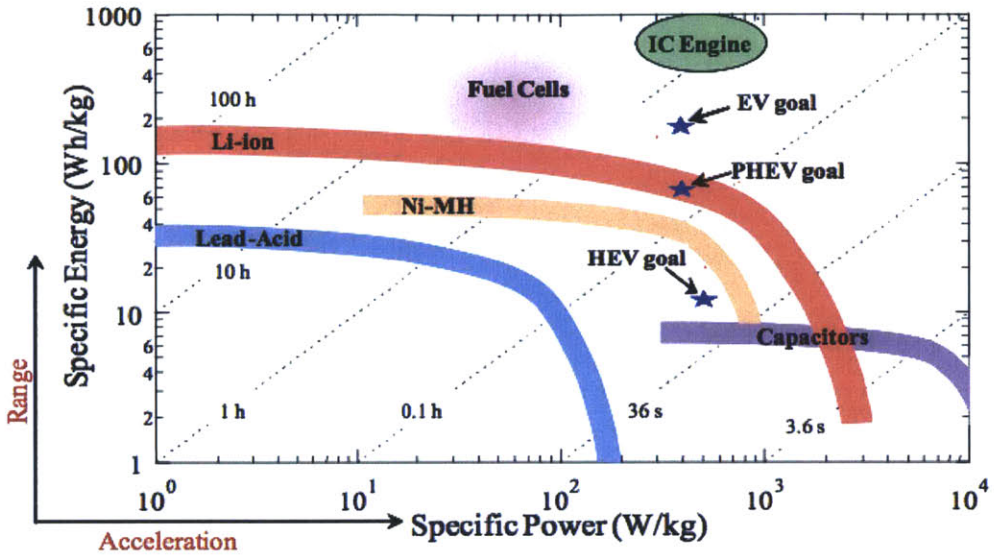

Figure 3: Specific Energy vs. Specific Power Across Different Energy Storage Technologies

If the performance of intercalation cathode chemistries is to improve, whether through modifying or designing new materials, the *mechanism* of Li–insertion kinetics must be adequately understood, and $LiFePO_4$ represents a compelling and illustrative example.

Chapter 1: $LiFePO_4$ Background

Since the initial work in 1997,[3] over 2100 research publications have been authored on lithium iron phosphate ($LiFePO_4$), one of only a handful of commercially viable Li-ion battery cathode materials currently used in electrified vehicles. The now well-known excellent rate performance of the material,[4] however, has been demonstrated only in the years following, defying the initial claim that $LiFePO_4$ would be strictly relegated to low-rate applications[3] because of kinetic barriers associated with propagating a two-phase interface within an active particle (discussed in detail in future sections). Despite the sheer quantity of research devoted to the subject and the well-demonstrated excellent battery performance of $LiFePO_4$,[4] what *is* surprising are the number of apparent discrepancies and ensuing contention in the literature regarding its (de)lithiation kinetics. The question now strays from *can* $LiFePO_4$ be a high-rate battery material, to *why*? The first step toward answering this question and developing a complete picture of lithiation intercalation kinetics within a $LiFePO_4$ composite electrode lies in understanding the nuances of the Li_xFePO_4 ($0 < x < 1$) system equilibrium itself.

1.1 Crystal Structure, Voltage, and Safety

Before the initial work on $LiFePO_4$ in 1997,[3] the known commercial and widely studied Li–insertion cathode materials were transition metal oxides such as $LiCoO_2$ and $LiMn_2O_4$, which crystallize in the layered and spinel structures, respectively. $LiFePO_4$ (also known as triphylite), alternatively, forms in the ordered olivine structure, with orthorhombic unit cell and *Pnma* symmetry, and has a theoretical capacity of 170 mAh/g as shown below in **Figure 4**.

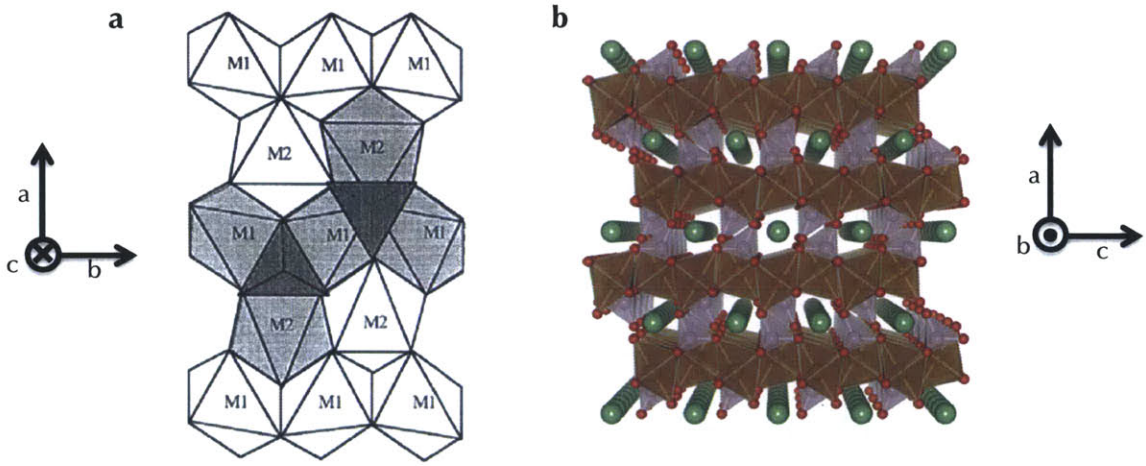

Figure 4: $LiFePO_4$ Crystal Structure. (a) Distorted HCP oxygen anion sub–lattice oriented along *ab* plane. (b) Li channels (green) oriented along *b* direction (into the page) within the $FePO_4$ host structure (red, brown and purple atoms correspond to O, Fe, and P, respectively).

The oxygen anions reside on a distorted hexagonal close-packed (HCP) sub-lattice, with the hexagonal sheets contained in the *ab* plane and the stacking direction oriented along the *c* direction as seen in **Figure 4a**.[3] The interstitial sites are occupied by phosphorus cations on $1/8^{th}$ of the tetrahedral sites and lithium and iron cations occupying half of the octahedral sites. The distortion in the oxygen framework forms two distinct octahedral sites of varying size, with the smaller site (called the M1 site) occupied by Li, forming 1D chains of edge-sharing LiO_6

octahedra along the *b* direction shown in **Figure 4b**, and the larger site occupied by Fe (called the M2 site), forming 2D sheets of corner-sharing FeO_6 octahedra in the *bc* plane. The PO_4 groups each share two edges with LiO_6 octahedra and one with FeO_6 octahedra.

Each orthorhombic $LiFePO_4$ unit cell contains four formula units, with lattice parameters $a = 10.33\ A$, $b = 6.01\ A$, $c = 4.69\ A$ ($V = 291.4\ A^3$, $\rho = 3.6$ g/cm^3), and its delithiated form $FePO_4$ (also known as heterosite) is isostructural with lattice parameters $a = 9.82\ A$, $b = 5.79\ A$, $c = 4.79\ A$ ($V = 272.4\ A^3$, $\rho = 3.85$ g/cm^3), accounting for a 6.81% volume reduction and 2.59% density increase upon a full charge.[5] Olivine $LiFePO_4$ is thermodynamically stable at room temperature and up to temperatures higher than 800°C,[6] but olivine $FePO_4$ has been reported to be metastable at room temperature, informed by an irreversible phase transformation to a trigonal phase (berlinite) observed upon heating but not observed upon cooling beginning at 580°C.[7] First principles calculations confirm that the berlinite $FePO_4$ polymorph is the most stable at ambient pressure,[8] in apparent disagreement, however, with formation enthalpies calculated using high-temperature oxide melt solution calorimetry, which suggest the opposite, that the orthorhombic olivine phase is the most stable at room temperature and that the phase transformation not observed upon cooling from high temperature is simply impeded by slow kinetics. The excellent cycling performance of $LiFePO_4$ and reversibility of Li intercalation are in part attributed to not only the phase stability of the two end-members but also the modest structural change upon charge and discharge.[3] Also,

$LiFePO_4$ and $FePO_4$ do not decompose or react perniciously with commonly used electrolytes at temperatures up to 85°C, and exothermic decomposition of the charged state ($FePO_4$) combined with oxygen evolution (leading to uncontrolled exothermic reaction with the electrolyte thus compromising cell safety) is not observed in conventional operating conditions.

Reversible Li intercalation into Li_xFePO_4 occurs at an average voltage of ~ 3.4 V with respect to metallic lithium (Li^+/Li^0), which yields theoretical energy densities of ~ 580 Wh/kg (by mass) and volumetric energy density of ~ 2100 Wh/L (by volume). On a nominal basis, $LiFePO_4$ has higher gravimetric energy density than both $LiCoO_2$ and $LiMn_2O_4$, and higher volumetric energy density than $LiMn_2O_4$ but lower than $LiCoO_2$. Compared to transition metal oxides, structures with oxygen anions replaced by polyanionic structures (such as PO_4^{3-}) have higher voltages for an identical metal redox couple, a general phenomenon known as the inductive effect.[5] In $LiFePO_4$, this arises from oxygen anions commonly bonded to both Fe and P. The covalency of the Fe–O bond is reduced from the attraction of the oxygen anion's electrons to the phosphorus cation, which reduces the Fe^{2+}/Fe^{3+} redox energy and consequently raises the voltage. Also, because the PO_4^{3-} group hybridizes less with the Fe cation compared to an oxygen anion, the *3d* electron states are more localized on the Fe sublattice compared to oxides.

Cathode materials of the form $LiMPO_4$ (M= Mn, Co, Ni), which also share the ordered olivine structure, potentially offer higher energy densities than $LiFePO_4$ from the prospect of accessing a higher voltage redox couple, 4.1 V, 4.8 V, and 5.1 V

versus Li^+/Li^o for $Mn^{2+/3+}$, $Co^{2+/3+}$, and $Ni^{2+/3+}$, respectively, while retaining nearly identical theoretical capacities (167 – 170 mAh/g).[9-12] Unfortunately, these materials suffer either from poorer intercalation kinetics or thermal stability compared to $LiFePO_4$, and in particular, the lithiation voltage of $LiCoPO_4$ and $LiNiPO_4$ exceeds the stability window of many common organic electrolytes, all of which are current impediments preventing widespread use. In the case of Li_xMnPO_4, the presence of octahedrally coordinated Mn^{3+} with high-spin $3d$ electron configuration induces local lattice distortion to break symmetry and eliminate degeneracy thereby lowering the energy, which is known as the Jahn-Teller effect. The local distortion can assume different orientations and involves the lengthening of a pair of Mn–O bonds and the constriction of two pairs of Mn–O bonds in $MnPO_4$.[13] Many studies invoke the effect of Jahn-Teller distortions in Li_xMPO_4 as responsible for the varied electrochemical performance compared to $LiFePO_4$.

1.2 Bulk and Single-Particle Thermodynamics

1.2.1 Bulk Thermodynamics of the Li_xFePO_4 System

Perhaps the defining feature of the Li_xFePO_4 system is the strong room-temperature Li phase separation with negligible Li solubility in the end-member phases (heterosite and triphylite). In accordance with Gibbs' phase rule, which stipulates that there can be zero degrees of freedom in the intensive variables in the two-phase regime of a two-component system (given fixed pressure and temperature), this gives rise to the characteristic flat room-temperature voltage

curve ubiquitous in the literature, illustrated in **Figure 5**. Of all the commercially functioning Li battery cathode materials, $LiFePO_4$ is unique to having this property – $LiCoO_2$, $LiMn_2O_4$,[14] $Li(Ni,Co,Al)O_2$, and $Li(Ni,Co,Mn)O_2$ all form solid solutions over a wide concentration range, and if present at all, first-order phase transitions are weak arising from either Li ordering or electronic effects.[15]

Thorough experimental and computational characterizations of the bulk Li composition–temperature binary phase diagram (shown in **Figure 6**) also reveal the existence of a solid-solution phase which emerges through a eutectoid transition

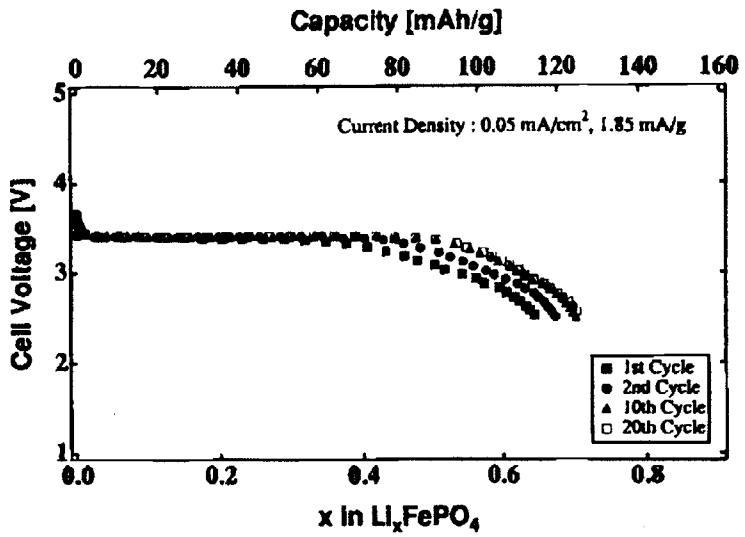

Figure 5: Discharge/charge curves vs. lithium at 2.0 mA/g (0.05 mA/cm²) for Li_xFePO_4 obtained by Padhi *et al.*

(at ~ 400 – 500 K, x_{Li} ~0.4 – 0.6). The complex high T behavior of the system arises from the unique contribution of the electron configurational entropy which stabilizes the solid-solution phase. In a conventional binary 'miscibility gap'–type system, interactions between unlike species (i.e. Li and vacancy) are purely repulsive, which encourages like species to pool together, but in Li_xFePO_4 the

presence of localized 3*d* electrons[16,17] (i.e. e^-/Fe^{2+} or h^+/Fe^{3+}) on the transition metal sub-lattice complicates matters. To accurately model the finite-temperature phase behavior of Li_xFePO_4, both the ionic and electronic degrees of freedom must be explicitly considered. At low temperatures (below the eutectoid point), strong attractive interactions between Li^+ and e^- (Fe^{2+}) overcome repulsive Li^+–Li^+ and e^-–e^- interactions, overall stabilizing the phase separated state. The e^- (Fe^{2+}) effectively acts as the "glue" between the Li^+ ions. The combined effect of strong

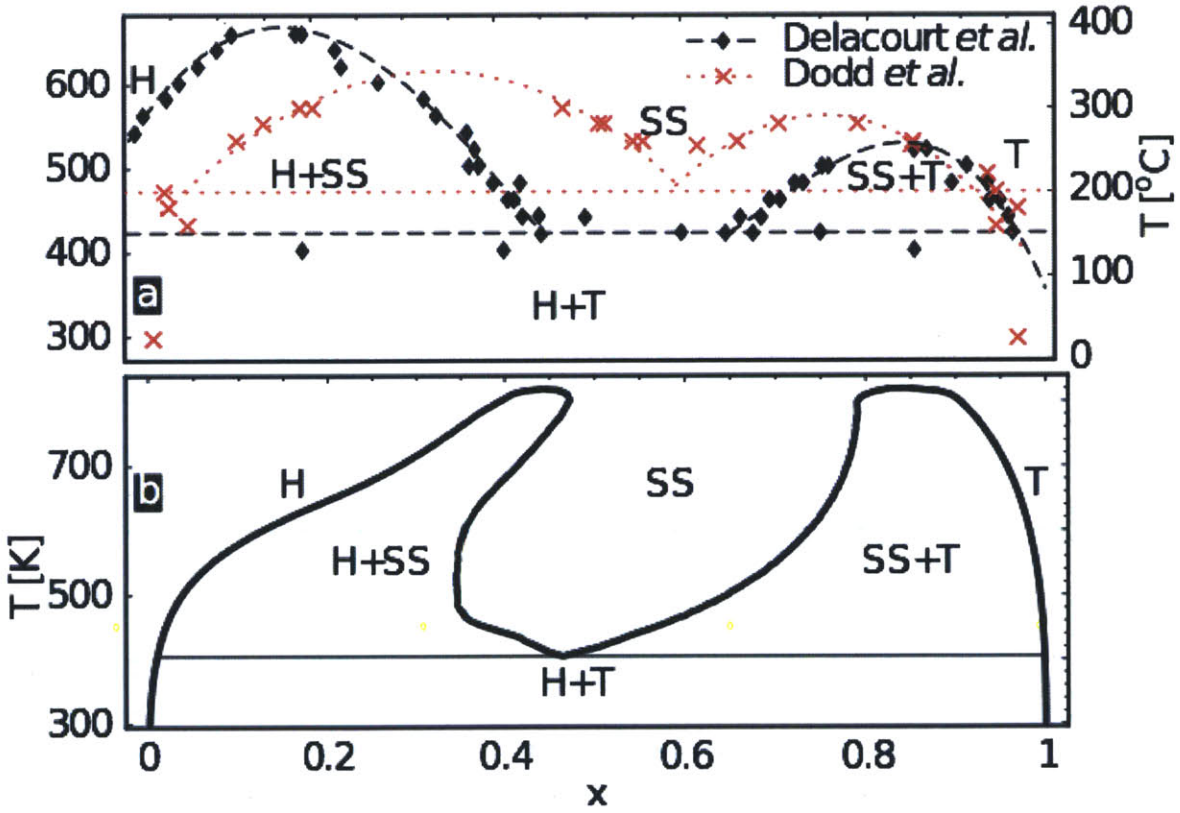

Figure 6: Bulk Li_xFePO4 phase diagram as determined by (a) experimentally by Dodd *et al.* (ref. 30) and Delacourt *et al.* (ref. 29) and (b) computationally by Zhou *et al.* (ref 31)

attractive Li^+–e^- interactions and the geometry of the olivine structure, which has twice as many nearest-neighbor Li^+–e^- pairs compared to repulsive Li^+–Li^+ pairs (the next strongest interaction as determined from first-principles calculations), not

only favors phase-separation but also ensures that there is very little solubility in the coexisting phases. At higher temperatures above the eutectoid point, however, the increased configurational disorder of electrons and holes (Fe^{2+} and Fe^{3+}) prevents Li^+ from coalescing together into a separate phase, consequently diluting the number of attractive Li^+–e^- interactions and overall supporting solid solution formation.[16] This can be readily seen in experimental measurements of the Fe-site electron mobility with increasing temperature, which rapidly increases with the onset of solid-solution formation according to Mossbauer spectroscopy experiments.

The solid solution phase, although dominated by electron disorder, is far from completely random, implying pockets of local ordering of Li and vacancies.[16] The combined lithium ion and electron configurational entropy of the solid solution at the eutectoid transition is only ~ 0.4 k_b (where k_b is Boltzmann's constant), much lower compared to ~ 1.39 k_b for a completely random arrangement. The high T behavior of Li_xFePO_4 also provides useful insight about the room temperature solid solution, specifically that there is only a small energetic difference between the phase separated state and the non-equilibrium solid solution. The single-phase state, which has low configurational entropy and becomes thermodynamically stable at relatively low temperature (~ 400 – 500 K), must then also have low mixing enthalpy and therefore low room-temperature free energy of Li mixing (assuming the heat capacity does not vary significantly with temperature). Local ordering of Li and Li-vacancies at room temperature has recently been observed in both partially electrochemically and chemically delithiated $LiFePO_4$ using

aberration-corrected annular-bright-field scanning transmission electronic microscopy.[18,19] Also, there have been numerous experimental observations of high T Li_xFePO_4 solid solutions quenched to room temperature that remain stable for extended periods of time, from hours to days.

From probing the bulk phase diagram and performing an analysis of the interactions between relevant species (Li^+, $\square^-$, e^-, h^+) informed by first-principles calculations, the free-energy landscape of Li_xFePO_4 is revealed to be highly nuanced, the implications of which are far-reaching in accurately describing the system's lithiation kinetics. Although Li_xFePO_4 is strongly phase-separating at room temperature, the free energy cannot be captured realistically by simplified models (such as a regular solution free energy), which are unfortunately too reductionist insofar as simultaneously capturing local ordering in the solid-solution phase, low free energy of mixing, and correct solubility limits. Because an accurate free energy is a compulsory input parameter for any meaningful modeling of the lithiation kinetics, gross simplification distorts the relative energy of different (de)lithiation pathways, inevitably leading to overall mischaracterization of the charging and discharging kinetics of $LiFePO_4$.

1.2.2 Bulk Thermodynamics of the Li–Fe–P–O System

To this point strictly stoichiometric $LiFePO_4$ has been considered, yet probing the entire Li-Fe-P-O quaternary phase space sheds light not only on the stability of $LiFePO_4$ with respect to chemical decomposition, but also on which possible

secondary phases are produced during synthesis given both the direction of off-stoichiometry and the oxidation environment (oxidizing to reducing conditions). Depending on their properties, secondary phases may be beneficial, neutral, or deleterious to overall electrochemical performance. In the body of literature on $LiFePO_4$, a sweeping variety of synthesis techniques have been employed, often resulting in the production of secondary phases as the consequence either of experimentally designed off-stoichiometry[4,20,21] or dopant-induced off-stoichimetry.[21,22] From first-principles calculations, Ong *et al.*[23] have constructed the Li-Fe-P-O_2 phase diagram and systematically contextualized several of the experimental findings regarding secondary phase formation: Li-deficient stoichiometries have been shown to produce $Fe_7(PO_4)_6$,[22] $Fe_2P_2O_7$,[20] and iron phosphides[21] under increasingly reducing conditions; Li-rich stoichiometries tend to produce Li_3PO_4 [24]; and stoichiometric $LiFePO_4$ decomposes to $Li_3Fe_2(PO_4)_3$ and Fe_2O_3 in highly oxidizing environments,[25,26] and to iron phosphides[20] under highly reducing environments. The specific tailored off-stoichiometry with iron to phosphorous deficiency ratio 2:1 (i.e. $LiFe_{1-2y}P_{1-y}O_{4-\delta}$) results in the formation of a poorly-crystallized $Li_4P_2O_7$-like secondary phase,[4] which grows to a self-limiting thickness.[27] Recently, the same strategy was used to form $Li_4P_2O_7$ on $Li_3V_2(PO_4)_3$ active particles.[28]

1.2.3 Equilibrium Within a Single Li_xFePO_4 Nanoparticle

Since $LiFePO_4$ is functionally useful exclusively in nano-form (less than ~ 100 nm), the relevant governing thermodynamic potential is no longer the bulk free energy but the single-particle free energy, which now includes significant positive energy contributions from surface and interface (generated as a consequence of intra-particle two-phase coexistence). Overall, these contributions modify the fundamental thermodynamic character of the free energy with resounding implications on charging and discharging.

Van der Ven *et al.* have specifically investigated how interfacial energy, surface energy, and coherency strains each independently modify the room temperature thermodynamic equilibrium of the $LiFePO_4$ system.[29,30] The change in free energy arises from imposing new physical constraints on the system, of small fixed volume when considering the effects of surface and interfacial energy and fixed lattice parameters (in the directions parallel to the interface) when considering the effect of coherency strain. In general, the imposed physical constraints on a single $LiFePO_4$ particle cause the free energy of the phase-separated state whereby $LiFePO_4/FePO_4$ phase separation occurs within a single particle to vary as a function of the $LiFePO_4/FePO_4$ phase fraction. Specifically, the free energy now bows out positively in the two-phase regime, overall inducing some concavity in the free energy as compared to the bulk scenario, illustrated schematically in **Figure 7b** compared to **Figure 7a**. This comes as a result of the positive energy penalty (with contribution from both interfacial and coherency

strain energy) now introduced to the system to sustain the $LiFePO_4/FePO_4$ interface within an individual particle in the two-phase regime (schematically shown in **Figure 7b**). Because these positive energy contributions only apply in the phase-separated state, the result is the characteristic positive "bump" in the free energy shown in **Figure 7b**. Not only does explicit consideration of the coherency strain and interfacial energy modify the overall shape of the free energy, but the solubility limits are also affected. The Li concentrations at which the phase-separated state becomes more thermodynamically stable than the single-phase state shift away from their stoichiometric compounds (as seen comparing **Figure 7a** to **Figure 7b**) from the bulk to single-particle scenario.[30]

With decreasing particle size, the overall effect is exaggerated as the relative energy penalty per volume associated with interface creation increases, which

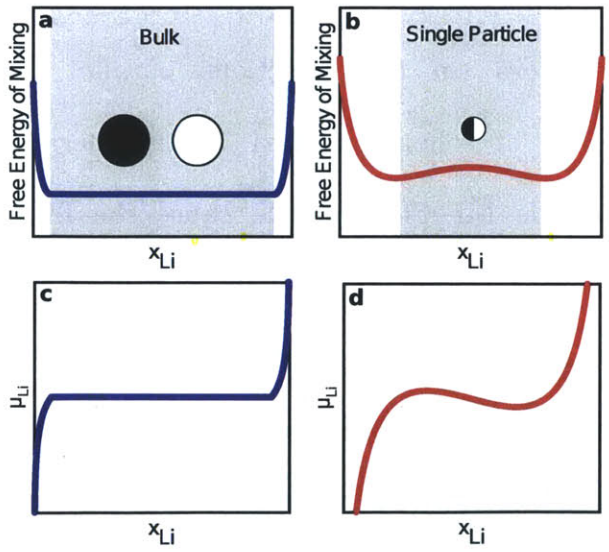

Figure 7: Schematic depictions of (a) the Li_xFePO_4 ($0 \leq x \leq 1$) bulk free energy and (b) the Li_xFePO_4 ($0 \leq x \leq 1$) free energy within a single particle. 2-phase regions are represented in gray. Schematic depictions of the Li chemical potential (μ_{Li}) in (c) bulk Li_xFePO_4 and (d) within a single Li_xFePO_4 particle.

causes the room-temperature miscibility gap to taper further inward. This trend has also been observed experimentally by Meethong *et al.* who observe both room-temperature solubility limits to move inward by nearly 0.15 in Li concentration when the particle size is reduced to less than 50 nm,[31] suggesting that below some critical particle size the solid-solution phase may be most stable at all Li concentrations. Similarly, within a single particle the relative interfacial and surface energy penalties per volume vary with the $LiFePO_4/FePO_4$ phase fraction depending on the particle morphology, because the interfacial area and the relative surface areas of $LiFePO_4$ and $FePO_4$ may either increase or decrease with phase fraction. Consequently, free energy minimization requires the Li concentration within each of the coexisting phases to change with the phase fraction, meaning that interestingly the solubility limits also vary as a function of overall Li concentration within the particle.[30]

Just the contribution of coherency strain energy to the two-phase free energy is in itself significant: given the approximate 5% difference in volume between $LiFePO_4$ and $FePO_4$ and elastic constants approaching ~ 150 – 200 GPa (the range for c_{11}, c_{22}, c_{33} as determined from first-principles calculations),[32] the two-phase free energy increases by a maximum of nearly ~ 1000 J / mol (~ 10 meV / formula unit) according to analysis performed by Van der Ven *et al.* (this for a coherent interface in the *bc* plane, the interface orientation that minimizes the coherency strain energy).[29] Since stresses are relieved at surfaces and elastic strain energy scales with volume, the overall impact of coherency strain compared to interfacial energy

increases with crystallite size, in agreement with HRTEM images of partially chemically delithiated large micron-size particles collected by Chen *et al.* that show the $LiFePO_4/FePO_4$ interface aligned along the *bc* plane.[33]

As a consequence of the positive energy penalty incurred from intra-particle two-phase coexistence, not only is the general shape of the free energy uniquely modified as discussed earlier, but the room-temperature metastable solid solution, which already has a remarkably low bulk mixing free energy, becomes relatively more stable in small $LiFePO_4$ particles as the thermodynamic driving force for demixing reduces even further. Experiments by Tan *et al.* comparing the stability of metastable Li_xFePO_4 solid solutions in nanocrystalline particles to larger particles quenched from high temperature confirm this, showing that nano-Li_xFePO_4 solid solutions not only persist for longer before decomposing but also are stable at lower annealing temperatures.[34] This is a somewhat surprising finding, given that with decreasing particle size the ratio of possible surface nucleation sites to bulk sites increases, which should favor heterogeneous nucleation.

In both cases, of either phase-separation within a single particle or metastable solid solution, the free energy qualitatively resembles that portrayed in **Figure 7b** with some inherent and irremovable non-convexity, as opposed to the bulk scenario shown **Figure 7a**. Moreover, there is *no* scenario where the Li_xFePO_4 free energy within an individual particle is entirely flat or convex. Therefore, the single-particle Li chemical potential, defined as the instantaneous slope of the free energy with respect to Li concentration, resembles the curve shown in **Figure 7d** as

opposed to **Figure 7c**. The single-particle voltage curve (related through $\Delta\phi = -\Delta\mu_{Li}$ and derived in the Introduction, where ϕ is the cell potential and μ_{Li} is the Li chemical potential), however, strongly differs from the experimental open-circuit voltage curve, which exhibits the characteristic plateau for almost the entirety of the Li concentration range (like that shown in **Figure 5**).

1.3 Bulk Kinetics

Most of the salient bulk properties of $LiFePO_4$ were characterized accurately in the very first $LiFePO_4$ papers[3] – open-circuit voltage (OCV; at ~ 3.45 V vs. Li metal shown in **Figure 5**), ordered olivine crystal structure (shown in **Figure 4**), reversible topotactic Li intercalation with theoretical capacity ~ 170 mAh/g, room temperature Li phase separation (shown in **Figure 6**), and both excellent stability and cycling ability. The now well-known excellent rate performance of the material, however, was demonstrated only in the years following, defying the initial claim that $LiFePO_4$ would be strictly relegated to low-rate applications because of kinetic barriers associated with propagating a two-phase interface within an active particle.[3] In fact, through a series of notable experimental modifications the rate performance has been steadily improved to the extent that $LiFePO_4$ is considered suitable for high-rate applications (power tools, electrified vehicles, power grid, etc.). These key improvements have come through a combination of the following: reducing the active particle size to the nano-scale,[35,36] coating active particles with carbon,[37] incorporating dopant impurities,[38] diluting the active mass within the

electrode with electrochemically inactive material,[39] and coating active particles with glassy ionic conductors.[4] Accordingly, much of the $LiFePO_4$ literature has focused on identifying and characterizing the relevant kinetic mechanisms at play during charging and discharging.

1.3.1 Bulk Li Diffusivity

In a material first mischaracterized as low-rate, and later revealed to be high-rate, the bulk Li diffusivity in $LiFePO_4$ has been one of the many issues of contention in the research literature over the past several years. From a variety of both computational and experimental techniques, the room temperature Li diffusivity has been reported to be as low as ~ 10^{-16} cm^2/s and as high as ~ 10^{-8} cm^2/s, clearly an unacceptable discrepancy for such a closely studied material. The type of method used to characterize the diffusivity seems to have a great effect in influencing the measured value. For example, a conventional electroanalytical method to determine the diffusion coefficient involves performing cyclic voltammetry, assuming Cottrell-like behavior, and observing the trend in the peak current as a function of potential scanning rate.[40,41] Another common method involves using the galvanostatic intermittent titration technique (GITT), where the chemical diffusion coefficient is ascertained from the voltage response to applied current pulses.[42,43] Electro-impedance spectroscopy (EIS) methods have been used to deduce the diffusivity typically by invoking the Randles equivalent circuit, and extrapolating the Warburg impedance from a Nyquist plot.[40,42,44-46] All of these

methods yield low Li diffusivity values inconsistent with the rapid charging and discharging behavior that is the hallmark of $LiFePO_4$ electrodes.

The challenges encountered in trying to determine accurately the bulk Li diffusivity in $LiFePO_4$ from classical electroanalytical methods call for more appropriate measurement techniques that reflect the actual excellent rate-performance of $LiFePO_4$ electrodes observed in practice. In this regard, atomistic computational models are particularly adept at describing local Li migration.[47,48] Morgan *et al.* first calculated the intrinsic Li ion diffusivity in $LiFePO_4$ from first-principles methods and found that room temperature Li conduction is especially rapid ($D_{Li} \sim 10^{-8}$ cm^2/s) along 1D tunnels oriented in the [010] direction illustrated in **Figure 4b** and negligible along perpendicular directions ([001] and [101]).[47] Islam *et al.* confirmed this finding, identifying the same anisotropic local Li migration behavior using empirical potentials.[48] All of these computational findings were further validated when Nishimura *et al.* confirmed experimentally the same favored direction of Li motion by visualizing the positions of Li atoms in neutron diffraction experiments.[49] The local migration behavior of Li in $LiFePO_4$ was recently examined quantitatively by Sugiyama *et al.*[50] who measured muon-spin rotation and relaxation spectra in polycrystalline $LiFePO_4$ samples and estimated D_{Li} to be ~ 3.6×10^{-10} cm^2/s at room temperature, much nearer to the values determined from first-principles calculations than to previous experiments. The verification of rapid Li diffusivity in $LiFePO_4$ is especially reassuring in that it resolves the apparent

mystery of how a cathode material can perform exceptionally well at rapid rates despite having supposedly poor bulk transport properties.

1.3.2 Electronic Conductivity

Like the Li diffusivity, there have been many studies focused on characterizing electronic conductivity of $LiFePO_4$, again with reported values spanning several orders of magnitude. Much of the literature reports the bulk electronic conductivity as simply 'poor' (10^{-7} – 10^{-9} S/cm[51,52]), but its role in the charging and discharging process, specifically whether or not it is rate-limiting, remains unclear. The challenges in measuring bulk electronic conductivity and interpreting electronic conductivity measurements are multiple and will be explored in this section.

The mechanism responsible for electronic transport in bulk $LiFePO_4$ is, however, well understood and is not a source of contention in the literature. Electronic conduction in the mixed valence state proceeds through thermally activated small polaron hopping. As discussed earlier, the electron associated with the Fe^{2+}/Fe^{3+} redox localizes on the transition metal sublattice. A small polaron is defined as the 'quasiparticle' comprised of the localized electron (or hole) and its induced polarization field that distorts the local crystal. In the migration process both the electron (or hole) and its associated local distortion move together[53] on a 2D plane defined by the transition metal sublattice (*bc* plane). The electronic conductivity, therefore, is determined largely by two parameters, namely the

activation energy for electron migration and the concentration of charge carriers (which is set extrinsically by impurities or by the Li concentration).

Two common electrochemical methods used to characterize the electronic conductivity are electrical impedance spectroscopy (EIS) and the four-point Van der Pauw DC method. EIS involves first measuring the current response at different frequencies and then using equivalent circuit models to infer the electronic conductivity, while the four point Van der Pauw method determines the resistivity of a thin sample by measuring the voltage response to an applied DC current. Each of these techniques employs ionically blocking electrodes, making electrons the only contributors to the observed current. Electronic conductivities obtained from electrochemical measurements are generally in the 10^{-7} – 10^{-9} S/cm range,[51,52] which is significantly lower than the conductivity of other cathode materials such as Li_xCoO_2 (~ 10^{-1} S/cm for a single crystal in the semiconductive x = 1 phase).[54] This has led many in the battery community to label electron transport as the rate-limiting process in $LiFePO_4$.

There are, however, important challenges regarding the interpretation of measurements derived from classical electrochemical methods. The difficulty in decoupling conductivity in the active material from electrode-scale resistance and the physical relevance of decoupling ionic and electronic motion call into question the common belief that electron transport is rate limiting in $LiFePO_4$. The first important challenge associated with the use of classical electrochemical methods lies in the interpretation of multi-particle measurements, in which electronic

conductivity within particles must be separated from electronic resistance at the electrode scale. Sources of electrode-scale resistance include contact resistance between the current collector and the composite electrode, contact resistance between the active materials and the carbon conductive network and contact resistance at the boundary between particles.[52] For example, Delacourt *et al.*[52] reported a 7 order of magnitude increase in electronic conductivity going from pure $LiFePO_4$ (10^{-9} S/cm) to carbon-coated $LiFePO_4$ (10^{-2} S/cm). As stated by the authors, such an increase in conductivity cannot be attributed to the particles themselves, but can be understood rather as a signature of the percolating conducting network formed by the carbon coating. This analysis suggests that the method employed, in this case EIS, was unable to capture strictly the electronic conductivity within single particles.

The multi-scale nature of electronic conductivity in composite electrodes is readily seen with broadband dielectric spectroscopy (BDS) which, using frequencies ranging from 40 to 10^{10} Hz (an extended frequency range compared to standard EIS), can identify charge fluctuations at different length scales in the electrode. As the frequency of an electromagnetic wave increases, its wavelength decreases, making high frequency waves ideal for probing the dynamics of electron transport at small length scales. Conversely, low frequency waves can be used to assess electronic transport at larger length scales. Using BDS, Seid *et al.*[55] identified conductivities ranging from 10^{-6} S/cm to 10^{1} S/cm, respectively indicative of electrode-scale conduction and carbon coating conduction. This study, however, was

also unable to isolate the electronic conductivity within $LiFePO_4$ particles themselves. This may be an indication that at the length scale at which electronic transport within single particles occur the recorded current response is dominated by other forms of electronic transport, such as electronic transport within the carbon coating network.

Several strategies have been employed in the literature in order to isolate particle conductivity from electrode scale conductivity. One approach employed by Amin *et al.*[51,56] involves performing measurements on large mm-size single crystals. AC impedance spectroscopy as well as DC polarization/depolarization measurements were performed on large millimeter-sized $LiFePO_4$ crystals, leading to a 2D electronic conductivity in the *bc* plane on the order of 10^{-7} S/cm at 50 °C.[51] Similar measurements with electronically blocking electrodes found the ionic conductivity to be approximately 4 orders of magnitude less than the electronic conductivity at high temperature (140 °C), thus identifying ionic transport as opposed to electronic transport as the rate-limiting process in Li transport. This conclusion challenges the common belief that electronic conductivity is rate-limiting in $LiFePO_4$.

Another experimental approach to isolate particle-scale from electrode-scale conductivity consists of directly measuring the polaron hopping rate between adjacent Fe atoms using Mossbauer spectroscopy. Mossbauer spectroscopy is able to detect local changes in the oxidation states of iron atoms with high spatial and temporal resolution using isomer shifts in the gamma ray absorption spectrum of Fe

nuclei. Using this method, Tan *et al.*[57] found polaron migration barriers ranging between 0.3 and 0.41 eV for fully delithiated and fully lithiated particles, respectively. These values are on the low end of the experimentally measured polaronic activation barriers, which are mostly reported to be in the 0.4 – 0.6 eV[52,58] range. Notable exceptions are the low activation barriers reported by Takahashi *et al.* (0.155 eV, using EIS)[40] and Shi *et al.* (0.189 eV using DC measurement on a pressurized sample).[58]

Polaronic activation barriers can also be assessed by theoretical methods based on first principles. Using DFT, Maxisch *et al.*[53] reported activation barriers ranging from to 0.175 eV to 0.215 eV in the fully delithiated and fully lithiated limits, respectively. These barriers are comparable to previously calculated lithium-ion migration barriers (0.2 – 0.27 eV), once again challenging the belief that electronic mobility is the rate-limiting step in $LiFePO_4$. The method, however, does not take into account the binding energy between a polaron and its nearest lithium ion. This binding energy was calculated by Maxisch *et al.* to be on the order of 0.5 eV, indicating that ionic and electronic migration in $LiFePO_4$ is likely coupled. This finding leads to the second important challenge in interpreting electronic conductivity measurements, namely the physical relevance of separately measuring ionic and electronic conductivities to assess rate capabilities. During electrochemical (dis)charging, Li^+ and e^- simultaneously diffuse within a particle and, as determined from first-principles calculations, this motion is likely to be coupled. This claim is supported by the aforementioned high Li^+/polaron binding

energy (Maxisch *et al.*) as well as by a recent DFT investigation by Sun *et al.*[59] which finds a strong correlation between Li^+ and e^- migration paths during Li transport.

Ambipolar lithium diffusivity, which captures the aggregate effect of Li^+ and e^- migration, emerges as a more relevant quantity to describe electrochemical processes. Several experimental methods described in section 3.1.1, such as cyclic Voltammetry, PITT, and GITT, involve partial (de)lithiation of LiFePO4 particles and therefore attempt to capture the coupled motion of Li+ and e- during electrochemical (dis)charging processes. However, methods that separately measure ionic or electronic conductivities at fixed lithium concentration, such as EIS or Four Point Van der Pauw, by definition cannot capture such coupled motion. Analysis of data provided in the literature shows that ambipolar diffusivity cannot simply be extracted from the separate investigation of electronic and ionic conductivities. Ambipolar diffusivity can indeed vary significantly from the prediction of mean-field models, which relate ambipolar diffusivity to electronic and ionic diffusivity in the case of non-interacting charged species. The predictions of ambipolar diffusivity from mean field models is a two-step process that is expressed in **Equations *(8)*** and ***(9)***. **Equation *(8)***, known as the Nernst-Einstein equation, is used to relate ionic conductivities to ionic diffusivities. The mean-field approximation is expressed in **Equation *(9)***, which relates the ionic diffusivities to the ambipolar diffusivity in the case of an ideal solution of non-interacting charged species.

$$D_i = \frac{\sigma_i kT}{c_i q^2} \quad (8)$$

$$\widetilde{D} = \frac{2D_{Li+}D_{e-}}{D_{Li+} + D_{e-}} \quad (9)$$

In **Equations** ***(8)*** and ***(9)***, σi is the conductivity of species i, c_i is the carrier concentration of species i, D_i is the diffusivity of species i and $\widetilde{D}$ is the ambipolar diffusivity.

An example of the discrepancies between the predictions of mean field models and the measured ambipolar diffusivities can be seen from the work of Amin *et al.*[51] At 450 K, Amin et al. measured the electronic and ionic conductivities using EIS to be 10^{-4} S/cm and 10^{-8} S/cm, respectively, and the ambipolar diffusivity was found using DC polarization measurements to be on the order $10^{-8} - 10^{-9}$ cm²/s. The mean-field model approach expressed in **Equations** ***(8)*** and ***(9)*** would predict the same ambipolar diffusivity to be ~ 10^{-19} cm²/s, which is eleven orders of magnitude smaller than the measured value (a 5% carrier concentration was assumed in this calculation, as determined from the solubility limits of $LiFePO_4$ at 450 K[60]). This highlights the fact that the coupled motion of Li^+ and e^- is not simply the sum of two independent ionic motions, and therefore questions the use of ionic and electronic conductivities as a metric for rate capabilities.

Nevertheless, the idea that electronic conductivity is rate-limiting in $LiFePO_4$ is still widely accepted in the literature. To address the purported electronic conductivity issue, there have been several studies of doping $LiFePO_4$ in an attempt

to improve the bulk electronic conductivity. And, to this end, reported conductivities of doped $LiFePO_4$ have been as high as 10^{-1} S/cm and excellent rate performance has been obtained in cycling experiments with doped $LiFePO_4$.[38] Whether these improvements arise from improving the bulk electronic conductivity or not remains an unresolved issue of contention in the literature and is beyond the scope of this work.

In summary, although it is generally believed to be low, no consensus has been reached on the true value of the bulk electronic conductivity in $LiFePO_4$, and the jury is still out on whether or not electron migration is the rate-limiting step in this material. Nevertheless, in electrochemical systems the independent ionic and electronic conductivities as measured from the current response to an electric field at a fixed lithium concentration may not be a direct predictor of rate performance. The coupled $Li^+ - e^-$ migration during electrochemical processes where Li^+ and e^- are supplied externally determines the true rate at which the electrochemical reaction can proceed, which for nano-sized $LiFePO_4$ has proven to be very high.

1.4 $LiFePO_4$ Phase Transformation Models

Given the strong phase-separating behavior of Li at room temperature, the extremely high rate performance of $LiFePO_4$ is certainly puzzling upon first inspection. As initially noted by Padhi *et al.*, Li insertion and removal through propagating a two-phase $LiFePO_4/FePO_4$ interface within an active particle can only hinder the overall discharging and charging kinetics (in comparison to a purely

equilibrium solid-solution mechanism), which motivated the initial conclusion that $LiFePO_4$ would be best suited for low-rate applications.[3] Therefore, elucidating the single-particle lithiation mechanism is critical not only to explain why $LiFePO_4$ can function as a high-rate material, but also to clarify the requisite criteria for identifying new high-rate two-phase battery electrode materials that can behave similarly.

Unfortunately, uncovering the single-particle lithiation mechanism poses significant challenges. First, because most conventional electroanalytic characterization methods are performed on bulk electrodes containing many particles, the single-particle lithiation mechanism will be obfuscated in the extracted data by the multi-particle behavior (if the single–particle behavior is not identically mirrored at the multi–particle scale) and ensuing electrode-scale inhomogeneity. Second, because lithiation is a dynamic process, direct characterization then requires *in-situ* single-particle experiments, which require both temporal and spatial precision beyond the limits of current experimental characterization methods. Consequently, the majority of experiments investigating the $LiFePO_4$ lithiation mechanism fall into two broad categories with their respective built-in tradeoffs: either *ex-situ* analysis on relaxed single particles, or conventional electroanalytic characterization of charging or discharging bulk electrodes (i.e. galvanostatic voltage curves, PITT, GITT, CV, etc.). Nevertheless, these limitations have not prevented ample progress in recent years toward understanding the $LiFePO_4$ single-particle lithiation mechanism, as carefully

designed experiments and models have now shed some light on why $LiFePO_4$ is capable of being rapidly charged and discharged.

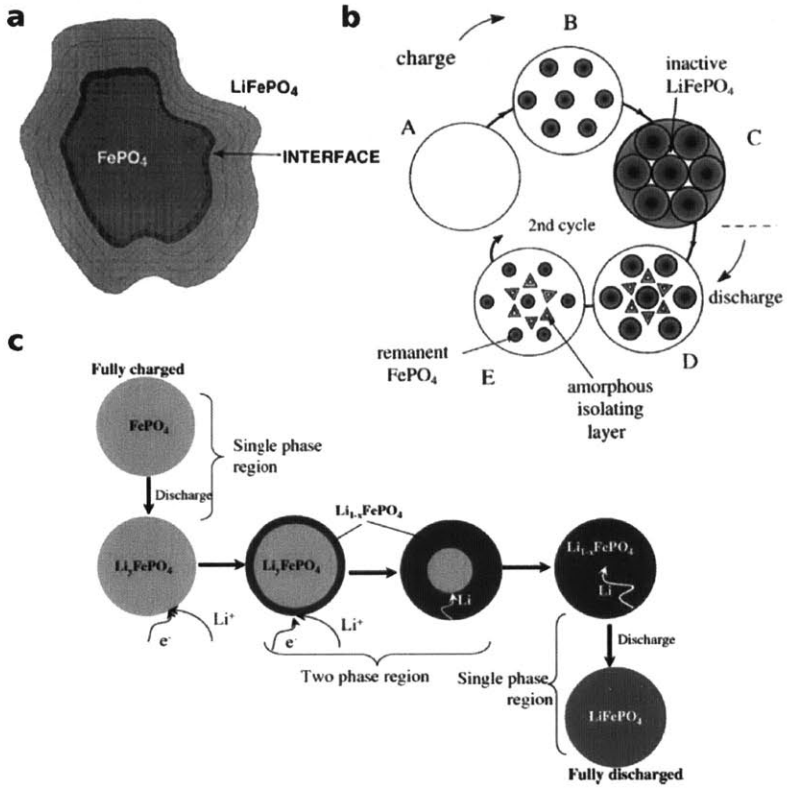

Figure 8: Isotropic models of the single-particle $LiFePO_4$ transformation mechanism as described by (a) Padhi *et al.*, (b) Andersson *et al.*, and (c) Srinivasan *et al.*

1.4.1 Isotropic Two–Phase Models

Inferred from the characteristic flat $LiFePO_4$ voltage curve, the most intuitive lithiation models all involve intra-particle two-phase coexistence, where on discharge the $LiFePO_4$ phase grows at the expense of $FePO_4$ and the reverse occurs upon charge. Padhi *et al.* first described a "core-shell" process as shown schematically in **Figure 8a**[3] and **Figure 8c**,[61] and in the years following this

general model has been refined and modified to take into account the Li diffusion anisotropy, coherent strain energy, dimensionality of the rate-limiting growth mechanism, etc. with some notable examples depicted in **Figure 9**. In the "core-shell" scheme, the reaction front upon both Li insertion and extraction moves radially inward, meaning that the interfacial area shrinks with time. This feature of the model was initially used to explain how at higher currents, the shrinking interfacial area becomes a current bottleneck and consequently limits the accessible capacity.[3] Similarly, the "mosaic model" proposed by Andersson *et al.* accounts for inaccessible capacity as the result of growing $FePO_4$ domains (on charge, for instance) impinging upon each other leaving unconverted $LiFePO_4$ in between (shown in **Figure 8b**).[62] Through carbon addition and reducing the particle size (to ~ 100 to 150 nm), however, close to the entirety of the theoretical capacity (~ 170 mAh/g) becomes accessible even at high rates,[36] which certainly limits the efficacy of the initial "core-shell" and "mosaic" models in describing the single-particle lithiation mechanism of functional $LiFePO_4$.

1.4.2 Anisotropic Two–Phase Models: Morphology and Kinetics

Given the known Li diffusion and coherency strain anisotropy in $LiFePO_4$, an isotropic "core-shell" mechanism appears both energetically[63] and kinetically unfavorable, prompting Chen *et al.* to first study the arrangement of Li within a partially chemically delithiated micron-size $LiFePO_4$ particle using HRTEM.[33] The $LiFePO_4/FePO_4$ interface (seen to be ~ 4 nm wide) was observed to align

preferentially along the *bc* plane (as shown schematically in **Figure 9a**), the orientation that minimizes the coherency strain energy[29] and maximizes the number of either fully occupied or fully empty 1D Li channels, consistent with rapid Li diffusivity[47] along the [010] direction. Laffont *et al.* observe similar behavior in partially chemically and electrochemically (*ex-situ*) delithiated $LiFePO_4$ using both HRTEM and electron energy loss spectroscopy (EELS) and infer a more ordered $LiFePO_4/FePO_4$ interface shown in **Figure 9b**.[64] Both investigations conclude that the single-particle lithiation mechanism proceeds through a two-phase interface moving perpendicular to the [010] direction as successive *b* channels are emptied on charge and filled on discharge.

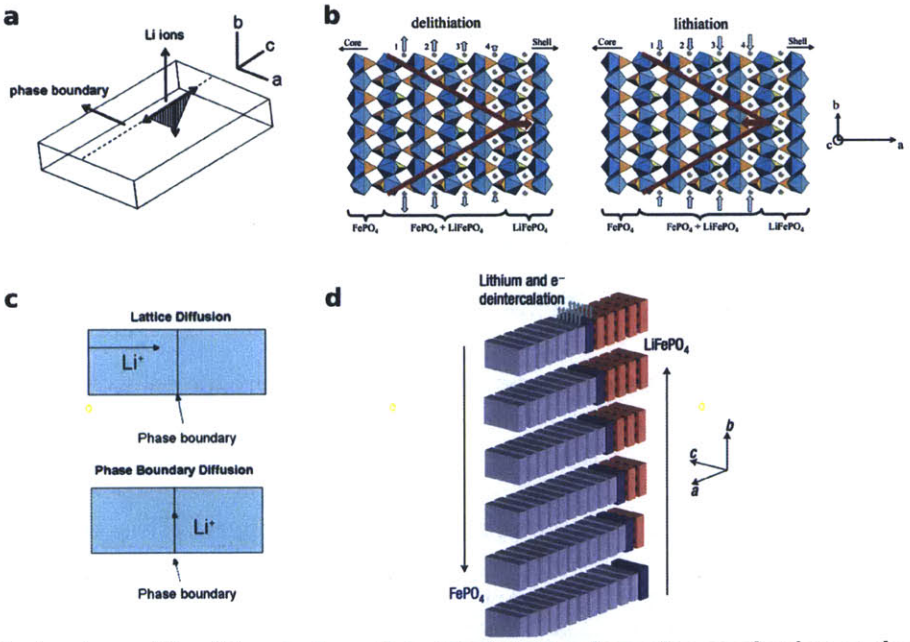

Figure 9: Anisotropic models of the single-particle $LiFePO_4$ transformation mechanism as described by (a) Chen *et al.*, (b) Laffont *et al.*, (c) Allen *et al.*, and (d) Delmas *et al.*

The insights gleaned from chemical delithiation experiments, although certainly valuable, cannot substitute exactly for a description of the *electrochemical*

lithiation mechanism, and the results from chemical delithiation experiments therefore must be interpreted with the appropriate caveats. Depending on the exact reagents used, the applied driving force for chemical delithiation can be inordinately high,[60] enough to structurally damage the $FePO_4$ host framework, as seen in scanning electron microscopy (SEM) images obtained by Chen *et al.* displaying noticeable and increasing crack formation in further oxidized samples.[33,65] Introduction of dislocations and cracks during electrochemical Li insertion and deinsertion are well-known causes of increased impedance and capacity fade over time,[66,67] which seems far less likely in nano-$LiFePO_4$ considering the well-observed long cycle life and reversibility at reasonable C-rates typical to conventional battery use. More apparent, the mechanism of combined Li^+ and e^- insertion is fundamentally different in an electrochemical than in chemical delithiation. In an electrochemical cell, the Li^+ is incorporated from the electrolyte, and the electron arrives from the current collector; whereas, there is no inherent separation of Li^+ from e^- in the chemical delithiation reaction. Moreover, the final state of a chemical delithiation reaction does not correspond to the same multi-particle equilibrium as earlier discussed, since $LiFePO_4$ particles in solution are not electronically and ionically interconnected to each other. This difference in the defined system constraints in part explains why Delmas *et al.*[68] observe predominantly fully lithiated and delithiated particles in a partially discharged electrochemical $LiFePO_4$ cell as opposed to intra-particle two-phase coexistence as observed in chemical delithiation experiments. The ionically and electronically

well-connected particle network in a real electrode allows the system to access the lower energy states whereby most $LiFePO_4/FePO_4$ interfaces are removed. Hence, it is unlikely that *ex-situ* observations on chemically delithiated materials bear any resemblance to the intermediate states of charge that an electrode goes through in electrochemical experiments.

The other broad approach employed in the literature to identify the relevant Li insertion and extraction kinetics of Li_xFePO_4 involves analyzing the behavior of a bulk electrode during charge and discharge using conventional electroanalytical methods and, more recently, pairing these methods with *in-situ* spectroscopy. Potentiostatic charging/discharging experiments performed on a two-phase system like $LiFePO_4$ can be regarded as an analogue to traditional secondary phase precipitation and growth initiated by some constant temperature undercooling. Therefore, traditional phase transformation kinetics models, such as time-cone analysis[69] of concurrent nucleation and growth or Kolmogorov–Johnson–Mehl–Avrami (KJMA) analysis[70] have been used to gain insight into the $LiFePO_4$ phase transformation mechanism.[71-74] By measuring the degree of phase transformation (i.e. the volume fraction of the new phase determined by integrating the current response) with time given a constant applied potential, the dimensionality of the growth mechanism has been interpreted by fitting to the Kolmogorov–Johnson–Mehl–Avrami equation:

$$f = 1 - \exp(-kt^n) \qquad \textbf{(10)}$$

where f is the volume fraction of the secondary phase, t is the transformation time, and k and n are fitting parameters. The information describing the phase transformation mechanism is contained in n, the Avrami exponent, which can range from values of ~ 1 to 4, with lower values signifying a 1D growth mechanism (n ~ 1 – 2) and higher values signifying either 2D (n ~ 2 – 3) or 3D (n ~ 3 – 4) growth. Hong *et al.* find n = 1.6 charging ~ 1 μm aggregates of $Li_xFe_{0.9}Mg_{0.1}PO_4$ with a potential step from 3.1 to 3.48 V (with respect to Li metal).[71] Allen *et al.* determine n ~ 1 in 60 – 70 nm $LiFePO_4$ particles discharged from 4.2 to 3.0 V,[75] and more recently, Oyama *et al.* find n = 0.66 and n = 1.08 in 203 nm $LiFePO_4$ particles discharged from 3.5 to 3.35 V and 3.42 to 3.41 V, respectively.[74] Also, in the work by Oyama *et al.*, the data obtained from charging and discharging smaller particles (84 nm and 45 nm) could not be fit to the Avrami equation with $n \geq 1$. All of these results are seemingly at odds with the initial proposed isotropic growth models (shown in **Figure 8**), which conform to 3D growth (and would therefore result in n ~ 2 – 3), and alternatively support the existence of anisotropic growth. The Avrami exponent n also contains information on possible rate-limiting kinetic transformation mechanisms:

$$n = a + bc \qquad \textit{(11)}$$

where a indicates the rate behavior of nucleation, b refers to the dimensionality of growth, and c describes the rate of growth. The possible values of a, b, and c, as well as their physical significance are shown below in **Table 2**.[76] Allen *et al.* initially interpreted n ~ 1 as a 1D constant growth mechanism, informed by anisotropic

diffusion of Li within $LiFePO_4$, with zero nucleation rate (i.e. $a = 0$, $b = 1$, and $c = 1$),[75] and then later revised the model noting that a 1D diffusion mechanism can facilitate 2D diffusion-controlled phase boundary growth with zero nucleation rate (i.e. $a = 0$, $b = 2$, and $c = ½$),[72] to better agreement with the models proposed by Chen *et al.* and Laffont *et al.* Both of these descriptions of the phase transformation mechanism are highlighted in **Figure 9c**.

Parameter Value	Physical Meaning
a = 0	Zero nucleation rate
a = 1	Constant nucleation rate
a > 1	Increasing nucleation rate
0 < a < 1	Decreasing nucleation rate
b = 1	1D growth mechanism (i.e. needle)
b = 2	2D growth mechanism (i.e. disk)
b = 3	3D growth mechanism (i.e. sphere)
c = 1	Linear phase boundary growth (i.e. phase-boundary limited growth)
c = 1/2	Parabolic phase boundary growth (i.e. diffusion-limited growth)

Table 2: Indices corresponding to nucleation rate (*a*), geometric (*b*), and rate-limiting transformation mechanism contributions (*c*) in equation *(9)* which defines the Avrami exponent *n* in equation (*10*)

As with chemical delithiation experiments, special attention should be paid to the applicability of KJMA analysis to exactly describing the lithiation kinetics of phase transformation electrodes by examining the strength of the model's inherent assumptions. The KJMA equation was initially derived to describe an isothermal phase transition in a bulk material (i.e. crystallization from melt) rather than a phase transformation propagating through an assembly of many discrete small particles (like in a Li_xFePO_4 electrode).[77] In the latter case, the assumption of

homogeneous nucleation may be tenuous considering the increased availability of surface nucleation sites with small particles. Also, the critical nuclei may approach the size of the active $LiFePO_4$ particles themselves, especially at low overpotential, which makes the built–in assumption of a zero–volume critical nucleus size problematic. The overall transformation behavior described by the KJMA equation corresponds to initial slow transformation rate with the first nucleation of the second phase, then rapid growth of nuclei unimpeded by each other, and again reduced rate of transformation due to growing nuclei impinging on each other. In a multi-particle system, however, no single growing nucleus can exceed the size of its host particle, an important constraint not considered in the initial KJMA formulation, which far decreases the likelihood of growing $LiFePO_4$ grains impinging on each other and is only exaggerated in a system of consisting of nano-size $LiFePO_4$ particles. Also, when applying steep potential steps to initiate phase-transformation, the spatial gradient of the potential across the cell is likely very sharp and non-uniform, and will vary depending on the electrode architecture (loading density, thickness, etc.), meaning that the driving force for transformation may vary drastically within the electrode itself. To this end, the accuracy of KJMA analysis increases in systems with larger particle size and homogeneous distribution of the applied potential across the cell, to qualitative agreement with the measurements performed by Oyama *et al.*[74] who find more amenable values of the Avrami exponent consistent with nucleation and growth ($n \geq 1$) in larger particles (203 nm) with small applied overpotential (10 mV steps).

Noting the importance of analyzing electrochemically discharged and charged particles to gain insight into the single-particle transformation mechanism, Delmas *et al.* characterized several partially electrochemically delithiated Li_xFePO_4 samples with varied average Li concentration using *ex-situ* XRD.[68] Interestingly, the XRD spectra exhibit no peak shifting or broadening with changing average Li concentration, and rather appear as a linear combination of the $LiFePO_4$ and $FePO_4$ spectra superimposed on each other. This corresponds to a state where a fraction of the active $LiFePO_4$ particles are fully lithiated, and the remainder fully delithiated, and has recently been confirmed directly using TEM equipped with precession electron diffraction (PED) phase-mapping capability.[78] Delmas *et al.* have proposed the "domino-cascade" model, where phase-boundary propagation perpendicular to the *b* axis is extremely rapid compared to initial nucleation (**Figure 9d**), meaning that at any given snapshot in time a Li_xFePO_4 particle is most likely to be either fully lithiated or delithiated, effectively rationalizing their results.

To this point, even with the progress made in understanding the possible single-particle lithiation mechanisms, the origin of the exceedingly rapid charging and discharging capability of $LiFePO_4$ (especially in comparison to Li intercalation systems without strong first-order phase separating behavior) has remained unaddressed. Inherent to a two-phase growth mechanism, the basis for all mechanisms discussed thus far, is a nucleation step followed by two-phase growth. A single–phase mechanism, however, avoids the additional kinetic barriers associated with nucleation and growth altogether, and the barrier for nucleation as

estimated from classical nucleation theory is not insignificant. Considering the discharge (lithiation) process, Li ions coalesce together within the $FePO_4$ framework with some applied driving force (underpotential). Whether growth continues or not depends if the bulk free energy reduction from creating a $LiFePO_4$ cluster outweighs the positive energy penalty associated with creating a coherent $LiFePO_4/FePO_4$ interface. Only beyond some critical nucleus size does growth become stable, and only with greater applied driving force can the critical nucleus become smaller. Assuming isotropic interfacial energies and coherency strain, the critical nucleus size (of radius r^*) and critical nucleus barrier (ΔG^*) can be roughly estimated using well–known expressions derived from classical nucleation theory:

$$\Delta G_{r^*} = \frac{16\pi \cdot \gamma^3 \cdot v^2}{3(|\Delta\phi| - \Delta g_s)^2} \qquad (12)$$

$$r^* = \frac{2 \cdot \gamma \cdot v}{(|\Delta\phi| - \Delta g_s)} \qquad (13)$$

where γ is the $LiFePO_4/FePO_4$ interfacial energy, v is the molar volume of $LiFePO_4$, Δg_s is the coherency strain energy, and $\Delta\phi$ is the applied potential. The variation of the critical nucleus size with applied potential according to *(15)* is shown in **Figure 10** using values for γ, v, Δg_s obtained from the literature.[29,30] Even by approximately accounting for heterogeneous nucleation by ignoring the coherency strain energy altogether (Δg_s ~ 3,200 J/mol or 33 meV/Li for an interface oriented along the *bc* plane)[29] and considering only half of the interfacial energy obtained from literature (i.e. one half of γ = 0.96 J/m^2),[30] a 50 nm critical nucleus, which is also the typical size of an entire nano–$LiFePO_4$ particle, requires in excess of 50 mV underpotential

(as shown by the solid blue line in **Figure 10**) with ΔG_{r^*} approaching several hundred thousand kT (thermal energy) per nucleus cluster at room temperature.

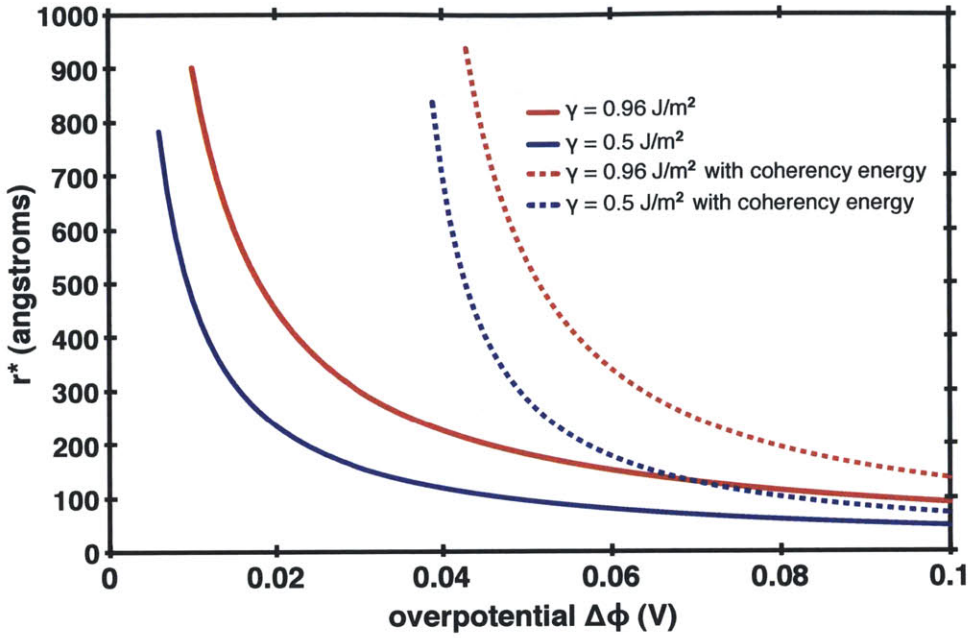

Figure 10: Plot of critical nucleus size (r*) vs. overpotential (ΔΦ) related by equation (15) including and not including coherency energy (dashed and solid lines, respectively), for different values of the $LiFePO_4/FePO_4$ interfacial energy γ (0.96 J/m2, in red, from literature and 0.5 J/m², in blue).

The plots shown in **Figure 10** convey an overarching point: the minimum ~ 10 – 20 mV (under)overpotential required for complete (dis)charge[79] observed in experiments is unusually small and a lithiation mechanism contingent on a nucleation step cannot account for this. This analysis motivates the possibility that the single-particle phase transformation in $LiFePO_4$ may avoid crystalline nucleation and growth and veer from the equilibrium phase diagram. Instead, the transformation, especially in nano-particles, likely occurs through an alternative non-equilibrium pathway that may be energetically costlier, but kinetically faster.

1.4.3 Dynamic Amorphization

Meethong et al.[80] investigated the possible formation of an amorphous phase stabilized at the active particle surface which may assist the phase transformation kinetics, and Tang et al.[81,82] later investigated the conditions (applied potential, particle size, misfit strain, etc.) where such a mechanism is likely to be predominant using a diffuse-interface continuum model. An amorphous transformation scheme offers several kinetic advantages over the traditional crystalline nucleation and growth mechanism. Although the volume free energy is higher compared to the bulk 2-phase $LiFePO_4/FePO_4$ equilibrium, formation of an amorphous phase ensures that the surface energy is likely lower, crystal–glass interfacial energy is likely lower, and misfit stresses are better relieved, which overall implies faster nucleation kinetics.[83] In addition to improved nucleation kinetics, ceramic glasses are known to be fast isotropic ionic conductors, which may offer improvement over 1D diffusion in crystalline $LiFePO_4$ and accelerate growth. Through analysis of the intensity of both $LiFePO_4$ and $FePO_4$ peaks in in-situ XRD spectra captured at different state of charge (at C/50 rate in 34 nm particles), Meethong et al. determine the relative phase fraction of each phase. Unexpectedly, the phase fraction was observed to vary non-linearly with state of charge, which was thus interpreted as proof of the formation of an amorphous phase to ensure mass balance.[80]

Amorphization provides a compelling explanation for fast (de)lithiation kinetics in Li_xFePO_4, but there are some unresolved questions which give pause for further consideration. Presumably, the initial and final states are still both

crystalline (either olivine $FePO_4$ or $LiFePO_4$), meaning that in addition to nucleating an amorphous phase, there is also a recrystallization process, which will undoubtedly have its own additional kinetic barriers. Also in the case of charging, the amorphous phase must recrystallize into metastable olivine $FePO_4$, rather than into the equilibrium berlinite crystal structure.[8] If, however, there is no recrystallization and the amorphous structure is retained, it is especially surprising that this process would occur at or near the identical potential as the $LiFePO_4/FePO_4$ crystalline phase transformation (~ 3.5 V vs. Li). Considering a crystalline to amorphous transformation path from an atomistic point of view, significant bond breaking and rotation must occur, which intuitively seem more kinetically burdensome than Li insertion into a purely crystalline intercalation structure, especially surprising given the apparent less–than ~ 50 mV overpotential required to initiate the transition as observed by Meethong et al.[80] From an experimental methods standpoint, confirmation of the existence of an amorphous phase purely from XRD peak intensities has been recently questioned,[84,85] owing to disagreement over the cause of the so-called "delay" observed in in-situ experiments which may be the result purely from electrode-scale inhomogeneity enhanced by pressure gradients in the electrode.[85] Nevertheless, consideration of a potential amorphous transition path helps clarify the necessary overall criteria for any realistic $LiFePO_4$ single-particle non-equilibrium lithiation model: 1) an expedient kinetic (de)lithiation mechanism that is 2) available with small (~ 10 – 20 mV) driving force.

1.5 Remaining Questions

Although more than 2100 publications have been written on the subject of $LiFePO_4$ since the initial work in 1997,[86] there are still important questions outstanding that remain unaddressed, and the following work focuses on three:

(1) Can the apparent energy density limitation of $LiFePO_4$ be addressed?

$LiMnPO_4$ has a higher voltage (and near identical capacity) as $LiFePO_4$, but other electrochemical properties are not favorable, namely safety and rate performance. To compromise, one approach adopted in the literature has been to investigate the electrochemical performance of mixed olivines such as $Li(Fe,Mn)PO_4$. This motivates a study of the ***Phase Diagram and Electrochemical Properties of Mixed Olivines from First-Principles Calculations.***[87]

(2) Why are the Li intercalation kinetics in nano-$LiFePO_4$ particles so favorable?

Although the excellent rate performance observed in nanosized $LiFePO_4$ particles is in itself a favorable property, it comes at the expense of reduced volumetric energy density by way of poorer packing of smaller particles (resulting in a lower than desired tap density).[88] The scale of improvement in rate performance observed with reducing the particle size far outpaces that predicted by Fick's laws (assuming the source of improvement is strictly from reducing the diffusion length) and necessitates investigating the ***Particle Size Dependence of the Ionic Conductivity.***[89]

(3) How can $LiFePO_4$ be a fast charging and discharging material despite being a phase-separating system?

The single particle transformation mechanism in $LiFePO_4$ has been investigated at length in the literature as described in detail in **1.4**, but each model proposed therein falls short in adequately answering the above question, which has prompted here investigation into ***The Kinetics of Non-equilibrium Li Incorporation in $LiFePO_4$.***[90]

Chapter 2: Methods

The thermodynamic and kinetic models presented in this thesis are constructed from ground state energy calculations coupled with physical intuition gleaned from the extensive $LiFePO_4$ literature. Therefore, the accuracy of these calculated input energies is of paramount importance to the validity of this work. Fortunately, the combination of density functional theory (DFT) calculations used to parametrize a cluster expansion followed by Monte Carlo simulations is a tried and tested methodology that connects material–specific electronic structure to macroscopic–scale thermodynamics and kinetics. Furthermore, independently verifying known experimentally measurable materials properties of the system in question ensures the veracity of the overall method. The following is a general description in broad terms of the techniques used as the basis of the models presented in this work (more detailed derivations and descriptions can be found in the listed references).

2.1 Ground-State Energies from Density Functional Theory

Determining the exact energy of a given crystal requires solving the time independent Schröedinger equation ($H\psi = E\psi$) for multiple interacting electrons and nuclei, which is currently an intractable computational problem for the system sizes of interest. Through a reformulation of the Schröedinger equation followed by a series of physical approximations, however, accurate solutions of the ground state

energy amenable to numerical computation can be found using DFT. For one, the Born–Oppenheimer approximation[91] is invoked to avoid simultaneously solving for both electrons and nuclei, specifically ignoring the kinetic energy of the nuclei, which are much heavier than the electrons. To overcome the overwhelming complexity of determining the energy of a system of many electrons interacting with each other, one approach has been to simplify the problem by employing the variational principle and solving the Schröedinger equation self-consistently for a system of many independently acting electrons interacting with an effective potential (this is known as the Hartree method).[92] To improve accuracy, in addition to considering a system of independently acting electrons, the additional quantum mechanical property of electron exchange can be incorporated by treating the multi–electron wavefunction as a Slater determinant (this is known as the Hartree–Fock method).[92]

Unfortunately, neither of these methods provides the desired accuracy required or computational ease as DFT, which operates on a different principle enabled by the Hohenberg–Kohn theorem,[93] which allows the problem to be redefined in terms of the electron density rather than the coordinates of multiple interacting electrons. The Hohenberg–Kohn theorem states **(1)** that for a system of interacting particles within an external potential, there is a unique particle density, and **(2)** the energy is a functional of the particle density, and the ground state is the global minimum of this functional.[93] The next approximation involves instead considering a fictitious system of non-interacting electrons (so–called Kohn-Sham

electrons)[94] with identical density as in the actual physical system, and the difference in energy, called the exchange–correlation energy, can be suitably approximated (using the local density approximation (LDA[94]) or more involved exchange–correlation functionals, for instance). Now the complexity of the problem is reduced to minimizing the total energy-functional of a system with no multi-body effects, a computationally manageable problem, and its accuracy depends on the magnitude of the contribution and the accuracy of approximating the exchange–correlation contribution. For the case of systems with strongly localizing electrons (as is the case with $LiFePO_4$), the DFT+U approximation[95-97] which additionally addresses self-interaction error is most accurate.

2.2 Cluster Expansion

To determine some battery properties, such as redox voltage[98] or relative safety to decomposing oxygen,[99] only a few ground state energy (DFT) calculations are required, but determining macroscopic room–temperature thermodynamic properties, such as the Li_xFePO_4 free energy, requires many Hamiltonian evaluations to statistically sample through. Practically, this is an unfeasible time expenditure if each energy evaluation corresponds strictly to a single DFT calculation, which encourages fitting the energy of the Li_xFePO_4 ($0 \leq x_{Li} \leq 1$) system to an equation that can be readily evaluated and is parametrized over the relevant degrees of freedom (this also means coarse–graining over non-relevant degrees of freedom). In Li intercalation systems, the relevant configurations are the ordered

structures with different numbers of $Li^+/\square^-$ (and e^-/h^+) occupying well defined intercalation sites in the $FePO_4$ host structure, and the corresponding energy is amenable to fitting using the cluster expansion method originating from alloy theory.[100]

Any configuration with substitutional disorder (here $Li^+/\square^-$ and e^-/h^+ occupancy) can be exactly represented by an array of occupation variables, $\sigma_i = 1$ for an occupied site, and $\sigma_i = -1$ for an unoccupied site. The energy and any other property that depends on substitutional disorder can be projected onto a linear polynomial expansion of the occupation variables (geometrically defined by the space group of the crystal), which forms an orthonormal and complete basis set. By picking the correct interactions, fortunately relatively few terms are required for sufficient convergence. This allows for relatively accurate and quick–to–compute Hamiltonian evaluations which facilitate performing Monte Carlo simulations in relatively large simulation sizes to obtain the room temperature compositional free energy landscape. For the $LiFePO_4$ system, 245 different ground–state energy evaluations (through DFT) of different $Li^+/\square^-$ (and Fe^{2+}/Fe^{3+}) configurations (short–range orderings in small periodic supercells) were used to parametrize a cluster expansion, with 29 fitting coefficients (mostly pair interactions and a few triplet interactions).[16] In the ensuing Monte Carlo simulations, the cluster expansion is then evaluated ~10^6 times (in larger simulation cells, 6 x 12 x 12 unit cells or so) to effectively sample the configurational entropy to build a reliable temperature–composition phase diagram.

2.3 Monte Carlo Methods

Monte Carlo methods broadly refer to numerical schemes involving using input random numbers often to estimate integrals or sample through a stationary statistical distribution. Here, Monte Carlo sampling, specifically importance sampling as implemented using the Metropolis method,[101] is used to calculate the system free energy from statistically averaging through individual atomic configurations weighted with the right probability as dictated by statistical thermodynamics. The efficacy of this process depends on two factors, one sampling states with the correct probability, and two, doing so timely and efficiently. As discussed, the cluster expansion provides an accurate and acceptably quick method of evaluating the energy of a given microstate, but ensuring that the entire configurational space is sampled without being biased requires traversing through a Markov chain of configurations. These are a sequence of states that are constructed and recursively defined by modifying the previous state; formally the transition probability between successive states is defined strictly by the current state. In the Monte Carlo simulations in this work, the sequence of states is constructed by flipping the spin of the occupation variable at a single lattice site chosen at random (i.e. from $\sigma_i = 1$ to -1 or vice versa) in the case of simulations performed in an open ensemble (i.e. no spin conservation) or by picking two sites at random and exchanging the values of the occupation variables (ensuring spin conservation) for canonical simulations. The appropriate energy average can be computed directly through a series of accepting and states with the correct probability.

To ensure efficiency, the acceptance ratio should not remain excessively low which motivates more frequently sampling through states that have higher probability of acceptance, the basis for importance sampling. The algorithm implemented in this work is known as the Metropolis method,[101] where the system is perturbed (as discussed in the previous paragraph), and the acceptance/rejection scheme is as follows: if the energy of the new configuration is lower than previous, then the new configuration is accepted with probability 1, but if the energy of the new configuration is higher than previous, then the new configuration is only accepted with probability $exp(-H/kT)$, where H refers to the relevant free energy of the new configuration, k is Boltzmann's constant, and T is the system temperature. This results in a sequence of states sampled through with the correct probability as informed from statistical mechanics, and when the number of states generated is increased, the average energy computed approaches the exact value.

2.4 Experimental Agreement

Ultimately, the usefulness of these methods is determined by their ability to match and predict real measurable and experimental material's properties. First, DFT+U methods are better suited (than either GGA or LDA) to predict the redox voltage[12,102] of $LiFePO_4$ as well as the electronic band gap[103] and electron density of states.[103] Also, DFT+U methods, to good agreement with experiment, find positive mixing energies for structures with Li_xFePO_4 ($0 < x < 1$) composition (consistent with phase separation) unlike GGA or LDA.

Furthermore, using the cluster expansion method followed by Monte Carlo simulations accurately produces the features of the temperature–Li composition Li_xFePO_4 phase diagram, including phase separation at room temperature and a eutectoid transition to the solid–solution state at higher temperatures (as seen in **Figure 6**). To arrive at this result, the electronic substitutional degree of freedom must be explicitly considered in MC simulation, otherwise (only considering $Li^+/\square^-$ substitution) the computed phase diagram incorrectly predicts no eutectoid transition and instead a miscibility gap–type phase diagram.[16] This result has two obvious conclusions– first, the configurational electronic degree of freedom introduces important physics and must be explicitly considered, and second, the Hamiltonian generated from first principles is reliable to predict the properties of the Li_xFePO_4 system.

Chapter 3: Phase Diagram and Electrochemical Properties of Mixed Olivines from First–Principles Calculations

With the emergence of $LiFePO_4$ as a viable battery cathode material for large format batteries, cation-substituted phospho-olivine systems of the form $Li(Fe_{1-y}M_y)PO_4$ (M = Mn, Co) have gained the interest of battery researchers.[104-118] Specifically, the prospect of improved energy density over $LiFePO_4$ due to the higher redox potential of Mn^{3+}/Mn^{2+} compared to Fe^{3+}/Fe^{2+} (~4.1 V compared to ~3.4 V vs. Li/Li^+ [102]) has fuelled research into $Li(Fe_{1-y}Mn_y)PO_4$. Several questions in particular arise for mixed cation systems: $LiFePO_4$ is delithiated in a two-phase reaction forming $FePO_4$, and both phases tolerate only a small amount of off-stoichiometry.[119] Zhou *et al.* have shown that this two-phase reaction is unusual and driven by the strong electron-Li^+ interaction.[16] Dilution of the Fe sites by Mn may modify the phase behavior upon delithiation. In particular, Yamada *et al.* observe that the reduction of Fe^{3+} to Fe^{2+} shifts from two-phase to single-phase upon Li insertion for samples with $0.2 \leq y \leq 0.6$ (samples with $y = 0$, 0.2, 0.4, 0.6, 0.8, and 1.0 were tested, but those with $y \geq 0.8$ were unstable and did not completely retain the olivine structure in the delithiated state) while the Mn reaction remains entirely two-phase for $y \leq 0.8$.[104]

The approach here is to use first–principles calculation to study the temperature-composition phase diagram of $Li_x(Fe_{1-y}Mn_y)PO_4$ for different Mn-Fe compositions. In the case of $LiFePO_4$, both first principles investigations and

experiments have helped explain the observed low temperature phase-separation,[16,60,120] diffusion path of Li,[47-49] and high rate capability.[68] Of particular interest, first-principles calculations by Zhou *et al.*[16] which take into account both lithium/vacancy (Li^+/V) and electron/hole (e^-/h^+) configurational entropy have proven accurate in predicting the finite-T phase behavior of the Li_xFePO_4 system. In this work, a modification to that model has been incorporated to take into account Mn substitution of Fe. The resulting phase diagram of $Li_x(Fe_{1-y}Mn_y)PO_4$, voltage curves, and solubility limits are reported and compared to experiment. Also the change in polarization and hysteresis associated with the first order phase transition as Mn is substituted for Fe is studied.

3.1 Methods

The model used in this work builds on the approach proposed by Zhou *et al.*[16] which was used to determine the phase diagram of Li_xFePO_4. In that work, a coupled cluster expansion taking into account both ionic and electronic degrees of freedom was parametrized from *GGA+U ab-initio* calculations[12] and then used as a Hamiltonian in Monte Carlo simulations. By thermalizing both the Li^+/V and e^-/h^+ distributions, the free energy can be obtained for any temperature and Li concentration. In essence, a cluster expansion is a representation of the energy of the system in the phase space of all Li^+/V and e^-/h^+ distributions. The typical form of the energy model is a polynomial expansion in the occupation variables at each site:

$$E[\vec{\lambda},\vec{\varepsilon}] = J_\circ + J_i\lambda_i + J_{ij}\lambda_i\lambda_j + J_{ia}\lambda_i\varepsilon_a + J_{ab}\varepsilon_a\varepsilon_b + \ldots \qquad (14)$$

In **Equation *(14)***, λ_i represents occupancy of Li^+ site i, where $\lambda_i = 1$ represents Li^+ occupation and $\lambda_i = -1$ represents vacancy occupation. Similarly, ε_a represents occupancy of iron site a, where $\varepsilon_a = 1$ represents electron (Fe^{2+}) occupation and $\varepsilon_a = -1$ represents hole (Fe^{3+}) occupation. The J coefficients are the effective cluster interactions (ECIs), which reflect the aggregate effect of several physical factors such as electrostatics, screening, relaxation, covalency, etc. Because the Fe^{3+}/Fe^{2+} sublattice and the Li^+/V sublattice do not coincide, this is a coupled cluster expansion rather than a quaternary model.[121]

In this work, the same cluster expansion by Zhou *et al.*[16] was used, apart from one modification. In order to simulate the $Li_x(Fe_{1-y}Mn_y)PO_4$ system, we replace the transition metal point term by

$$\Delta E = \sum_{a\in \text{Mn Sites}} J_{Mn}\varepsilon_a + \sum_{a\in \text{Fe Sites}} J_{Fe}\varepsilon_a \qquad (15)$$

where $J_{Mn} = -4.2$ eV/2 and $J_{Fe} = -3.5$ eV/2. This represents the electron energy on the transition-metal site shifted down by 0.7 eV/2 on a fixed set of randomly chosen metal sites to account for Mn substitution. The factor of 1/2 is due to the fact that in this formulation, the redox reaction of hole to electron state is represented by the change in occupation variable ε_a from -1 to 1. It is well documented in both experiments and first-principle calculations that the difference between redox voltages of $LiMnPO_4$ and $LiFePO_4$ with respect to Li is ~0.7 V.[3,9,12] Since the point term ECI roughly corresponds to the chemical potential (i.e. the voltage), the model used in this work approximately takes into account the difference in redox potential

associated with Mn versus Fe. Since in our model Mn only modifies the interactions in Li_xFePO_4 by the e^-/h^+ site energy on the Mn position, higher-order Mn specific interactions such as Jahn-Teller distortion are not taken into account. The implications of this are discussed later.

Monte Carlo simulations were performed at different temperatures and degrees of Mn substitution in 6 x 12 x 12 and 12 x 12 x12 supercells (50,000 MC steps and 10,000 equilibration steps) where one cell corresponds to four $Li_x(Fe_{1-y}Mn_y)PO_4$ formula units. The free energy at each composition was obtained by integrating the relation between μ_{Li} and x_{Li}.

3.2 Results

To observe the effect of Mn on the voltage profile (Li content on x-axis, voltage on y-axis), Monte Carlo simulations were performed as a function of μ_{Li} at constant temperature for several Mn compositions. A typical calculated voltage profile output is shown in **Figure 11** for $y = 0.6$, showing noticeable hysteresis between charge (decreasing μ_{Li}) and discharge (increasing μ_{Li}). Free energy integration[122] is employed to obtain the equilibrium voltage profile and thus remove the hysteresis, the result of which is shown in **Figure 12** for several Mn compositions. The voltage curves show two plateaus at ~4 – 4.2 V and ~3.5 – 3.7 V, corresponding to the Mn^{3+}/Mn^{2+} and Fe^{3+}/Fe^{2+} redox couples, respectively. This can be readily seen since the widths of the plateaus (in Li composition) are roughly equal to the Mn/Fe compositions. The slight discrepancy of the calculated voltages

as compared to experiments is typical for the *GGA+U* approximation to obtain energies.[12] Constant voltage (chemical potential) regions correspond to first-order phase transitions and thus phase-separated regions in Li composition, and regions with varying voltage correspond to single-phase regions. Between the Mn^{3+}/Mn^{2+} and Fe^{3+}/Fe^{2+} plateaus is an extended single-phase region in which most Fe is oxidized while most Mn is not.

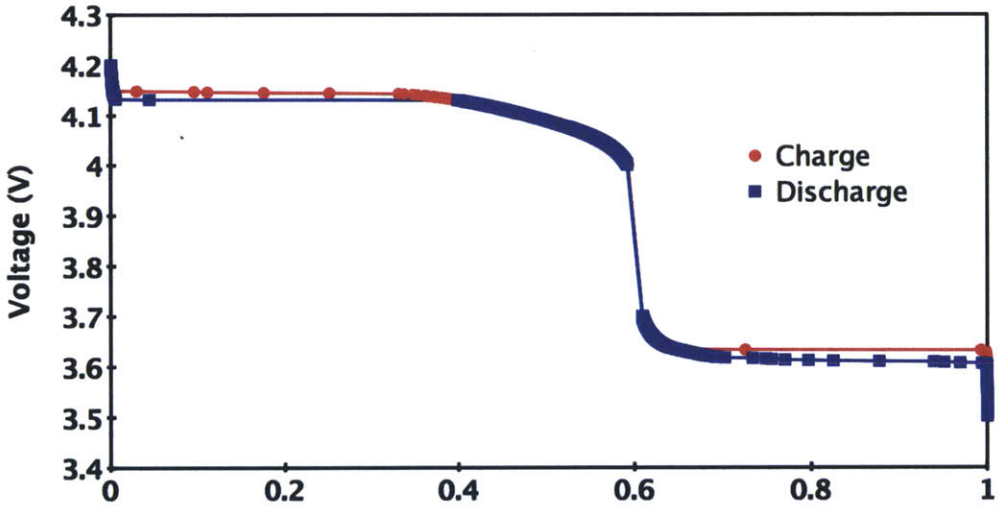

Figure 11: Calculated charge (red circles) and discharge (blue squares) voltage curve of $Li_x(Fe_{0.4}Mn_{0.6})PO_4$ at 300 K as determined by Monte Carlo (12 x 12 x 12 cell size) simulation.

The information determined from the voltage curves shown in **Figure 12** can be summarized by plotting the composition at the phase boundaries as shown in **Figure 13** with Li content (x) along the x-axis and Mn content (y) along the y-axis. Region (a) is phase-separated corresponding to the Mn^{3+}/Mn^{2+} couple; region (b) is single-phase corresponding to Mn^{3+}/Mn^{2+} (shaded region) and Fe^{3+}/Fe^{2+} (unshaded region); and region (c) is phase-separated corresponding to Fe^{3+}/Fe^{2+}. The dashed

line corresponds to the experimentally determined boundary between single-phase Fe^{3+}/Fe^{2+} and phase separated Fe^{3+}/Fe^{2+} by Yamada *et al.*[104]

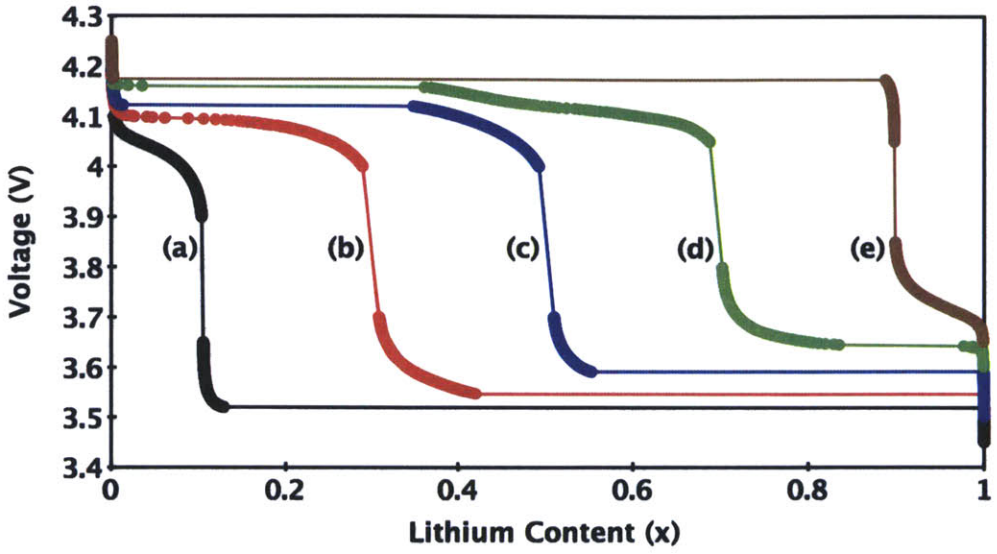

Figure 12: Equilibrium voltage curves of $Li_x(Fe_{1-y}Mn_y)PO_4$ at 300 K for (a) y=0.1, (b) y=0.3, (c) y=0.5, (d) y=0.7, and (e) y=0.9 as determined by Monte Carlo free energy integration.

The results from free energy integrations at different temperatures can be used to construct phase diagrams (Lithium content (x) along the x-axis and temperature along the y-axis) as shown in **Figure 14**. The phase diagram of Li_xFePO_4 ($0 \leq x \leq 1$), determined by both experiment[60,120] and first principle calculations,[16] shows a low temperature miscibility gap between $FePO_4$ and $LiFePO_4$ and a eutectoid transition to a solid solution phase. By substituting Mn on the Fe sublattice, the solid solution phase is stabilized at low temperature, and the phase diagram consists of two miscibility gaps at low temperature, the first between $Fe_{1-y}Mn_yPO_4$ (denoted α in **Figure 14**) and $Li_yFe_{1-y}Mn_yPO_4$ (denoted SS in **Figure 14**) and the second between $Li_yFe_{1-y}Mn_yPO_4$ (SS) and $LiFe_{1-y}Mn_yPO_4$ (denoted β in

Figure 14) where $0 \leq y \leq 1$. Several observations can be made from these results. First, the miscibility gap of the minority redox couple (e.g. Mn^{3+}/Mn^{2+} for $y < 0.5$ or Fe^{3+}/Fe^{2+} for $y > 0.5$) is lower in temperature than the miscibility gap of the majority redox couple. This can be understood from the fact that as a redox center is diluted in concentration, the effective interactions that create the miscibility gap are also diluted, thereby lowering the transition temperature to solid solution. Second, the solid solution phase penetrates between the two miscibility gaps down to low T at a Li composition that is approximately equal to the amount of Mn (y).

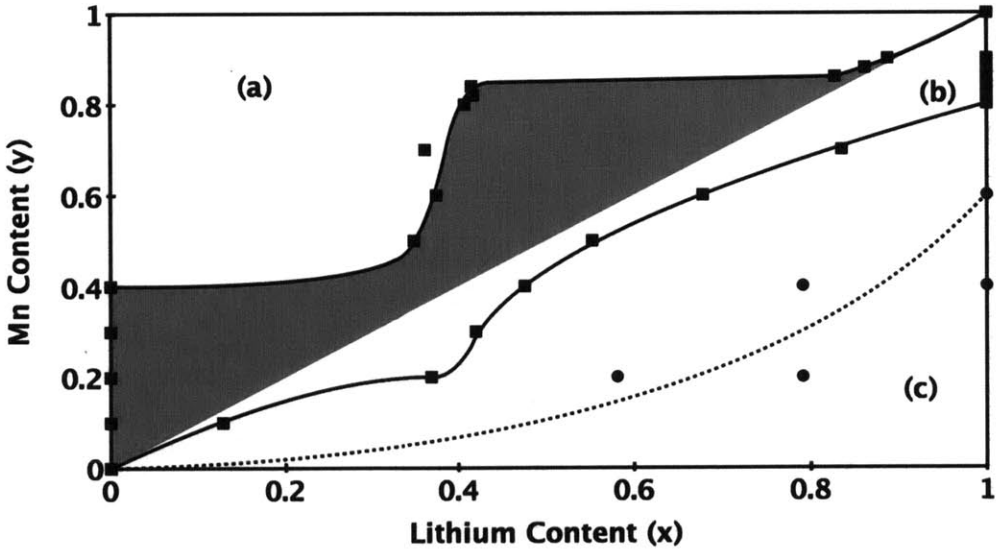

Figure 13: . Summary phase diagram of the $Li_x(Fe_{1-y}Mn_yPO_4)$ system at 300 K. Squares denote the boundaries between phase-separated and single-phase regions. Region (a) corresponds to a two-phase region associated with the Mn^{3+}/Mn^{2+} couple; Region (b) corresponds to a single-phase region associated with the Mn^{3+}/Mn^{2+} couple (shaded region) and the Fe^{3+}/Fe^{2+} couple (un-shaded); Region (c) corresponds to a two-phase region associated with the Fe^{3+}/Fe^{2+} couple. Circles correspond to the boundary between the two-phase and single-phase regions associated with the Fe^{3+}/Fe^{2+} couple as determined experimentally by Yamada *et al.* The dashed line denotes the experimentally determined boundary between single-phase Fe^{3+}/Fe^{2+} and phase-separated Fe^{3+}/Fe^{2+} as determined by Yamada *et al.*

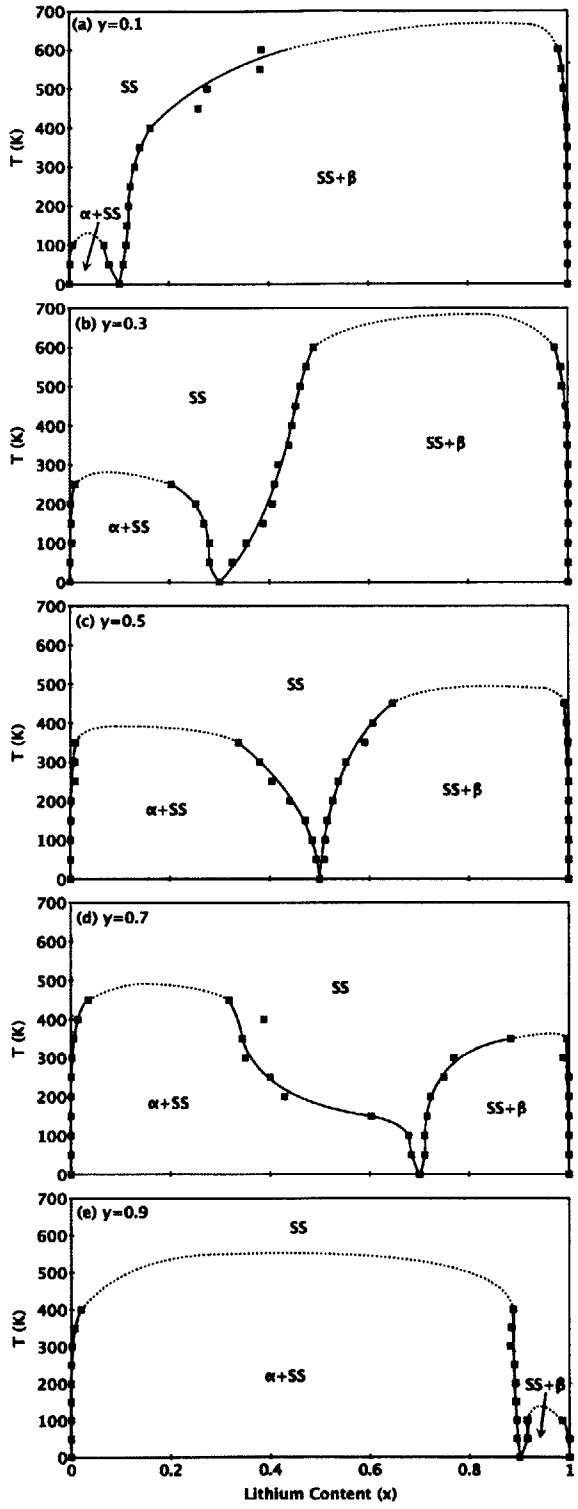

Figure 14: Calculated phase diagrams of $Li_x(Fe_{1-y}Mn_y)PO_4$ for (a) y=0.1, (b) y=0.3, (c) y=0.5, (d) y=0.7, and (e) y=0.9. Dashed line is speculative.

Figure 12 clearly shows that the voltage at which the phase transition occurs (hereafter referred to as the transition voltage) for both Fe^{3+}/Fe^{2+} and Mn^{3+}/Mn^{2+} couples increases as Mn content increases. The values of the transition voltage at 300 K for both couples as a function of Mn composition are catalogued in **Figure 15**. The voltage for both redox couples steadily increases with Mn composition. It is also shown that the phase transition shifts from first-order to second-order with increasing Mn substitution for the Fe^{3+}/Fe^{2+} couple, and the opposite is seen for the Mn^{3+}/Mn^{2+} couple.

Figure 16 shows the voltage of the Fe^{3+}/Fe^{2+} first-order phase transition upon both charge and discharge in the Monte Carlo simulation at different degrees of Mn

substitution and a comparison to the experiments performed by Nakamura *et al.*[112] on the $Li_xFe_{1-y}Mn_yPO_4$ system. Similarly, **Figure 17** shows the transition voltages upon charge and discharge of the Mn^{3+}/Mn^{2+} first-order phase transition with increasing Mn substitution. In both **Figure 16** and **Figure 17**, the same trend of increasing transition voltage with Mn substitution is observed. Also, the difference between the transition voltage determined upon charge and discharge (as discussed earlier and shown as the hysteresis in **Figure 11**) decreases with increasing Mn substitution for the Fe^{3+}/Fe^{2+} couple and increases for the Mn^{3+}/Mn^{2+} couple. This effect is shown clearly in **Figure 18**, which shows the polarization, defined as the difference between the charge and discharge transition voltages, at different degrees of Mn substitution for both the Fe^{3+}/Fe^{2+} and Mn^{3+}/Mn^{2+} couples.

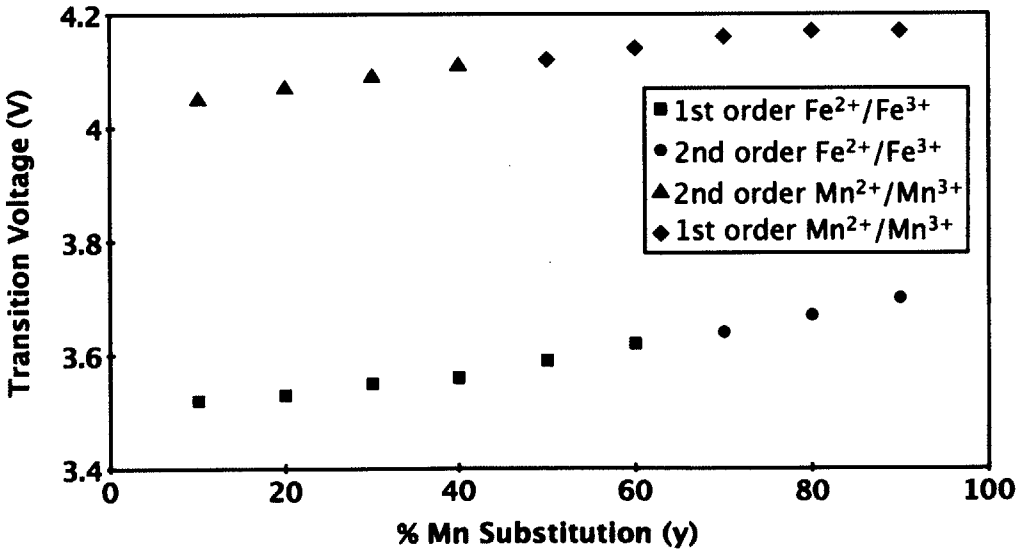

Figure 15: Equilibrium phase transition voltages at 300 K for Fe^{3+}/Fe^{2+} and Mn^{3+}/Mn^{2+}.

3.3 Discussion

Most of the trends we find compare well to the available experimental work. In experimentally determined charge-discharge curves and OCV measurements of the $Li_x(Fe_yMn_{1-y})PO_4$ system,[105,106,109,110] two plateaus at ~3.5 V and ~4.1 V are observed with a sloping (single-phase) region in between connecting the two, which shows good qualitative agreement with the data presented in **Figure 12**. Also, the experimentally obtained voltage curves show similar variation of the plateau width

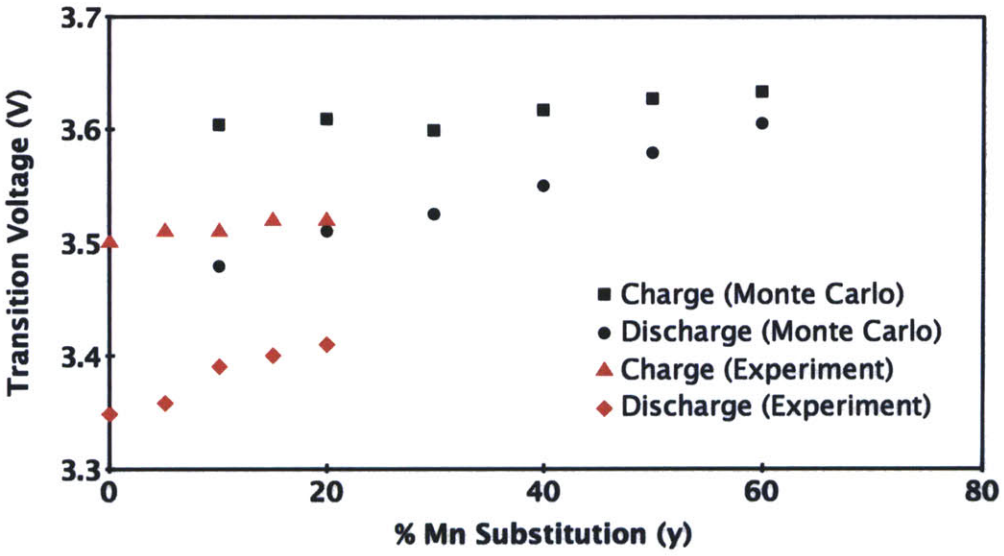

Figure 16: Figure 6. Phase transition voltages of the Fe^{3+}/Fe^{2+} couple as determined by Monte Carlo (12 x 12 x 12 cell size) simulation upon charge and discharge compared to experiments by Nakamura *et al.*

with increasing Mn composition as observed in **Figure 12**.[105,106,109,110] The trends observed in **Figures 15-18**, of increasing transition voltage and reduced polarization of the Fe^{3+}/Fe^{2+} transition with increasing Mn composition, are similarly reflected in experimental data.[112-114] Experimental polarization and transition voltage data of the Mn^{3+}/Mn^{2+} transition is unavailable, but experimental data in the $Li_x(Fe_{1-y}Co_y)PO_4$ system[115] reflects a similar trend of increasing

polarization and transition voltage of the Co^{3+}/Co^{2+} transition with increasing Co content. While this is a different system, it serves to illustrate how a higher redox couple is modified by the presence of the Fe^{3+}/Fe^{2+} couple.

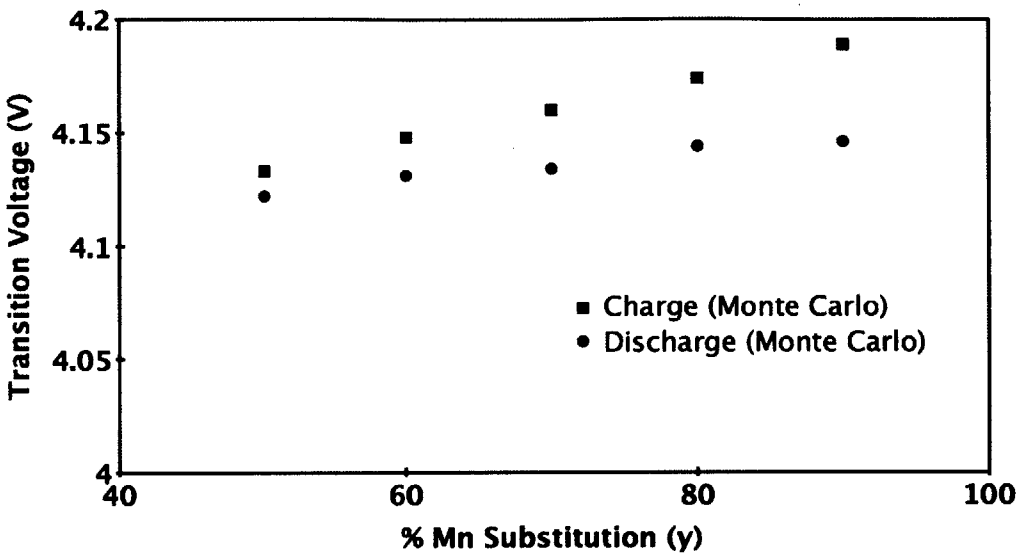

Figure 17: First-order phase transition voltages of the Mn^{3+}/Mn^{2+} couple as determined by Monte Carlo (12 x 12 x 12 cell size) simulation upon charge and discharge.

Experiments performed by Yamada *et al.*[104] do not produce a single-phase Mn^{3+}/Mn^{2+} region when the Mn couple is diluted by Fe as we find in the shaded portion of **Figure 13**. We believe that this difference between the calculations and experiments is due to the specific Jahn-Teller nature of Mn^{3+}. The Jahn-Teller distortion around Mn^{3+} leads to a large lattice distortion. Typically, when large elastic effects are present around impurities, solid solution regions are small, and a first order phase is preferred because a collective distortion of the unit cell results in less elastic strain energy than the combined elastic distortions around single impurities. The model used in this work represents Mn only by modifying the point

term in the coupled cluster expansion determined for the Li_xFePO_4 system, leaving all higher order ECIs unchanged. Thus, Mn-specific higher-order interactions are neglected in the model. These findings support the widely held opinion that the underlying physics of the $LiMnPO_4$ system are different compared to the $LiFePO_4$ system.[104,1231, 30] Hence, while the phase diagram of the pure Li_xMnPO_4 system has not been investigated, it seems likely that the temperature at which solid solution occurs is higher than in Li_xFePO_4 due to the stronger phase separation interaction caused by the Mn^{3+} Jahn-Teller distortion.

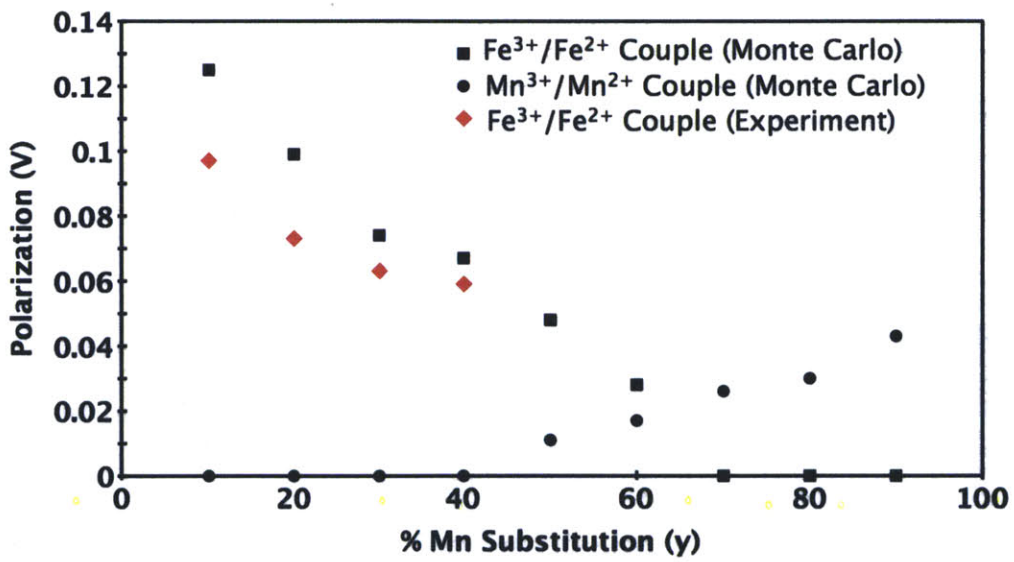

Figure 18: Polarization, defined as the difference between charge and discharge voltages, for Fe^{3+}/Fe^{2+} and Mn^{3+}/Mn^{2+} couples as determined by Monte Carlo (12 x 12 x12 cell size) simulation compared to experiments by Nakamura *et al.*

3.3.1 Existence of Single Phase Region

To understand the phase behavior in $Li_x(Fe_{1-y}Mn_y)PO_4$, we recollect the physical mechanism that is responsible for the two-phase region in Li_xFePO_4.[16] Both

the e^--h^+ and the Li^+-V interactions by themselves are of the ordering type and do not promote phase separation, but in Li_xFePO_4 the e^--Li^+ interaction is unusually strong due to the localized Fe^{2+}/Fe^{3+} states. As this interaction dominates, Li^+ strongly attracts Fe^{2+} which in turn attracts more Li^+, leading to a two-phase state. The Fe^{2+}-Li^+ (or Fe^{3+}-V) interaction is strong and favorable enough to overcome the Li^+-Li^+ (V-V) and Fe^{2+}-Fe^{2+} (Fe^{3+}-Fe^{3+}) repulsion when all Li is brought together. This allows us to understand the trends observed in this paper. It is important to realize that in a mixed cation system such as $Li_x(Fe_{1-y}Mn_y)PO_4$, the plateau voltages are not between fully lithiated (β) and delithiated (α) states, but between α and the solid solution (SS) phase (for Mn^{3+}/Mn^{2+}) and between SS and β (for Fe^{3+}/Fe^{2+}). As the Fe sites are diluted by Mn, the driving force for phase separation is decreased. In the SS where Fe is largely 3+ and most Mn is 2+, some Li^+ will have Mn^{2+} neighbors, and some will have Fe^{3+} neighbors. This unfavorable interaction raises the energy of the end member of each two-phase region and lowers the transition temperature to form solid solution as observed in **Figure 14**. One can also make a mean field argument to understand the tendency toward solid solution. In $Li_y(Fe_{1-y}Mn_y)PO_4$ the Fe^{3+}-V pairs that form are diluted by Mn^{2+}-Li^+ pairs, and hence their effective interaction energy (which is attractive) is diluted, leading to a lower transition temperature. The effect of random bond disorder in lattice models has been well studied in model systems and has been shown to transform first order transitions into second order ones and ultimately into glassy disordered states in agreement with our results.[124-127] The disorder in the low-T single phase which we

find between the two miscibility gaps for $y \approx x$ in $Li_x(Fe_{1-y}Mn_y)PO_4$ should be thought thereby as a glassy state rather than a high-T solid solution.

3.3.2 Increasing transition voltage

The variation in voltage of each redox couple with Mn/Fe concentration can be understood by considering the energy of the intermediate solid solution phase. The voltage in a two-phase reaction from $\alpha \rightarrow \beta$ is related to the energy of the two phases[98]:

$$\phi = -\left[\frac{E_{Li_{x_\beta}(Fe,Mn)PO_4} - E_{Li_{x_\alpha}(Fe,Mn)PO_4} - (x_\beta - x_\alpha)E_{Li}}{x_\beta - x_\alpha}\right] \qquad (16)$$

For the sake of argument, we neglect the small solubility in the fully lithiated and delithiated phase so that the plateau voltages for Mn and Fe are the following:

$$\phi_{Mn} \approx -\left[\frac{E_{Li_y(Fe_{1-y}Mn_y)PO_4} - E_{(Fe_{1-y}Mn_y)PO_4} - yE_{Li}}{y}\right] \qquad (17)$$

$$\phi_{Fe} \approx -\left[\frac{E_{Li(Fe_{1-y}Mn_y)PO_4} - E_{Li_y(Fe_{1-y}Mn_y)PO_4} - (1-y)E_{Li}}{1-y}\right] \qquad (18)$$

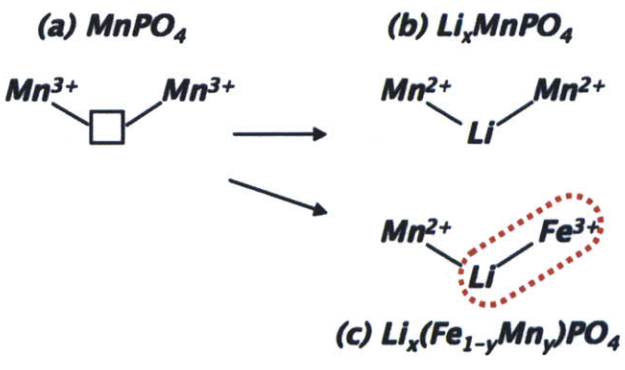

Figure 19: Schematic of Li site and nearest neighbor transition metal interactions before and after lithiation for the case of Li_xMnPO_4 compared to $Li_x(Fe_{1-y}Mn_y)PO_4$.

Consider, for example, the Mn redox voltage. In the delithiated state, all lithium vacancies are surrounded by hole states (Mn^{3+} or Fe^{3+}) just as in pure $MnPO_4$ as drawn schematically in **Figure**

19. Lithiation of pure $MnPO_4$ (labeled as (a) in **Figure 19**) leads to a state ($LiMnPO_4$ denoted as (b) in **Figure 19**) where all Li^+ are surrounded by electron states (Mn^{2+}). This is different in the case of $Li_x(Fe_{1-y}Mn_y)PO_4$. Lithiation on the Mn plateau leads to the intermediate phase ($\approx Li_y(Fe_{1-y}Mn_y)PO_4$ labeled as (c) in **Figure 19**) where Li^+ will be surrounded by some Mn^{2+} *and* some Fe^{3+}. The unfavorable Li^+-Fe^{3+} interaction (denoted by the dashed line in **Figure 19**) leads to a higher average energy per Li inserted than in the pure case, hence a lower voltage. This is shown in more detail in the **Appendix** in **3.5**. Hence, it is the increased energy of the intermediate disordered state which decreases the voltage of the high redox couple (Mn) and increases the energy of the low redox couple (Fe).

3.3.3 Reduced Polarization

The trend observed in **Figure 18**, that the polarization of the Fe^{3+}/Fe^{2+} transition reduces as Mn substitution increases, and vice-versa for the Mn^{3+}/Mn^{2+} transition, can be understood considering the composition difference between phases. Reduced polarization implies a reduced activation barrier to phase transition. At fixed temperature, the concentration difference (of Li) in the two-phase region between $Fe_{1-y}Mn_yPO_4$ (α) and $Li_yFe_{1-y}Mn_yPO_4$ (SS) monotonically decreases as the Mn composition y is increased. Similarly, the concentration difference in the two-phase region between $Li_yFe_{1-y}Mn_yPO_4$ (SS) and $LiFe_{1-y}Mn_yPO_4$ (β) monotonically increases with increasing y. For the Fe^{3+}/Fe^{2+} transition, systems with increased y must undergo less extreme fluctuations in Li concentration, so a

higher number of MC moves are accepted at lower overpotential. For the Mn^{3+}/Mn^{2+} transition, the same occurs as y is decreased. Hence, the decrease in plateau voltage polarization is a fairly straightforward consequence of a reduction in the composition difference between the initial and final state along the first order phase transition. We should point out that the polarization captured by a Monte Carlo simulation is only part of the polarization in a real electrode. Contributions from electronic resistance, surface charge transfer, strain accommodation, or interface velocity limitations cannot be modeled with our approach.

3.3 Conclusions

In this work, a framework based on first principles calculation to model the phase behavior and electrochemical trends of mixed olivine systems is presented, with specific emphasis on $Li_x(Fe_{1-y}Mn_y)PO_4$. Monte Carlo simulations using a Hamiltonian based on a modified coupled cluster expansion parametrized from *GGA+U ab-initio* calculations of Li_xFePO_4 were used to determine the phase diagram, voltage curves, and solubility limits of $Li_x(Fe_{1-y}Mn_y)PO_4$ with significant experimental agreement. Also, experimental trends in the transition voltage and polarization are mirrored in the calculations.

Given the efficacy of the model used in this work, several insights regarding the origin of the phase behavior and electrochemical trends observed in $Li_x(Fe_{1-y}Mn_y)PO_4$ can be made. The formation of the intermediate single-phase region (SS) centered at $Li_y(Fe_{1-y}Mn_y)PO_4$ and the lowered transition temperature to form solid

solution are the result of the dilution of phase-separating interactions. The attractive interaction between Mn^{2+} and Li^{+} is diluted by Fe^{3+} in the SS and vice versa. Similarly, the observed changes in plateau voltages can be explained by the change in energy of the intermediate solid solution. Due to the unfavorable Li^{+} coordination, the Fe^{3+} and Mn^{2+} states in the SS have higher energy than in their pure $FePO_4$ or $LiMnPO_4$ phases leading to higher and lower plateau voltages for Fe^{3+}/Fe^{2+} and Mn^{3+}/Mn^{2+} respectively. While we have focused on the $Li_x(Fe_{1-y}Mn_y)PO_4$ system, our model to explain the variation in redox plateau voltage is likely valid for other transition metal combinations as well, as all will have SS phases with unfavorable Li^{+}-M^{3+} (or V-M^{2+}) pairs separating the voltage plateaus. The trends in polarization arise as a result of the composition difference in Li between the intermediate solid solution and end-member phases.

3.5 Appendix: Determining Voltage Shifts in Mixed Olivines

Neglecting triplet interactions and the small solubility in the fully lithiated and delithiated phases, the shift in the transition voltage of the Mn^{3+}/Mn^{2+} and Fe^{3+}/Fe^{2+} redox couples is shown to be independent of the point energies (J_{Fe} and J_{Mn}) and depends entirely on the Mn content y and the difference in the pair interaction energies between the completely delithiated/lithiated phase and the intermediate phase $Li_y(Fe_{1-y}Mn_y)PO_4$.

Subtracting ***Eq. (16)*** from ***Eq. (17)*** yields $\Delta\phi_{Mn}$:

$$\Delta\phi_{Mn} \approx \frac{-(E_{Li_y(Fe_{1-y}Mn_y)PO_4} - E_{(Fe_{1-y}Mn_y)PO_4})}{y} + E_{LiMnPO_4} - E_{MnPO_4} \qquad \textit{(19)}$$

Substituting **Equations *(14)*** and ***(15)*** into **Equation *(19)***, where *PI* denotes the pair interaction energies:

$$\Delta\phi_{Mn} \approx \frac{-\left\{\left[J_o - J_{Fe}(1-y) + J_{Mn}y + PI_{Li_y(Fe_{1-y}Mn_y)PO_4}\right] - \left[J_o - J_{Fe}(1-y) - J_{Mn}y + PI_{(Fe_{1-y}Mn_y)PO_4}\right]\right\}}{y} + 2J_{Mn} \qquad \textit{(20)}$$

$$= \frac{PI_{Fe_{1-y}Mn_yPO_4} - PI_{Li_yFe_{1-y}Mn_yPO_4}}{y}$$

It should be noted that $PI_{Fe_{1-y}Mn_yPO_4} = PI_{LiMnPO_4} = PI_{MnPO_4}$ since all represent states where either all Li and *e* sites are occupied, or all are unoccupied, hence equivalent pair interactions. Because of unfavorable Li^+–Fe^{3+} interactions, $PI_{Li_yFe_{1-y}Mn_yPO_4} > PI_{Fe_{1-y}Mn_yPO_4}$, which explains the negative shift in the Mn^{3+}/Mn^{2+} transition voltage in $Li_x(Fe_{1-y}Mn_y)PO_4$. A similar line of reasoning can be used to explain the positive shift in the Fe^{3+}/Fe^{2+} transition voltage in $Li_x(Fe_{1-y}Mn_y)PO_4$.

Chapter 4: Particle Size Dependence of the Ionic Diffusivity

Diffusion constants are typically considered to be independent of particle size, with the benefit of nanosizing materials arising solely from shortened transport paths. Shown here for materials with one-dimensional atomic migration channels, the diffusion constant depends on particle size, with diffusion in bulk being much slower than in nanoparticles. Specifically, this model accounts for conflicting data on $LiFePO_4$, an important material for rechargeable lithium batteries, explaining why it functions exclusively on the nanoscale.

The benefit of nanosizing materials on bulk transport is conventionally attributed to the higher surface-to-volume ratio and reduced transport length in nanoparticles.[128] The diffusion constants which govern mass transport are not often regarded as size dependent, and macroscopic theories such as Fick's Law are implicitly assumed to be size-independent. The following work shows that for materials with a one-dimensional diffusion mechanism, nanosizing is particularly advantageous for ionic transport, as the intrinsic diffusion constant is scale dependent and significantly reduced at large particle size. $LiFePO_4$,[3] a well-known cathode material for rechargeable Li^+ ion batteries which only operates in batteries when in nanoform, is chosen as an illustrative example though the results should be applicable to all materials with 1D diffusion. The presence of point defects in one-dimensional transport paths makes the diffusion constant particle size-dependent, and explains how very high diffusivity at the nanoscale cannot be sustained in large

crystals. In addition, the observation of almost isotropic diffusion in large crystals with the strong anisotropic nature of Li mobility at the microscopic level is reconciled.

4.1 1D Diffusion and Li Transport in $LiFePO_4$

Computational[47,48] and experimental[49] studies of $LiFePO_4$ indicate that Li^+ ion migration occurs preferentially via one-dimensional channels oriented along the [010] direction of the orthorhombic crystal structure. These channels are shown in **Figure 20**. In fact, Li^+ ion diffusion along a perfect *b* direction is calculated to be so rapid ($D \sim 10^{-8}$ cm^2s^{-1}) that nano-size particles (100 nm) would be delithiated in much less than a second (0.01s), and micron-size particles (1 μm) in a second if

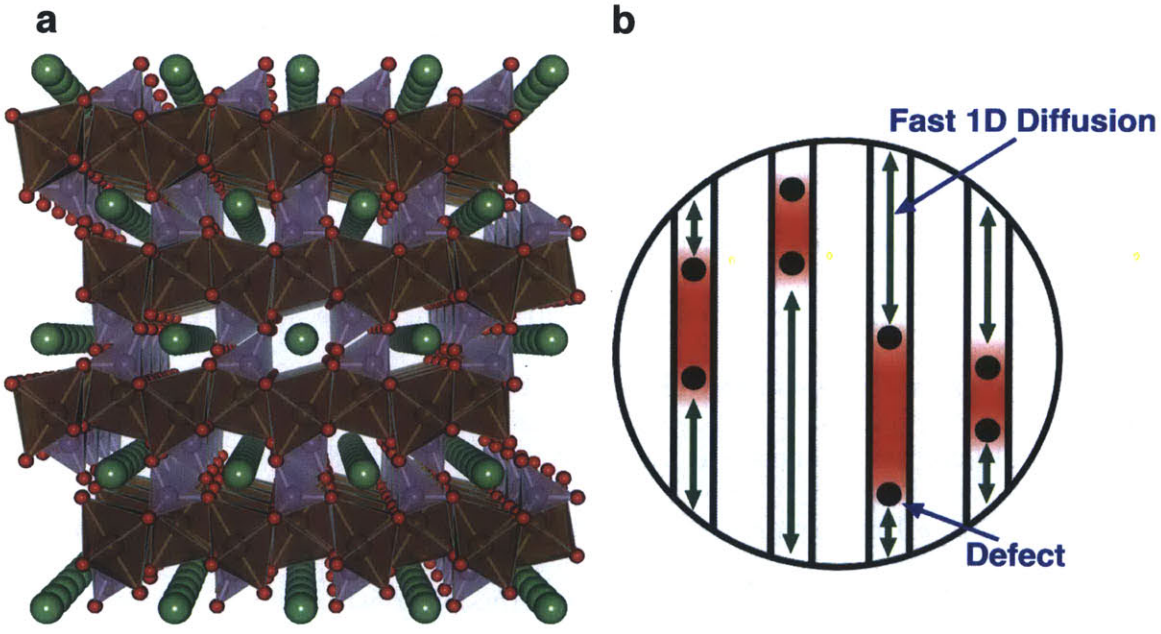

Figure 20: (a) Crystal structure of $LiFePO_4$ illustrating 1D Li^+ diffusion channels oriented along the [010] direction. (b) Schematic illustration of Li^+ diffusion impeded by immobile point defects in 1D channels.

intrinsic Li^+ mobility in the material were rate-controlling.[47] These predictions are certainly commensurate with the high rate performance observed in nano-sized $LiFePO_4$,[4,36,129] but studies of macroscopic $LiFePO_4$ exhibit much poorer and fundamentally different transport properties. Specifically, conductivity studies performed by Amin *et al.* on macroscopic (mm-scale) $LiFePO_4$ single crystals[130] indicate that at ~ 150 °C the chemical diffusion coefficient of lithium is ~ $10^{-9} - 10^{-10}$ $cm^2 \cdot s^{-1}$, but diffusion coefficient measurements taken along the *a*, *b*, and *c* axes from the same study also indicate that the Li^+ ion diffusivity is significantly less anisotropic compared to computational calculations,[47] and experimental observations[49] of the Li^+ positions.

One-dimensional diffusion is significantly different than diffusion in 2 or 3D. For instance, one-dimensional diffusion will be impeded by the presence of immobile and low-mobility defects (shown as black circles in **Figure 20b**) residing in the diffusion path. In dimension 2 or higher, immobile point defects will not affect the rate of two-dimensional diffusion, as the diffusing species can simply move around the defect. Hence, the presence of point defects will have a drastic effect on the rate at which ions can move through the crystal. For any finite concentration of point defects in 1D diffusion channels, there will be some channel length above which channels contain on average two or more point defects, thereby making sites inside the material inaccessible to Li^+ ions entering through either side of the tunnel opening (shown in red in **Figure 20b**). The channel-blocking concept allows the pathological nature of one-dimensional diffusion to be clearly illustrated. If the

diffusing ion cannot circumvent the defect, the macroscopic diffusion constant will become zero considering that $D \approx \langle r^2 \rangle / 2t$. If a channel is blocked, the mean-square displacement $\langle r^2 \rangle$ of an ion in the channel is capped, and at long times t the diffusivity goes to zero.

4.2 Point Defects and Blocked Capacity

For one-dimensional diffusion to be sustainable in the macroscopic limit, it is required that the diffusing species can cross over between different 1D channels. While this is unlikely in perfect materials, defects such as vacancies in the atomic sites between the channels can make crossover possible. For $LiFePO_4$, *ab initio* density functional theory in the GGA+U approximation with previously defined parameters[12] is used to perform an exhaustive search of formation energies of possible point defects involving combinations of Li^+ vacancies and interstitials, Li^+ on Fe^{2+} sites, Fe^{2+} on Li^+ sites, Fe^{3+} on Fe^{2+}sites, and Fe^{2+} vacancies (hereafter referred to using Kroger-Vink notation as V_{Li}^{-}, $Li_i^{\bullet}$, Li_{Fe}^{-}, $Fe_{Li}^{\bullet}$, $Fe_{Fe}^{\bullet}$, and V_{Fe}^{2-} respectively). The detailed results of this search will be reported elsewhere. For all reasonable conditions of the external chemical potential of each species, the nearest neighbor anti-site defect Li_{Fe}^{-}–$Fe_{Li}^{\bullet}$ consistently has the lowest formation energy of about 0.515 – 0.550 eV (details are shown in **4.6.1**). This finding compares well with both existing theoretical and experimental studies of defects in $LiFePO_4$: using empirical potentials, Islam *et al.*[48,131] also determine that the formation energy for the bound anti-site defect is the lowest of all considered defects ($E_{antisite}$ =

0.74 eV), and in studies by Chung *et al.*[132,133] using high-angle annular dark-field (HAADF) scanning transmission electron microscopy (STEM), antisite defects are observed with concentration ~ 1% at 600 °C. At temperatures considered in this study, $Fe_{Li}^{\bullet}$ is expected to be comparatively immobile with respect to the time scale of Li^+ migration within the 1D channels, which is in line with the excellent cycling capability and capacity retention of this material.

Li^+ sites situated between $Fe_{Li}^{\bullet}$ defects cannot be reached from the surface of a particle unless there is an alternative transport path available (to be discussed later), and these Li^+ sites are hereafter referred to as part of the "blocked" capacity. While in very large particles most sites will be blocked by defects, the total channel length between surfaces in nanoparticles is small, resulting in channels containing very few or even zero defects. For instance, for particles smaller than 60 nm, 1% $Fe_{Li}^{\bullet}$ population leads to on average fewer than two defects residing in each channel, and therefore no blocked Li^+ sites (the distance between Li^+ sites along the 1D channel in $LiFePO_4$ is ~ 3 Å). A more rigorous probabilistic model of the fraction of "unblocked" sites can be constructed assuming that the creation of defects is a Poisson process, the location of defects is spatially uniform, and the capacity situated between two defects in the same Li^+ ion channel (shown as red in **Figure 20b**) is blocked. The details of this derivation are described in **4.6.2**, but the mean fraction of unblocked capacity, *C*, (reachable from the surface without going through defects) is given by:

$$C = \frac{2 - (2 + N \cdot p_{def})\exp(-N \cdot p_{def})}{N \cdot p_{def}} \qquad (21)$$

where N is the number of Li^+ sites along a 1D channel, and p_{def} is the concentration of defects. The expected fraction of unblocked capacity (**Equation *(21)***) as a function of one-dimensional channel length is plotted in **Figure 21** for various defect concentrations. Given the formation energy of the bound anti-site defect, the equilibrium defect concentration at typical solid-state synthesis temperatures (800 - – 1100 K) is ~ 0.1 – 0.5 %, which can be considered as a theoretical thermodynamic limit representing a lower bound on the actual defect concentration in real materials, which are often synthesized via non-equilibrium techniques using precursors and contain trace quantities of impurities. Specifically, in $LiFePO_4$ single crystals grown by optical floating zone method, Amin *et al.*[56] observe ~ 2.5 – 3 % $Fe_{Li}^{\bullet}$, and in hydrothermally synthesized $LiFePO_4$ Yang *et al.*[7] observe up to ~ 7 – 8 % $Fe_{Li}^{\bullet}$.

The results in **Figure 21** hint at how effective Li^+ mobility in $LiFePO_4$ may depend on particle size. For small particles, most of the channels will contain one or zero defects, and all sites are available by rapid diffusion through unblocked channels. For larger particles, most Li^+ sites will not directly be accessible from the surface. In the latter situation, the effective Li^+ diffusivity will be zero unless Li^+ ions can circumvent defects by migrating between different channels.

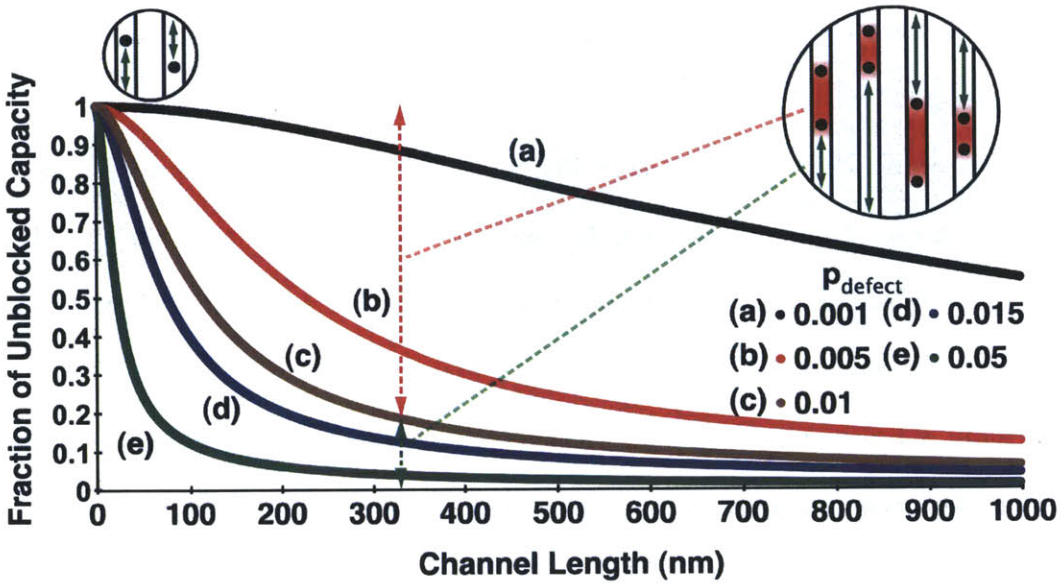

Figure 21: Expected unblocked capacity vs. channel length in LiFePO4 as determined by Eq. 19 for various defect concentrations.

4.3 Li Cross-over and Effects on Bulk Li Diffusivity

The $Li_{Fe}^{-}-Fe_{Li}^{\bullet}$ anti-site defect offers such an opportunity for Li^{+} to cross over between channels. Activation energies for Li^{+} migration past $Fe_{Li}^{\bullet}$ were calculated using the generalized gradient approximation (GGA) to density functional theory as implemented in the Vienna *Ab Initio* Simulation Package (VASP). Elastic band calculations were performed in supercells containing up to eight unit cells and four images in the dilute vacancy limit. Various migration paths conforming to Li^{+} circumventing $Fe_{Li}^{\bullet}$ were considered, and it was determined that the lowest energy path possible occurs by Li^{+} migrating to the nearest Li^{+} channel through a vacant intermediate Fe^{2+} site, with an activation barrier of 0.491 eV (details in **4.6.1**).

Given the mechanism of defect circumvention and its migration barrier, the bulk diffusivity of lithium in $LiFePO_4$ containing defects can be determined by employing a modified

random walk model (described in the **4.6.4**) in a potential landscape with activation energies corresponding to fast 1D diffusion along the [010] direction and defect circumvention. Along the [010] direction, if the migrating atom does not neighbor a defect it is equally likely to move forward as backward in the Li^+ channel. However, if the migrating atom lies directly adjacent to the defect, it is likelier to move in the direction away from the defect rather than circumvent it because the activation barrier associated with a back-jump is much smaller, which leads to significantly reduced mean-square displacement and thus reduced diffusion coefficient with increasing defect concentration.

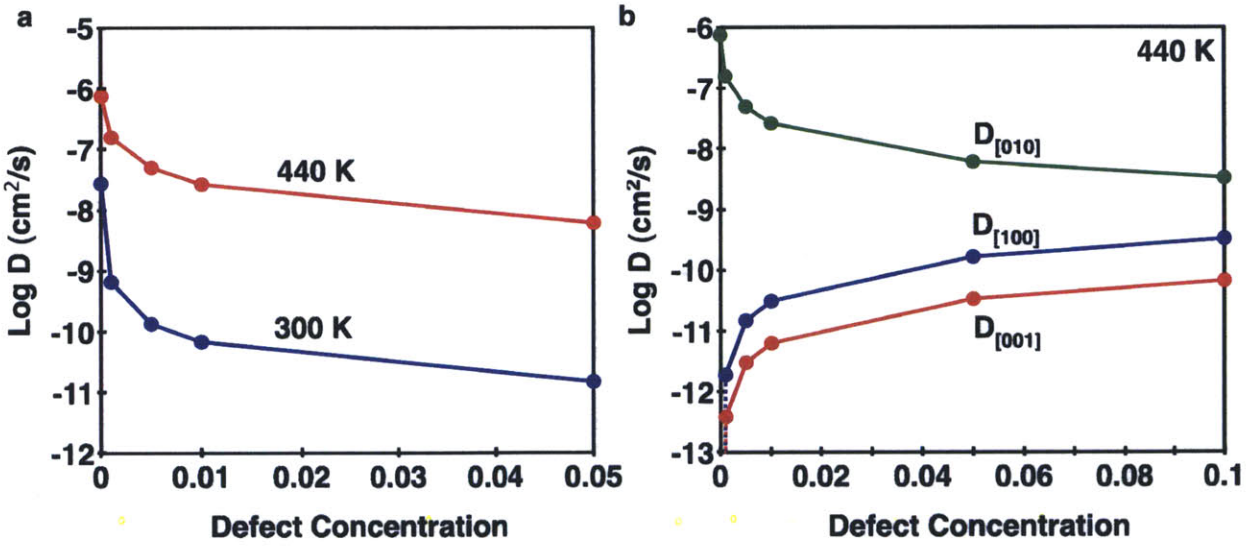

Figure 22: (a) Variation of the Li-vacancy self-diffusion along [010] with defect concentration at T = 300 K (red) and at T = 440 K (blue). (b) Variation of the Li-vacancy self-diffusion $D_{[100]}$ (blue), $D_{[010]}$ (green), and $D_{[001]}$ (red) with defect concentration at T = 440 K.

The focus in this work centers on vacancy diffusion over lithium sites as it is a more intrinsic property than the lithium diffusion which depends on the Li-vacancy concentration. The Li-vacancy concentration is set by the degree of lithiation (in the single-phase region) up to a maximum value reached at the

solubility limit, estimated to be up to ~ 11% by Yamada *et al.*[134] The vacancy self-diffusion coefficient along [010] at 300 and 440 K as a function of defect concentration is shown in **Figure 22a**. To determine the Li^+ diffusivity in the dilute vacancy limit, the values shown in **Figure 22** should be multiplied by a prefactor including the equilibrium vacancy concentration. The presence of defects is shown to significantly decrease the bulk 1D diffusivity along Li^+ tunnels even with defect concentrations less than 0.01. At room temperature, the drop in diffusivity is more drastic, reducing by more than 2 orders of magnitude with p_{defect} = 0.005 ($D_{[010]}$ = ~ 10^{-10} cm^2/s). It should be noted that the cross-over mechanism involves a net displacement in the <101> directions and is consequently the predominant mechanism for diffusion in the [100] and [001] directions. At 440 K, $D_{[100]}$ and $D_{[001]}$ as a function of defect concentration are shown in **Figure 22b** and compare well with single-crystalline $LiFePO_4$ diffusivity measurements performed by Amin *et al.* who report ~ 2.5 – 3 % anti-site defects.[51,56] Compared to the defect-free scenario, there is a sharp reduction in the anisotropy of the diffusivity in the presence of defects which corroborates observations of 2D diffusion behavior.[51,56] The shift of a diffusion mechanism from 1D to either 2D or 3D due to the presence of defects is a general materials concept rather than a unique property of $LiFePO_4$, as the same phenomenological behavior has explained both the deviation from 1D diffusion of self-interstitial crowdion defects in materials undergoing irradiation damage[135] as well as the relative anisotropy of Li^+ conductivity in ramsdellite $Li_2Ti_3O_7$.[136]

4.4 Particle Size Dependence

To illustrate the effect of point defect obstructions on rate performance of $LiFePO_4$ across varying particle size and defect concentration, we look to the characteristic time (defined by *(2)* and plotted in **Figure 23**) for Li^+ to diffuse along the [010] direction, which takes into account fast diffusion through unblocked capacity (governed by $D_{unblocked}$ as calculated by Morgan *et al.*[47]) and slower diffusion (governed by $D_{blocked}$ as shown in **Figure 22a**) through trapped capacity between defects:

$$t = t_{blocked} + t_{unblocked} = \frac{x^2_{blocked}}{D_{blocked}} + \frac{x^2_{unblocked}}{D_{unblocked}}. \quad (22)$$

The average blocked and unblocked diffusion lengths, $x_{blocked}$ and $x_{unblocked}$, are determined from the product of particle length and the fraction of blocked/unblocked capacity as calculated in **Equation *(21)***. From **Figure 23**, the impact of defects is striking – even when the particle size is reduced to 100 nm, there is an order of magnitude decrease in the characteristic diffusion time with just 0.05 % defect concentration and an additional order of magnitude decrease at 1 % defect concentration.

In a $\log(t) - \log(x)$ plot, Fickian diffusion appears as a straight line with slope of two as diffusion time scales as the square root of distance. **Figure 23** shows that this is only the case for a defect-free crystal. In the presence of point defects, power law behavior of time is only observed for very small particles (with high D) or very large particles (with smaller D). Hence, there is a particle size regime where

diffusion transitions from the nano-regime to the bulk and diffusion times do not scale with length as one would expect from Fick's law.

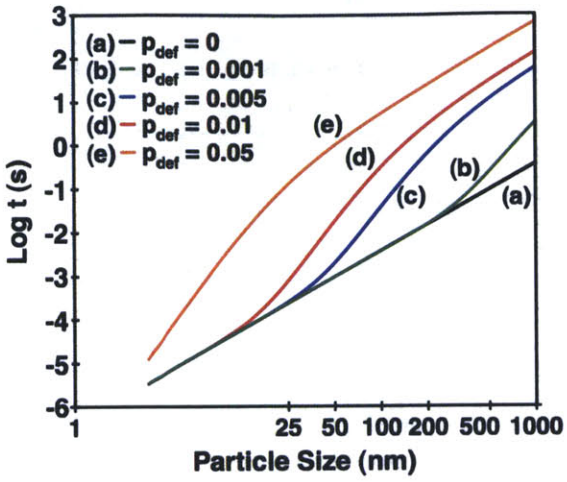

Figure 23: Characteristic diffusion time to traverse a particle along the [010] direction as defined by *Eqn. (2)* plotted as a function of particle size for varying defect concentrations.

4.5 Conclusions: Why nano–$LiFePO_4$ performs better

In this work, it is shown that the diffusion constant of ions moving in one-dimensional channels is not intrinsic, but determined by particle size as soon as point defects are present. These point defects restrict the root-mean square displacement of the ions and without migration paths around defects, the diffusion constant in a macroscopic crystal would tend to zero. Specifically for $LiFePO_4$, first principles methods confirm that the channel-blocking defects are likely Li_{Fe}^{-}–$Fe_{Li}^{\bullet}$ anti-sites, and that migration of Li^{+} through the vacant Fe^{2+}-site is a much higher energy process than Li^{+} migration within the channels. This process makes the diffusion constant of Li^{+} dependent on both particle size and defect concentration. For small particles, most channels have zero or one defect in them, making all sites

accessible by very rapid migration of Li^+ through the channels. For larger particles, multiple cross-overs are required between channels to reach all Li^+ sites, making transport intrinsically slower. By calculating effective diffusion constants, the impact of just modest concentrations of anti-site defects becomes apparent: with > 0.005 defect concentration, the fraction of unblocked capacity is negligible at the micron-scale, and the bulk diffusivity along the [010] direction decreases by over two orders of magnitude at room temperature. Also, by forcing cross-over between Li^+ tunnels in large crystals, the dimensionality of the diffusion mechanism shifts from 1D to 2D or 3D as the anisotropy of the diffusion coefficients reduces in the presence of defects. Both of these findings reconcile discrepancies in the measurement of Li^+ diffusivity in $LiFePO_4$ across different particle sizes and synthesis methods. Specifically, the results of Amin *et al.*,[51,56] which show reduced Li^+ diffusivity and imply a 2D diffusion mechanism in mm-size $LiFePO_4$ single crystals, are well understood in the context of our model of Li^+ diffusion in the presence of defects. Without invoking surface effects and changes in solubility with particle size, the deleterious effect of channel-blocking point defects also provides a convincing argument as to why the general performance of nano-$LiFePO_4$ is so much better than its bulk counterpart.

In this study, the focus has been on the impact of anti-site defects, but off-stoichiometric defects involving $Fe_{Li}^{\bullet}$, albeit fewer in population due to higher formation energy, will have much higher Li^+ migration barriers for defect circumvention. For instance, the cross-over migration of Li^+ past anti-site defects as

described earlier cannot occur in Fe-excess $LiFePO_4$ as all intermediate Fe^{2+} sites always remain occupied by Fe^{2+}. Consequently, any trapped capacity between two such defects may remain entirely inaccessible at any reasonable rate of charge/discharge.

While $LiFePO_4$ performs very well as a Li-battery cathode when in nanoform, the use of nanoparticles leads to lower packing density in the electrodes, reducing the energy density of batteries. For many applications, including portable electronics and electrified vehicles, the volume of the battery is as important a consideration as weight, and larger particle size $LiFePO_4$ could significantly increase the energy content of cells. These results clarify that mitigation of channel-blocking point defects now becomes a critical design consideration in the $LiFePO_4$ synthesis process, and the remaining future challenge is to synthesize near defect-free $LiFePO_4$ at larger particle sizes. While the particle size effects studied in this work arise due to one-dimensional diffusion in defective $LiFePO_4$, the same concepts can be applied to other potential battery materials.

4.6 Appendices

4.6.1 Defect Formation Energies

Charge-neutral point defects containing $Fe_{Li}^{\bullet}$ considered in this study include the nearest-neighbor antisite defect, $Li_{Fe}^{-} - Fe_{Li}^{\bullet}$, as well as off-stoichiometric combinations $V_{Li}^{-} - Fe_{Li}^{\bullet}$ and $V_{Fe}^{2-} - 2\,Fe_{Li}^{\bullet}$. The chemical potentials for the species

removed or added to the synthesis environment need to be known. A reasonable range for these chemical potentials was determined from the first principles Li-Fe-P-O phase diagram determined by Ong *et al.*[23] More specifically, a given off-stoichiometry and oxygen chemical potential defines the relevant three-phase equilibrium reference state. For example, for the V_{Li}^{-}-$Fe_{Li}^{\bullet}$ defect, there is Fe excess and Li deficiency in the ratio of 1:2. At $\mu_{O2} = -11.52$ eV the three phase equilibrium with this stoichiometry occurs between $LiFePO_4$, Fe_2O_3, and $Fe_7(PO_4)_6$ as shown in the work by Ong *et al.*[23] The chemical potentials of Li, Fe, and P in this three-phase equilibrium are the limiting chemical potentials at which $LiFePO_4$ with this off-stoichiometry can exist without decomposing to other phases in the three-phase equilibrium. Below in **Figure 24** is a plot showing the defect formation energies of the aforementioned defects for the range of appropriate oxygen chemical potentials where $LiFePO_4$ is stable. From the above plot, it is clear that the nearest neighbor

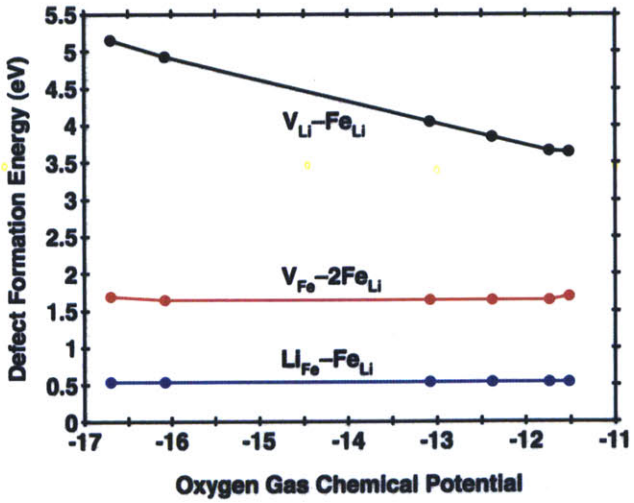

Figure 24: Formation energies of defects containing FeLi vs. oxygen gas chemical potential in the range where LiFePO4 is stable

antisite defect has the lowest formation energy for all reasonable values of the oxygen chemical potential.

4.6.2 Unblocked Capacity in $LiFePO_4$ Channels Containing Defects

The fraction of unblocked capacity C available in a single Li^+ ion channel containing N total sites and D defects (located at $d_1, d_2, \ldots, d_D$) can be described by

$$C = 1 - \frac{1}{N}(\max\{d_1, d_2, \ldots, d_D\} - \min\{d_1, d_2, \ldots, d_D\} + 1) \qquad (23)$$

and the probability density of the total number of defects D in a channel assuming defect creation is a Poisson process is

$$\mathrm{P}(D = d) = e^{-\lambda}\frac{\lambda^d}{d!} \qquad (24)$$

where λ is the Poisson parameter defined as $\lambda = N \cdot p_{defect}$, where p_{defect} is equal to the concentration of defects. Assuming N is large, the channel is modeled as the continuum [0,1] and for any x in this closed interval,

$$\mathrm{P}(C < x) = \sum_{d=0}^{\infty} \mathrm{P}(D = d) \cdot \mathrm{P}(C < x \mid D = d). \qquad (25)$$

To calculate the probability distribution for the capacity given a fixed number of defects, we consider that there are exactly $d > 2$ defects present in a given Li^+ ion channel. In order for $C < x$, the maximum distance between any two defects must be $< 1 - x$. There are $d(d-1)$ ways to choose one defect to be closest to 0 and a second defect to be closest to 1 with all remaining defects in between. Therefore

$$\frac{1}{d(d-1)}\mathrm{P}(C < x \mid D = d) = \int_0^x dx_1 \int_{1-x+x_1}^1 dx_1 \int_{x_1}^{x_2} dx_3 \ldots \int_{x_1}^{x_2} dx_d \qquad (26)$$

$$= \int_0^x dx_1 \int_{1-x+x_1}^1 dx_1 (x_2 - x_1)^{d-2}. \qquad (27)$$

Evaluating this integral leads to

$$\mathrm{P}(C < x \mid D = d) = 1 - (1-x)^d - dx(1-x)^{d-1}. \qquad (28)$$

For $d = 0$ or $d = 1$, ***(6)*** reduces to 0, as expected. Combining ***(24)***, ***(25)***, and ***(28)*** yields

$$\mathrm{P}(C < x) = e^{-\lambda}\sum_{d=0}^{\infty}\frac{\lambda^d}{d!} - e^{-\lambda}\sum_{d=0}^{\infty}\frac{[\lambda(1-x)]^d}{d!} - e^{-\lambda}\lambda x\sum_{d=0}^{\infty} d\frac{[\lambda(1-x)]^{d-1}}{d!} \qquad (29)$$

$$= 1 - e^{-\lambda x} - \lambda x e^{-\lambda x}. \qquad (30)$$

From ***(24)***, the probability of complete unblocked capacity occurs only if there is one defect or no defects present in the channel:

$$\mathrm{P}(C = 1) = (1+\lambda)e^{-\lambda}. \qquad (31)$$

From ***(30)*** and ***(31)***, the expected unblocked capacity and variance are calculated from standard statistics definitions:

$$\mathrm{E}(C) = \frac{2 - (2+\lambda)e^{-\lambda}}{\lambda}. \qquad (32)$$

$$\mathrm{Var}(C) = \frac{2 + (2 - 2\lambda - 2\lambda^2)e^{-\lambda} - (2+\lambda)^2 e^{-2\lambda}}{\lambda^2}. \qquad (33)$$

4.6.3 Crossover Migration Path

The relevant migration barriers involved in Li^+ crossover migration are shown below in **Figure 25** and **Figure 26**. In **Figure 25**, it is shown that migration of Li^+ (adjacent to $Fe_{Li}^{\bullet}$ in the 1D diffusion channel) to the nearest vacant Fe site is barrierless, meaning that the Fe site will be consistently populated by Li^+. In **Figure 26**, the migration energy of Li^+ from the Fe site to a vacant Li^+ site in the neighboring Li^+ channel is shown to be the ~ 0.491 eV, the net activation energy associated with crossover migration.

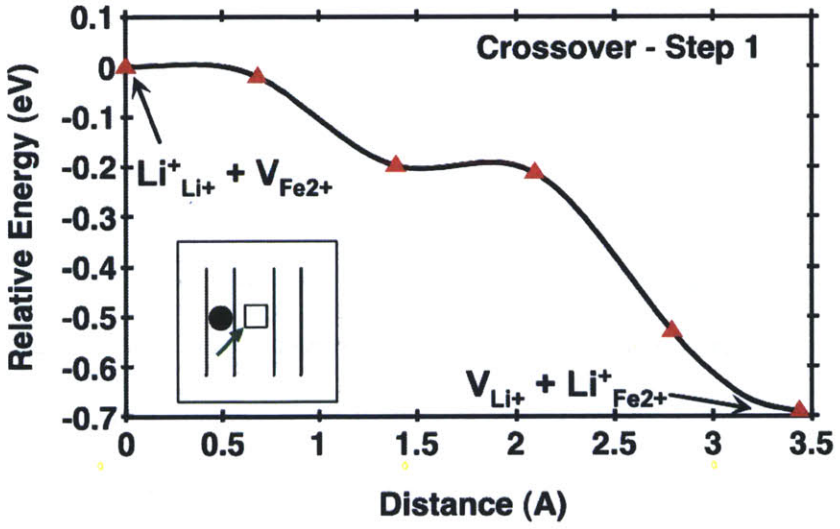

Figure 25: Migration path of Li^+ in a blocked channel to the nearest vacant Fe site. Open square is Li-vacancy, and solid circle is Fe_{Li}.

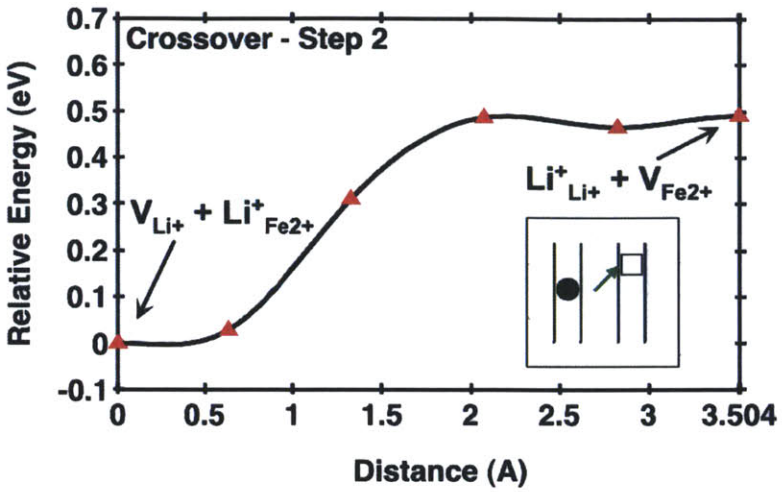

Figure 26: Migration path of Li^+ from the Fe site to the neighboring Li^+ diffusion channel. Open square is Li-vacancy, and solid circle is Fe_{Li}.

4.6.4 1D Random Walk Model

In the [010] direction, we used a modified 1D random walk model that accounts for local correlation to determine the diffusion coefficient. The potential landscape of the diffusion path in the [010] direction is depicted schematically in **Figure 27**. The shallow activation barriers (270 meV as calculated in previous work[47]) are associated with fast hops unimpeded by defects, and the higher activation barriers (491 meV as described earlier) are associated with the slower crossover mechanism. If the migrating atom does not neighbor a defect, it is equally likely to move forward as backward as shown in *(a)* in **Figure 27**. However, if the migrating atom lies directly adjacent to the defect, it is likelier to move in the direction away from the defect rather than circumvent it (as shown in *(b)* in **Figure 27**) because the activation barrier associated with a back-jump is much smaller. Assuming defects are dispersed at random, the diffusion behavior becomes uncorrelated at larger length scales. For uncorrelated diffusion, the 1D diffusion coefficient is be described by

$$D = \frac{\Gamma\langle r^2 \rangle}{2} \qquad (34)$$

where Γ is the jump frequency and $\langle r^2 \rangle$ is the mean-square jump distance. To calculate D for a system that undergoes locally correlated but macroscopically uncorrelated diffusion, we determine Γ and $\langle r^2 \rangle$ not for single discrete hops, but rather for several hops corresponding to a mean-square jump distance at a length scale where diffusion can be assumed to be uncorrelated. For example, as shown in **Figure 27**, it is equally likely that a migrating atom initially equidistant from its two neighboring defect blockages moves past the defect to the right as to the left, which now defines r.

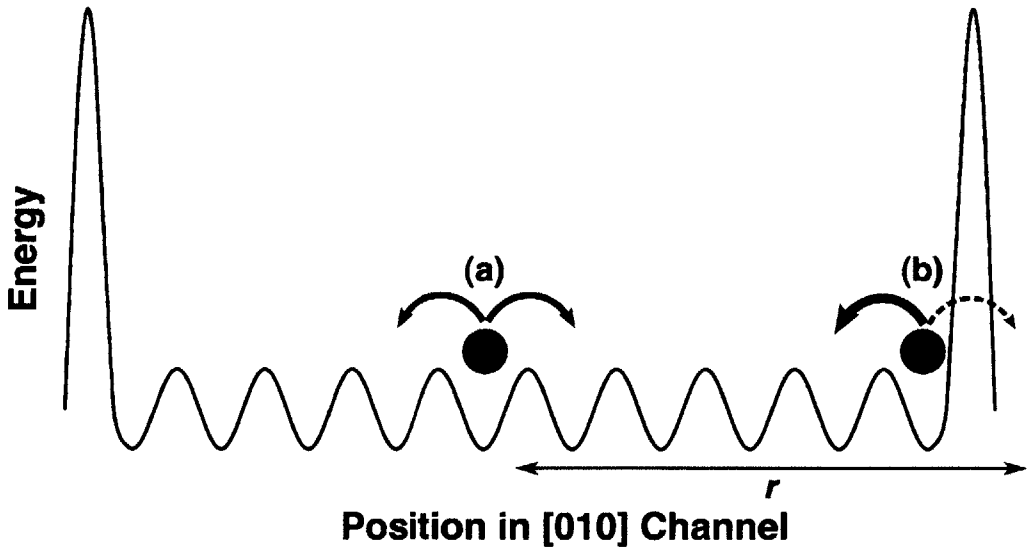

Figure 27: Schematic depiction of potential landscape along Li^+ diffusion channels oriented along [010] containing shallow migration barriers associated with lattice diffusion and heightened migration barriers associated with defect circumvention. At position (a), Li^+ is equally likely to jump to the left as to the right, but at position (b), Li^+ will jump to the right with significantly reduced probability.

To calculate Γ, we first determine through direct numerical simulation the average number of jumps corresponding to a mean-square displacement of $\langle r^2 \rangle$,

that is how many jumps are required to circumvent the nearest defect obstruction, and note the time associated with each individual hop,

$$\tau = \left(\nu \cdot \exp\left(-\frac{E_a}{kT} \right) \right)^{-1}, \qquad \textbf{(35)}$$

where ν is the "characteristic attempt frequency" (assumed to be ~ 10^{12} Hz, on the order of atomic vibrational frequencies) and E_a is the activation barrier associated with the jump. By combining ***(34)*** and ***(35)***, the diffusion coefficient along the [010] direction for varying defect concentration has been determined.

Chapter 5: Kinetics of Non-equilibrium Li Insertion in $LiFePO_4$

Li-ion batteries are a key technology for multiple clean energy applications. Their energy and power density is largely determined by the cathode materials, which store Li by incorporation into their crystal structure. Most commercialized cathode materials, such as $LiCoO_2$,[137] $LiMn_2O_4$,[14] $Li(Ni,Co,Al)O_2$, or $Li(Ni,Co,Mn)O_2$[138] form solid solutions over a large concentration range, with occasional weak first-order transitions due to ordering[137] of Li or electronic effects.[15] An exception is $LiFePO_4$, which stores Li through a two-phase transformation between $FePO_4$ and $LiFePO_4$.[16,60,120,134] Notwithstanding having to overcome extra kinetic barriers, such as nucleation of the second phase and growth through interface motion, the observed rate capability of $LiFePO_4$ has become remarkably high.[4,38,139] In particular, once transport limitations at the electrode level are removed through carbon addition and particle size reduction, the innate rate capability of $LiFePO_4$ is revealed to be very high. It is demonstrated here that the reason $LiFePO_4$ functions as a cathode at reasonable rate is the availability of a single-phase transformation path at very low overpotential, allowing the system to bypass nucleation and growth of a second phase. The Li_xFePO_4 system is an example where the *kinetic* transformation path between $LiFePO_4$ and $FePO_4$ is fundamentally different from the path deduced from its *equilibrium* phase diagram.

5.1 Background

In the considerable volume of literature on the subject, the lithiation mechanism in (Li)$FePO_4$ is conventionally described and interpreted as a two-phase growth process[3,33,61,68,73,140,141] involving the coexistence of both phases ($LiFePO_4$ and $FePO_4$), initiated by a nucleation event. Several of these models are discussed in detail in section **1.4**. According to classical nucleation theory, upon lithiation of $FePO_4$ the inserted Li will pool together forming clusters, which only grow once a critical size is reached. The critical size, below which the new phase dissolves again, exists because the driving force for transformation scales with volume, and the interfacial energy which hinders the transformation scales with area. These concepts lead to the well known expressions for the critical radius (r^*) and critical nucleation barrier (ΔG_{r^*}), $r^* = \frac{2\gamma \cdot v}{|\phi| - \Delta g_s}$ and $\Delta G_{r^*} = \frac{16\pi \cdot \gamma^3 \cdot v^2}{3(|\phi| - \Delta g_s)^2}$,[19] where γ is the $LiFePO_4/FePO_4$ interfacial energy, v is the $LiFePO_4$ molar volume, ϕ is the applied underpotential, and Δg_s is the coherency strain energy. Using values determined from first-principles calculations of the interfacial energy[30] (γ = 0.96 J/m^2) and coherency strain energy[29] ($\Delta g_s \approx$ 3200 J/mole or 33 meV/Li for nucleating $LiFePO_4$ in "morphology 1" in [29]) available in the literature, r^* and ΔG_{r^*} can be determined as a function of the applied underpotential (and is plotted in **Figure 10**). For a critical nucleus to be smaller than 100 nm (i.e. for r^* = 50 nm), which is a typical size of a primary $LiFePO_4$ particle in a composite electrode, an underpotential in excess of 50 mV must be applied, and ΔG_{r^*} is at least several hundred thousand kT (at room

temperature) per cluster. This very large energy required to form the critical nucleus makes nucleation very unlikely. Even if one were to ignore the coherency strain energy altogether, and reduce the interfacial energy by a factor of two (e.g. to account for heterogeneous nucleation), ΔG_{r^*} for a 50 nm diameter nucleus exceeds 300,000 kT per cluster. Considering this very large ΔG_{r^*}, and the fact that the voltage hysteresis between charge and discharge in very slow discharging experiments (C/1000) approaches only ~ 20 mV,[79] the lithiation mechanism in $LiFePO_4$ is clearly inadequately described by classical nucleation and growth. An identical analysis performed here applies to the charging procedure.

5.2 Non–equilibrium Solid–Solution Free Energy Calculation

If nucleation does not proceed then the Li_xFePO_4 and $Li_{1-x}FePO_4$ solid solutions can be highly oversaturated. The high T behavior of Li_xFePO_4 (shown in the phase diagram in **Figure 6**) provides useful insight about the room temperature solid solution, specifically that there is only a small energetic difference between the phase separated state and the non-equilibrium solid solution. The single-phase state, which has low configurational entropy and becomes thermodynamically stable at relatively low temperature (~ 400 – 500 K), must then also have low mixing enthalpy and therefore low room-temperature free energy of mixing (assuming the heat capacity does not vary significantly with temperature). To quantitatively investigate the energetics of metastable solid solutions in Li_xFePO_4 as an alternative transformation path, the cluster expansion approach was used

combined with *ab initio* density functional theory calculations.[12] The cluster expansion allows determination of the energy of any Li/vacancy and Fe^{2+}/Fe^{3+} configuration in the system, and was parametrized from the calculated energies of 245 different Li/vacancy and electron/hole configurations in Li_xFePO_4 ($0 \leq x \leq 1$) shown in **Figure 28a**. These same formation energies were used previously as input to Monte Carlo simulations to accurately reproduce the Li_xFePO_4 phase diagram.[16] As shown in **Figure 28a**, no Li_xFePO_4 states with $0 < x_{Li} < 1$ have negative formation energies, in agreement with low temperature phase separation.

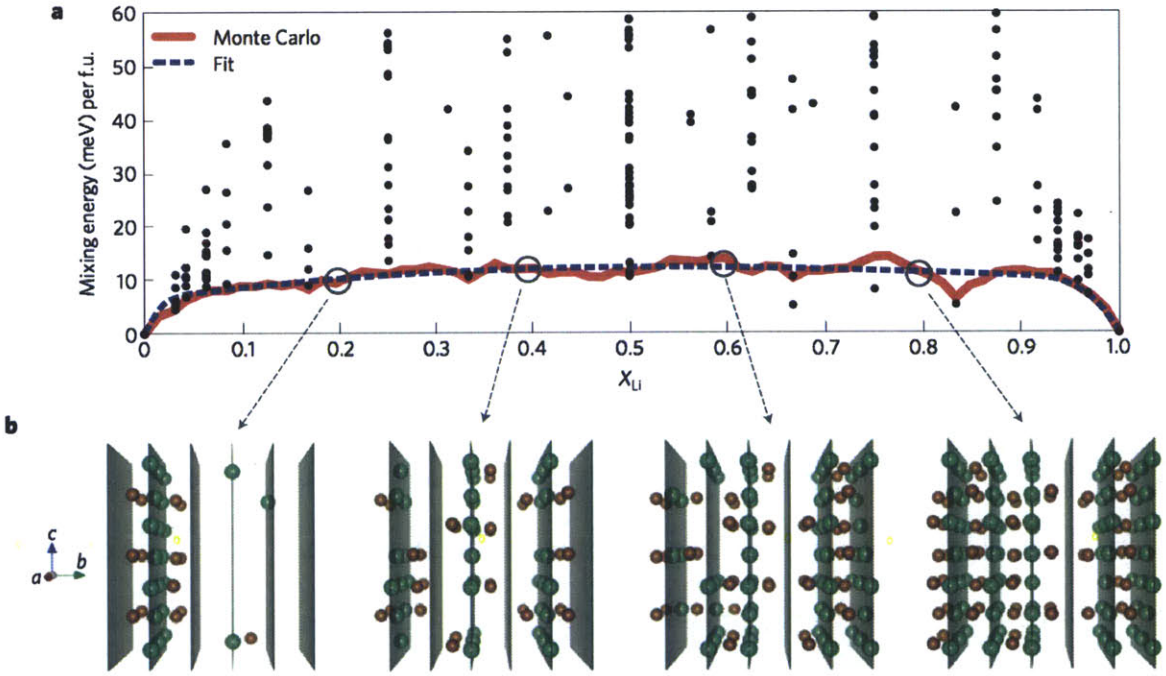

Figure 28: Free energy and atomic configurations along the single-phase $LiFePO_4$ transformation path. (a) Zero-temperature mixing energies (black circles) calculated from first-principles of 245 different Li /vacancy and electron/hole configurations in Li_xFePO_4 ($0 \leq x \leq 1$) show the existence of several low formation energy structures. The room temperature non-equilibrium *free* energy curve determined by canonical Monte Carlo simulations (solid red) using small simulation cells (2x3x3 unit cells), as well as the least squares cubic spline fit of the Monte Carlo data (dashed blue) both plateau at ~ 15 meV/f.u. within ~ $0.05 < x_{Li} < 0.9$. (b) Snapshots of Li (green atoms) and Fe^{2+} (brown atoms) configurations in room temperature Monte Carlo simulations at x_{Li} = 0.2, 0.4, 0.6, 0.8 show the succession of single-phase states with some local ordering. Adjacent (010) planes containing Li/vacancy are shown in green.

However, at several compositions between $x_{Li} = 0$ and $x_{Li} = 1$ the formation energies are very low and well below kT at room temperature: for instance 10.6 meV per formula unit at $x_{Li} = 0.333$, 5.2 meV per formula unit at $x_{Li} = 0.833$, and 5.1 meV per formula unit at $x_{Li} = 0.667$. Of the 245 formation energies shown in **Figure 28a**, 96 are below kT. This suggests that with minimal energy added to the system an insertion path that traverses through intermediate Li_xFePO_4 structures is possible. The advantages of a single-phase transformation path are significant: not only is the transformation facile, but lithiation of the particles is more homogeneous than in the two-phase model which reduces stresses and possible mechanical degradation of the material, consistent with the excellent cycling behavior of $LiFePO_4$ electrodes.

To better quantify the free energy and voltage along a metastable transformation path, Monte Carlo simulations were performed with the $LiFePO_4$ cluster expansion[16] with appropriate constraints to avoid phase separation to obtain the free energy of non-equilibrium states. Specifically, small simulation cells (2x3x3 unit cells) were used for which the phase-separated state is penalized (as an interface would constitute too large a relative contribution to the energy) and non-equilibrium but low energy single-phase states can be captured. The room temperature free energy of these states is shown in red in **Figure 28a**, and a sample of the structures found in the Monte Carlo simulations is shown in **Figure 28b**. Several somewhat unexpected observations can be made from **Figure 28**. First, the free energy does *not* have the typical regular solution form with two minima separated by a maximum as is typically assumed in simplified models of

$LiFePO_4$, and second, the Li-states while disordered show considerable short range ordering. Specifically, as seen in **Figure 28b**, at all concentrations Li vacancies prefer to accumulate locally within sheets in the *ac* plane (shown in green in **Figure 28b**, (010) planes in Miller indices) when possible, leaving the remaining interspersed sheets partially occupied by Li. Local ordering of Li and Li-vacancies has been directly observed experimentally, lending validity to the free energy model shown in **Figure 28a**.[18,19] Overall, the Li ions are distributed equally among the 1D diffusion channels oriented along the [010] direction,[47] and since the Li insertion reaction is a topotactic process, these structures define a continuous lithiation path where all 1D diffusion channels, not just those at a two-phase interface, are simultaneously active in either lithium insertion or deinsertion.

5.3 Effect on Electrochemical Charging and Discharging

The applied overpotential required to access these states is reflected in the slope of the free energy curve, where ΔG is the excess free energy over the equilibrium two-phase free energy (derivation shown in **Introduction**):

$$\Delta\phi = -\Delta\mu_{Li} = -\left(\frac{\partial \Delta G}{\partial x_{Li}}\right)_T . \qquad (36)$$

Because the free energy curve in **Figure 28a** corresponds to a non-equilibrium path, there will be an inherent voltage hysteresis between charge and discharge regardless of rate as seen in slow charge/discharge experiments (discussed in more detail in **Chapter 6**).[79] Also, the free energy curve is nearly flat for the bulk of the

concentration range (~ 0.05 < x_{Li} < 0.9), which has remarkable consequences on the charging and discharging behavior: if the local concentration of Li within a particle is within this range, very little change in driving force (potential) is required to

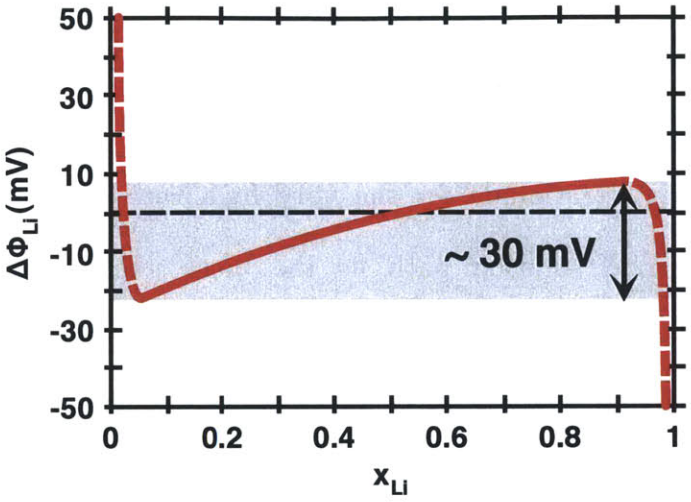

Figure 29: The single-particle voltage within ~ 0.05 < x_{Li} < 0.9 defined in *eqn. 34* and obtained from the least squares cubic spline fit of the Monte Carlo data shown in Figure 28a. The difference between the local maximum and minimum in this curve is the voltage hysteresis, indicating negligible voltage polarization between charge and discharge to good agreement with experimental work. Dashed portions of the curve are drawn to reflect the effect of configurational entropy on the potential in the dilute Li concentration and dilute vacancy limit.

drive either further lithiation or delithiation while avoiding phase separation. Hence, the voltage curve of this solid solution path will be remarkably flat. This is shown clearly in **Figure 29**, where the single-particle voltage defined in ***(38)*** (and obtained from the least-squares cubic spline fit of the Monte Carlo solid solution free energy shown in **Figure 28a**) is plotted in this specified concentration range. The calculated voltage hysteresis is very small, about 30 mV, which is consistent with Dreyer's observation that the voltage hysteresis in the zero current limit is small, about ~ 20 mV in $LiFePO_4$.[79]

The free energy curve in **Figure 28a** explains why (de)lithiation of (Li)$FePO_4$ is so facile. Taking discharge (lithiation) as an example, once a very small amount of Li is inserted in a particle (< 5%), lithiation will proceed as long as the potential is ~ 20 mV (the slope of the free energy curve) below the equilibrium potential. As no potential change is required to traverse the composition between $x \approx 0.05$ and $x \approx 0.9$, lithiation will proceed rapidly once a particle has some Li content ($>\approx 0.05$). Besides providing a rationale for the very high rate capability of $LiFePO_4$, the finding of the solid solution path as the most likely transformation path is consistent with several unexplained findings in the material. Several researchers have shown that solid solutions in Li_xFePO_4 created at high T and quenched to room temperature can persist for hours and even days without transforming to their equilibrium two-phase state.[60,120,142,143] Note that these results are surprising since the Li mobility in these materials is high, as demonstrated both from theoretical results[47] and from its high rate behavior.[4,38,139] The sluggish phase separation observed in these experiments is now well explained by considering the extremely flat solid solution free energy curve in **Figure 28a** indicating negligible thermodynamic driving force for demixing.

While these results indicate that Li_xFePO_4 may transform through a single-phase path, rather than by nucleation and growth of the second phase, the equilibrium state is undoubtedly two-phase. Hence, a partially (dis)charged electrode at rest will relax to the equilibrium two-phase state of lithiated and delithiated $LiFePO_4$ as shown in **Figure 30**. Whether the lithiated and delithiated

phases coexist within the same particle or as an assembly of particles, each either fully lithiated and delithiated, will vary as a function of particle size as described by Wagemaker *et al.*,[30] with larger particles stabilizing intraparticle two-phase coexistence (**Figure 30b**) and smaller particles favoring interparticle two-phase coexistence (**Figure 30a**) as observed by Delmas *et al.*[68]

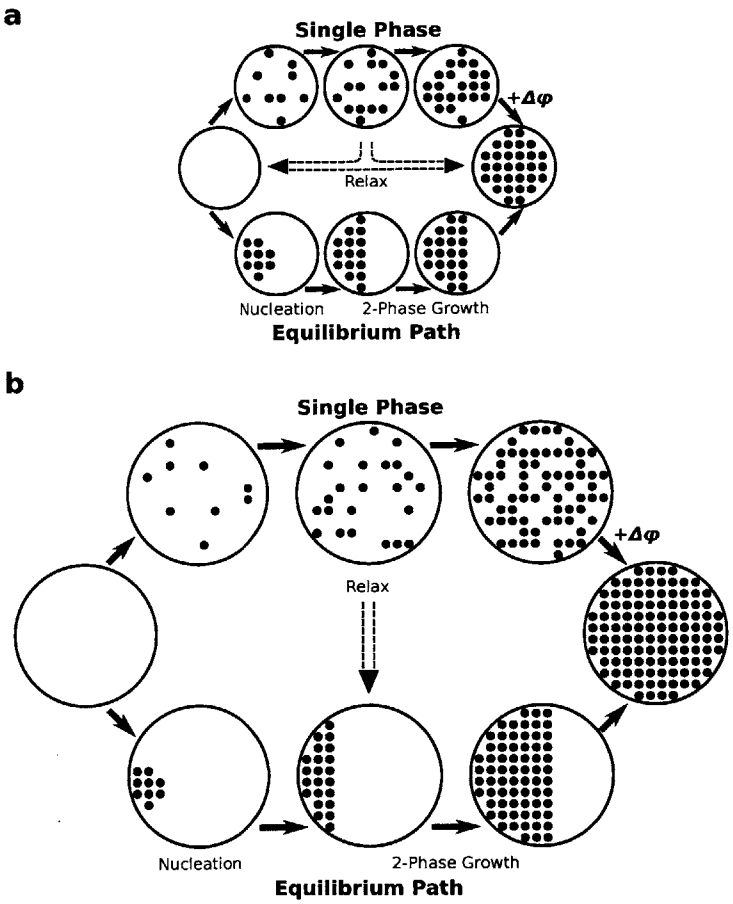

Figure 30: Schematic depiction of lithiation via an equilibrium two-phase path (bottom path) characterized by nucleation and growth compared to an alternative non-equilibrium single phase path (upper path) enabled by underpotential $\Delta\phi$ shown for a) small particles and b) larger particles. Once the underpotential is removed, the system relaxes to the equilibrium state.

In general, a non-equilibrium solid solution transformation will have substantially different kinetic behavior than an equilibrium solid-solution

mechanism, even though both proceed through a single phase. The source of this varied behavior is the shape of the single-particle Li chemical potential, which increases monotonically with Li content in the equilibrium scenario compared to the non-equilibrium case (**Figure 29**). In a hypothetical system where the solid-solution is thermodynamically stable at all Li concentrations, the driving force for further Li removal upon charging continually decreases given some fixed positive applied potential. Now consider charging a single LiFePO4 nanoparticle through the non-equilibrium solid solution path. After exceeding some critical overpotential (only ~ 10 mV as determined from first-principles calculations[90]) the driving force for additional litihium removal actually *increases*. If the applied potential is removed mid-charge, again the behavior differs between the equilibrium and non-equilibrium scenarios. In the former case, the Li will always homogenize within the particle, and in the latter case, the system will relax to the equilibrium phase-separated state (shown schematically in **Figure 30**), either two-phase coexistence within the same particle or inter-particle two-phase coexistence in a multi-particle system (described in detail in **Chapter 6**). With increasing particle size, the two-phase intra-particle state approaches the bulk limit, and is thus comparatively energetically favorable than in small particles, where the relative interfacial penalty is higher which overall favors inter-particle phase separation as depicted in **Figure 30**.

The metastable free energy curve and its associated single particle voltage profile derived from *ab-initio* computations also has significant consequences for the

(de)lithiation of a multi-particle assembly, as is the case in a real electrode (discussed in more detail in **Chapter 6**). The critical step for a particle to transform is to reach a certain concentration ($\approx$ 0.05 in discharge and $\approx$ 0.9 in charge). Once this concentration is reached (de)lithiation proceeds with only a small under(over)potential present. The particles which reach this solid solution regime first will insert (remove) Li as rapidly as their diffusion and surface transfer kinetics allow even at the expense of nearby particles which have not yet reached this limit. Particle size will play a role in this process, as smaller particles are saturated more rapidly and thus likely transform first. In the large particle limit, Li transport may become diffusion-limited, and phase-separation may occur within a particle. Whether the Li is obtained from the electrolyte or from extracting Li from neighboring particles depends on the relative rate at which Li from these two sources is available. Conversion of some $LiFePO_4$ to $FePO_4$ during discharge (lithiation) has actually been observed in in-situ XRD experiments.[144] Overall, this leads to a very inhomogeneous charge/discharge picture of the electrode where particles will appear either fully lithiated or fully delithiated as observed by Delmas *et al.*[68] Delayed and inhomogeneous transformation of $LiFePO_4/FePO_4$ have indeed been observed in multiple *in-situ* XRD experiments.[144]

5.4 Conclusions

In summary, despite its strong two-phase equilibrium character, the remarkable rate capability of $LiFePO_4$ can be explained by the existence of an

alternative single-phase transformation path available at very low overpotential, the availability of which obviates the need for nucleation and growth. By calculating the magnitude of the overpotential needed to enable the single-phase transformation path, it is determined that only minimal overpotential is required at room temperature. While $LiFePO_4$ is an example where the transformation path is fundamentally different from the equilibrium thermodynamic behavior, this result also opens up a more rational approach to the search for new electrode materials. Many potentially new Li-storage materials have strong first-order kinetics in their phase transformations and often display very poor kinetics.[145] This work shows that efforts to find new high energy-density materials with reasonable rate capability may have to focus on the potential non-equilibrium paths that are available to the system in a small range of overpotential, as they may be substantially faster than, and different from, the equilibrium path. Such solid-solution non-equilibrium paths can only exist if the phases are topotatically related and if the formation enthalpy of the states with intermediate lithium content is not too high.

Chapter 6: Implications and Future Work

6.1 Equilibrium in a Multi–Particle Assembly

An actual composite electrode is an assembly of many particles (~ 10^{10} – 10^{17}), no longer subject to the constraint that the Li concentration must remain fixed within each particle only that the overall Li concentration in the electrode is set. For an electrochemical cell to function, the active cathode material must be ionically and electronically wired to the counter-electrode, and in the conventional Li-ion battery architecture, active particles are simultaneously ionically and electronically wired to each other (through the electrolyte facilitating Li^+ exchange and through either carbon addition and/or particle–particle contact ensuring electronic connectivity). Li exchange between $LiFePO_4$ particles has been shown experimentally by Lee *et al.*,[146] by first constructing an electrode consisting of nano-$FePO_4$ and bulk $LiFePO_4$ particles and, after allowing the system to equilibrate, observing peak broadening in the x-ray diffraction (XRD) spectra consistent with the existence of nano-$LiFePO_4$. It is typically assumed that measurements of multi-particle systems reflect single-particle behavior, which may be a reasonable assumption for solid-solution systems but, as shown below, falls short in describing phase-separating systems.

The multiple particle equilibrium differs from the single-particle equilibrium due to the characteristic non-convexity of the single-particle free energy. The conditions for equilibrium in a multiple particle assembly (i.e. to minimize the

system free energy) require all particles to have identical μ_{Li} and to be stable with respect to Li concentration exchange fluctuations between particles. If the single-particle free energy is entirely convex, the corresponding μ_{Li} monotonically increases with x_{Li} as shown in **Figure 31a**, and thus for a given μ_{Li} there is a

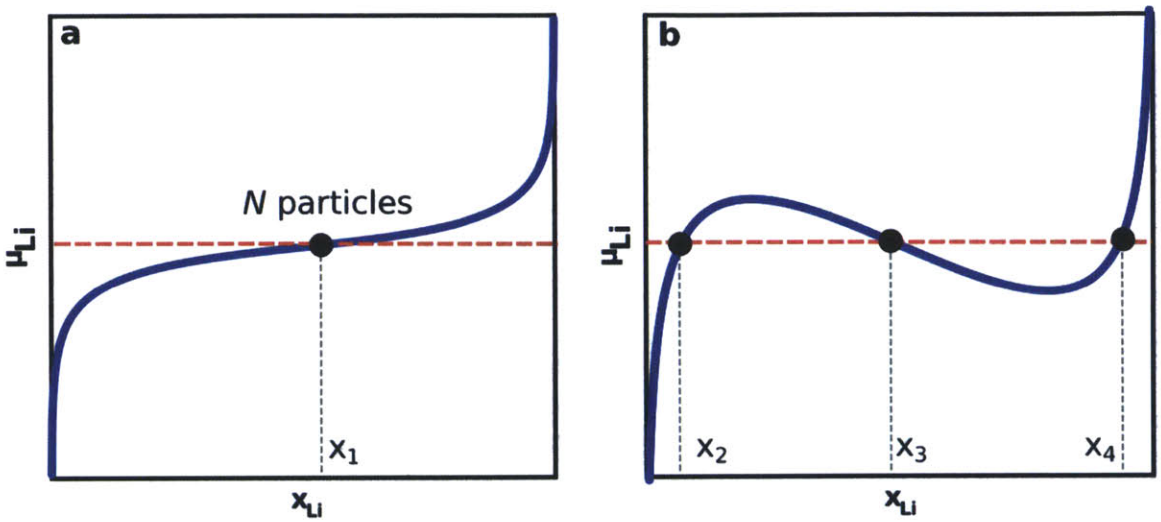

Figure 31: Schematic depictions of the equilibria defined at some fixed μ_{Li} (dashed red line) in a multi-particle system of *N* particles, each with either (a) a monotonically increasing single-particle Li chemical potential (μ_{Li}) or (b) a non-monotonically increasing single-particle Li chemical potential (μ_{Li}).

unique global minimum in the system free energy corresponding to all *N* particles sharing the identical Li concentration (x_1). Due to the non-convexity in the single-particle free energy (highlighted in both **Figure 7b** and **Figure 28a**), however, the $LiFePO_4$ single-particle μ_{Li} does not increase monotonically with x_{Li}, and there are several different x_{Li} (namely x_2, x_3, and x_4) that share the same μ_{Li} (shown in **Figure 31b**), meaning that there are multiple configurations that satisfy the first equilibrium criterion (identical μ_{Li} in each particle). Dreyer *et al.* have enumerated through all possible equilibria, showing that for a given global Li concentration, there are stable equilibria each corresponding to a fraction of the particles Li-rich

and the remaining fraction Li-poor.[79] Physically, this can be rationalized by considering that the possibility of free Li-exchange amongst all particles allows any energy penalty associated with creating a two-phase interface to be avoided. Coexistence of fully intercalated and deintercalated $LiFePO_4$ particles has indeed been confirmed in partially electrochemically lithiated samples allowed to relax and then characterized using both *ex–situ* x-ray diffraction (XRD)[68] and advanced transmission electron microscopy (TEM) methods.[78] It is of interest to point out that the aforementioned *ex-situ* observations of fully lithiated and delithiated particles can be fully rationalized by the system thermodynamics without having to invoke any specific kinetic mechanism of lithiation.

The consequences of having multiple local minima in the free energy can be illustrated with a demonstrative example. Consider the simplified case illustrated

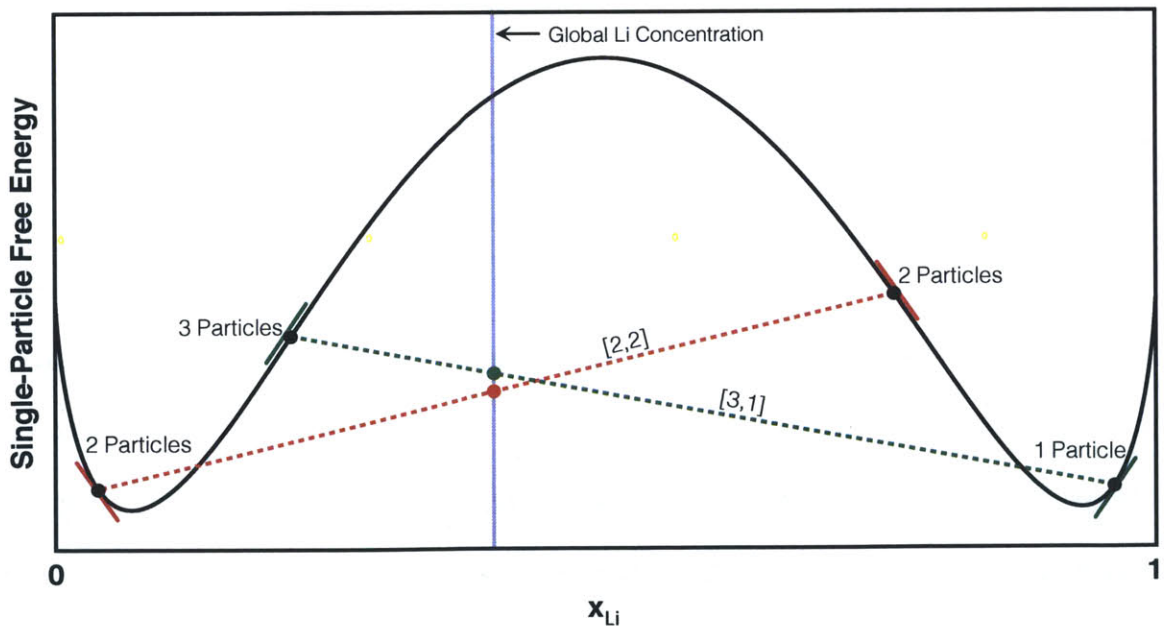

Figure 32: Illustration of the existence of two possible local equilibria (labeled [2,2] in green and [3,1] in red) in a 4-particle system with global concentration x_{Li} = 0.4, where each particle has an identical non-convex single-particle free energy (drawn in black). The Li chemical potential (μ_{Li}) of each equilibrium is represented by the instantaneous slope of the single-particle free energy (i.e. slope of solid green or red tangent).

in **Figure 32**, a system containing 4 identical Li_xFePO_4 particles with a global concentration falling within the single-particle miscibility gap (x_{Li} = 0.4). Highlighted and overlaid over the schematic single-particle free energy in **Figure 32** are two configurations corresponding to two local minima, one consisting of 2 lithium poor and 2 lithium rich particles (labeled [2,2] in red) and another consisting of 3 lithium poor and 1 lithium rich particles (labeled [3,1] in green). The molar free energy of the system is graphically represented at x_{Li} = 0.4 by the red and green points, the molar free energies of the [2,2] and [3,1] configurations, respectively. Although there is only a small difference in the free energy between both equilibria, there is a notable difference in μ_{Li} (and consequently the open-circuit voltage), represented by the slope of the tangent of the free energy, drawn in red and green for the [2,2] and [3,1] configurations, respectively. In Li_xFePO_4, the open-circuit voltage of different equilibria can vary by as much as ~ 20 to 30 mV, while maintaining near identical free energy (~ 5 – 10 meV/f.u. or 1 – 2 kj/mol) according to **Figure 28a**. As more particles are introduced to the system, the number of such equilibria also increases, and by virtue of having many stable equilibrium configurations, the equilibrium that a system eventually evolves toward is *path-dependent*, which is reflected in OCV measurements with varying charging and discharging histories converging to different values (even after long relaxation times).[79,80,147] This feature of the free energy landscape of $LiFePO_4$ effectively rationalizes how the Li_xFePO_4 system well known for rapid lithiation kinetics

appears to require exorbitant times to equilibrate as entire particles must transform as the system evolves toward a local free-energy minimum.[79]

In a potential-controlled system like an electrochemical cell, the existence of a non-monotonic single-particle voltage curve and interaction between active particles are chiefly responsible for the characteristic voltage plateau observed in slow discharging and charging experiments.[79] The subset of equilibria traversed during low-rate charging is shown qualitatively in **Figure 33**. To charge an assembly of $LiFePO_4$ particles quasi-statically, an small overpotential (the difference between ϕ_{app} and the single-particle potential in **Figure 33**) is continually applied to drive Li out of $LiFePO_4$. Initially the driving force for charging, which is the difference between the applied potential and the single-particle potential, decreases with respect to further Li removal from a single particle, simply because the single-particle potential initially increases with capacity. Thus for charging several particles, this ensures that Li is extracted equally from all particles within this regime, as shown schematically in **Figure 33a** and **Figure 33b**.

Once the potential is increased such that each particle reaches the critical concentration x_c (**Figure 33c**), there is an apparent concentration instability– any fluctuation of Li out of an individual particle begets additional accelerated Li removal, as the driving force for charging increases in the already delithiating particle (described schematically with arrows of increasing magnitude in **Figure 33c** delineating the accelerated charge of Particle 1). Whether the Li is removed to

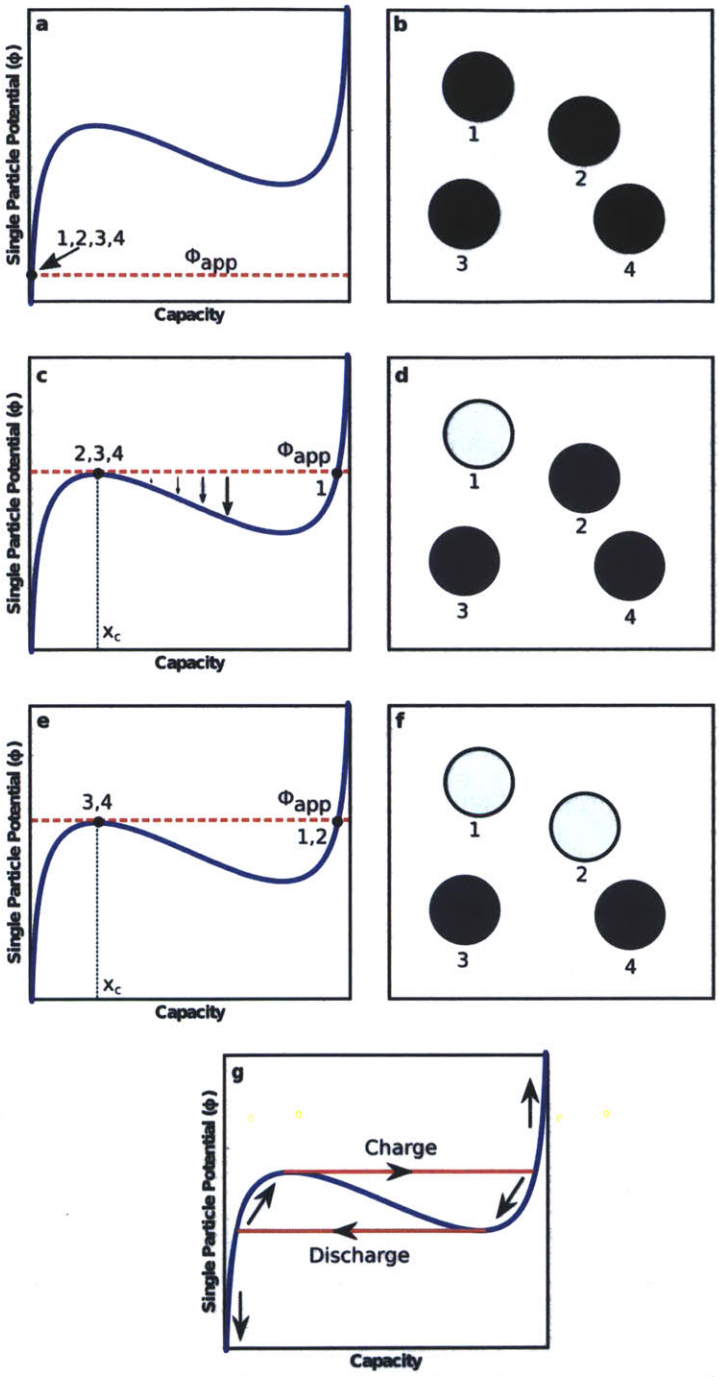

Figure 33: Schematic illustration of slow (quasi-static) charging, with some slowly increasing applied potential Φ_{app} (dashed red line), of a 4-particle Li_xFePO_4 system where each particle has the single-particle potential (drawn in blue) described in (a), (c), and (e). Qualitative descriptions of each particle's concentration during the charging process are described schematically (b), (d), and (f). The total system behavior is highlighted in (g) which shows the system voltage curve with characteristic built-in hysteresis in the zero-current limit.

the counter-electrode or is incorporated into neighboring particles (i.e. Particles 2,3,

or 4) will depend on the electrode kinetics. At this same potential, the process repeats itself and the remaining lithiated particles charge sequentially, as described in **Figure 33e** and **Figure 33f**, which accounts for the well-observed voltage plateau in experiments shown schematically in **Figure 33g**. Due to the shape of the single-particle voltage curve, the voltage plateau for the multi-particle system is inherently higher on charge than on discharge, which explains the non-vanishing ~20 mV hysteresis in the zero-current limit (at C/1000) in the Li_xFePO_4 voltage profile demonstrated by Dreyer *et al.*[79]

The particle size and morphology distribution of the active particles within the electrode means there is also a distribution amongst the active particles' phase transition voltages due to variation in the surface energy contributions to each single-particle free energy. Van der Ven *et al.* studied the effect of particle size distribution on the multi-particle Li_xFePO_4 OCV and showed that the larger the surface energy difference between a lithiated and delithiated active particle, and the wider the particle size distribution (within the nano-particle regime where surface-energy effects contribute the greatest), the more sloping the open-circuit voltage curve becomes.[148]

Across length scales, from bulk, to single-particle, to an assembly of many particles, the additional interactions and physical changes to the system continually modify the Li_xFePO_4 free energy and voltage profile. *Therefore, the free energy and voltage of a multiple-particle $LiFePO_4$ system appears qualitatively differently than that of a single particle, which in itself has varying features compared to the bulk*

system. Since the vast majority of electroanalytical experiments are performed on electrodes consisting of many particles, the behavior of bulk and single-particle Li_xFePO_4 is shrouded by interactions between particles, which can lead to possible mischaracterization of the properties of individual $LiFePO_4$ particles, an oft-recurring theme in the $LiFePO_4$ literature. For instance, the appearance of a voltage plateau in slow galvanostatic charging and discharging experiments has been historically interpreted as all $LiFePO_4$ particles simultaneously undergoing a phase transformation with two-phase coexistence, but as revealed through analysis of the multi-particle equilibrium, the plateau in the open circuit voltage really signifies coexistence of nearly fully lithiated and delithiated active particles, and no statement about *how* particles individually transform can be made from these experiments. Alternatively, sloping voltage curves are conventionally interpreted as proof of single-phase existence and are often used in the literature to identify the solubility limits; however, as demonstrated by Van der Ven *et al.*, a sloping voltage curve can arise from a wide size distribution of nano-particles each undergoing a phase transformation. Overall, a thorough examination of the Li_xFePO_4 equilibrium at the relevant length scales (bulk, single-particle, multi-particle) reveals the apparent non-triviality of the system thermodynamics, providing the basis for the unique (de)lithiation kinetics observed in this material. One may have to accept that simple charge/discharge experiments on composite electrodes reveal very little about the delithiation curve of single particles.

6.2 Electrode-Scale (de)lithiation

An implicit assumption in the traditional analysis of experimentally obtained charging and discharging data involves the single-particle behavior mirroring the electrode-scale behavior. This assumption is what enables materials properties such as Li diffusivity and insights regarding the single-particle lithiation mechanism to be extracted from conventional electrochemical experiments. The Li_xFePO_4 multi-particle equilibrium, however, exhibits a large degree of inhomogeneity at any intermediate state of charge with some particles fully lithiated and the remaining fraction fully delithiated. In the quasi-static limit, an assembly of $LiFePO_4$ particles will charge sequentially[79] rather than in parallel as assumed in conventional electrode-scale models as a consequence of the unusual shape of the single-particle potential.

Now consider the opposite scenario, charging an assembly of $LiFePO_4$ particles by applying a very large constant overpotential (i.e. $\Delta\phi >> 30$ mV, well in excess of the zero-current voltage gap[79]) and temporarily assume there are no rate limitations stemming from either Li^+ salt depletion in the electrolyte or poor electronic transport from the current collector. In this hypothetical limit, the large applied potential is far greater than the scale of the features of the single-particle potential curve, meaning that the driving force (i.e. the difference between the applied potential and single-particle potential) for Li removal from any and every $LiFePO_4$ particle in the system is roughly the same as illustrated in **Figure 34a** compared to **Figure 34b**. Consequently, all particles charge simultaneously and in

parallel in the large overpotential limit idealized scenario. Therefore, at intermediate charging rates, the multi-particle behavior is much more complex and lies somewhere in the middle, with some combination of particles charging in parallel and in series.

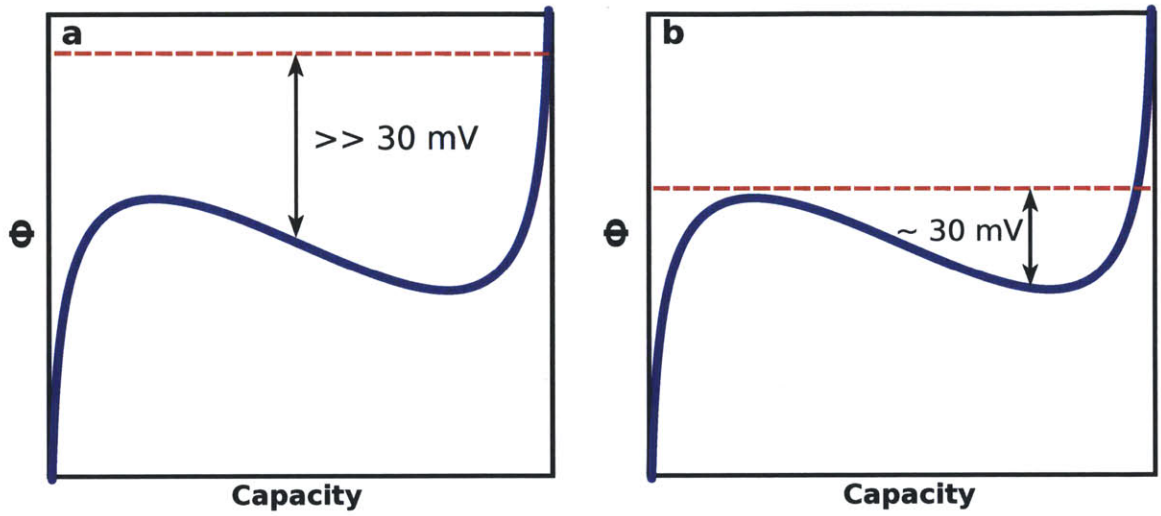

Figure 34: Schematic representation of charging at high (a) and low (b) rate. The driving force for Li removal is represented by the difference between the applied potential Φ_{app} (dashed red) and the single-particle potential (solid blue).

Intuitively, it is much more efficient to charge all particles within an electrode in parallel rather than one-by-one. To draw a fixed current, for instance, charging in sequence requires each particle, locally charged at an exceedingly high rate, to sustain all of the power in the electrode rather than the converse scenario where all particles, equally distributing the entire current, are charged simultaneously each at a much lower relative rate. The notion of more effective power distribution at higher rates is a curious outcome, but one that is predicated upon rapid electrode-scale kinetics and uniform distribution of the potential across the cell. Practically, this implies that cell construction and architecture play critical roles to access

$LiFePO_4$'s full rate capability, and indeed, noticeable empirical improvements in cell rate performance have been achieved through electrode-level modifications: most notably through adding carbon,[37] synthesizing $LiFePO_4$ nano-particles with Li conducting amorphous coating,[4] varying the electrode thickness,[149] and diluting the active mass (with inactive material) of the electrode.[39]

6.2.1 Carbon Coating

Ravet *et al.* first observed the benefits of carbon-coating,[37] observing peak sharpening in cyclic voltammetry data and overall enhancement of cycling kinetics and stability. Incorporating carbon coatings has now become one of the most common strategies to improve the rate performance of not only $LiFePO_4$ electrodes, but other chemistries as well.[150] An elaborate survey of the use of carbon-coatings and other sources of carbon addition in $LiFePO_4$ electrodes has been assembled and published elsewhere, with significant detail paid to different synthesis methods and the general impact on experimental performance.[151] Overall, any improvement in the charge and discharge kinetics as a result of carbon addition cannot come from improving the bulk transport within the active material, specifically the bulk electronic conductivity. Rather, carbon addition primarily improves the electronic contact between active particles and improves electronic connectivity to the current collector which makes for more effective current distribution at intermediate rate. Alternatively, another area of kinetic improvement may come indirectly from the simultaneous restriction of active particle growth to the nano-scale with carbon-

coating formation in the synthesis process arising from the decomposition of organic precursors.[152] In fact, this may be the most compelling explanation as pointed out by Gaberscek *et al.* in a survey of published electrochemical data comparing the performance of carbon-coated $LiFePO_4$ to non-carbon-coated $LiFePO_4$ which concluded that improved rate performance is highly correlated with smaller active particle size rather than the presence of carbon.[153] Also, the presence of a collection of $LiFePO_4$ nanoparticles embedded in a carbon matrix allows for additional mechanical stability, better accommodating the sizeable active particle volume change upon Li insertion and deinsertion.[152]

6.2.2 Ionically Conductive Coatings

In addition to synthesizing nano-$LiFePO_4$ particles with carbon-coating, the best rate performance achieved to date in a lab setting, accessing nearly two thirds of the theoretical capacity at ~ 200 C and about 1/3rd of the capacity at ~ 400 C, has been through charging and discharging $LiFePO_4$ nanoparticles (~ 50 nm) synthesized with poorly crystallized rapid ionic conducting glass-coatings.[4] A novel synthesis technique, intentionally steering the off-stoichiometry toward $LiFe_{0.9}P_{0.95}O_{4-\delta}$, results in the formation of an amorphous coating surrounding the active $LiFePO_4$ particles with a self-limited thickness comprising of most likely a combination of Li_3PO_4 and $Li_4P_2O_7$, as predicted by the first-principles determined phase diagram.[23] The purported mechanism of improved kinetics here is not only enhanced Li mobility within the glassy layer but also potentially improved surface

Li incorporation kinetics between the electrolyte and surface coating. Adams *et al.*, using a bond-valence force field method, calculated a 3 order of magnitude increase in the surface ionic conductivity with a $Li_4P_2O_7$ particle coating, which supports the former assertion.[154] As with carbon-coated particles, the benefit of ionically conductive glassy coatings does not lie in assisting the Li intercalation kinetics *within* the active particle itself, but rather in improving the kinetics of transporting Li *to* the active particle.

6.2.3 Electrode Thickness and Dilution

Along the same lines of altering the electrode architecture to improve overall electrode kinetics, the rate performance can be enhanced by varying the electrode thickness and also diluting the concentration of active mass (with inactive material). Gaberscek *et al.* specifically studied the impact of optimizing the electrode "wiring," that is the ionic and electronic connectivity between particles and also to the electron and Li^+ source (i.e. current collector and electrolyte, respectively). In particular, they systematically monitored the variation of reversible capacity and polarization as a function of both electrode mass and charge/discharge rate, while keeping the remaining parameters (i.e. particle size, porosity, etc.) as close to constant as possible. Interestingly, at low currents the kinetics are limited by the active particles themselves, supported by the non-linear behavior of current with polarization (roughly resembling Butler-Volmer behavior), and at higher rates, the rate limitation comes purely from the electrode resistance,

corroborated by the linear increase of the polarization with current. At low rates (ranging from C/20 to 1C), the reversible capacity remains nearly unchanged with electrode thickness, but at higher rates (ranging from 1C to 20C) there is a sharp decline in the reversible capacity with increasing thickness. This supports the notion that at higher rates, the rate-limiting step is no longer intercalation of Li within the active particles, but the passage of electrons and Li^+ through the electrode. The result is somewhat surprising, considering that much of the $LiFePO_4$ literature assumes that Li insertion into Li_xFePO_4 is inherently slow (either due to poor bulk electronic or ionic conductivity) and therefore is likely rate-limiting in all charging and discharging conditions (both low and high rate), certainly in comparison to Li^+ transport through the electrolyte and electron transport through carbon. Liu *et al.* were able to visualize the distribution of $LiFePO_4$ and $FePO_4$ spatially along directions parallel and perpendicular to the current collector within a thick electrode (40 mm by 45 mm) at intermediate states of charge using synchotron X-ray microdiffraction.[155] After charging to 50% state of charge at low rate (~ 0.11 C) the $FePO_4$ distribution is nearly uniform throughout the cell, and after charging at much higher rate (~ 18 C) the $FePO_4$ distribution is much more inhomogeneous, specifically in the direction perpendicular to the current collector. Again, this finding suggests that at high rates, the transport of either Li^+ or e^- to the active material is rate-limiting and points to unconventional multi-particle behavior that manifests itself by varying the electrode dimensions.

Another method to improve the electrode-scale kinetics involves diluting the active mass with electrochemically inactive material. For example, Johns *et al.* constructed composite electrodes with commercially synthesized $LiFePO_4$, acetylene black, TiO_2 (anatase), and PVDF binder with varying concentrations. Specifically, keeping the overall concentration of acetylene black and binder constant, sample electrodes were assembled with decreasing concentrations of $LiFePO_4$ offset by increasing concentrations of TiO_2, which is electrochemically inactive in the typical $LiFePO_4$ cycling window. Samples with increased dilution (i.e. more $LiFePO_4$ substituted with TiO_2) exhibit far superior rate-performance especially at high rates, which in itself illustrates that the source of rate limitation in this regime is the electrode construction rather than Li intercalation into active single particles.[39] By diluting the electrode and constructing a simple yet powerful model of Li diffusion across the electrode, Johns *et al.* identified that at high charging and discharging rates, the concentration of Li salt in the electrolyte is locally depleted which limits the accessible capacity but is mitigated by reducing the overall content of $LiFePO_4$ within the electrode.

6.3 Electrode-Scale Inhomogeneity

Beyond reducing the particle size to nano-dimensions, all of the major developments to enhance the high-rate performance of $LiFePO_4$ electrodes have historically been the result of electrode-scale improvements. Moreover, these apparently different strategies (carbon coating, ionically conducting coatings,

modified electrode thickness, and electrode dilution) hinge on the same principle. In effect, they all seek to optimize the "electrode wiring" and homogenize the distribution of the applied electrochemical potential across the cell, which is required to access the inherent high rate capability of $LiFePO_4$. Although the aforementioned modifications are performed at the electrode-scale, they facilitate the entire assembly of active particles to charge and discharge differently as a whole, a phenomenon that is unique to phase-transformation electrode materials (due to the characteristic non-monotone single-particle potential). Consider a "less-than-ideal" wired electrode, where the electrochemical potential is inhomogeneously distributed due to poor and varying ionic electronic connectivity throughout the cell. Although this cell construction will result in overall poorer performance for any given electrode material (two-phase or otherwise), the deleterious effects are exacerbated in $LiFePO_4$ electrodes. Those particles that are best "wired" experience the greatest electrochemical driving force for transformation. Therefore, they first undergo complete phase transformation and sustain the entire current demands of the cell, overall resulting in an inefficient sequential particle-by-particle charging/discharging scheme, in this case even at finite current conditions. In a worst-case scenario, the local Li availability (on discharge for instance) in the electrolyte is depleted or electronic connection to the counter-electrode is so poor such that the most kinetically expedient method of intercalation comes via inter-particle transport (implying simultaneous charging and discharging within the same cell).

The electrode-scale inhomogeneity in $LiFePO_4$ electrodes during charging and discharging is no more evident than in the data obtained from *in-situ* experiments. In recent years, the experimental capability to simultaneously monitor the presence of the transforming phase (i.e. emergence of $LiFePO_4$ during discharge or $FePO_4$ during charge) through XRD during active cycling has revealed an apparent irreconcilable finding– the XRD and electrochemical data do not align in time. This has been reported by a number of researchers,[80,84,85,144,156] each observing a delay between the XRD and electrochemical data. Upon the first discharge half-cycle, the collected XRD spectra remain nearly unchanged, yet according to the voltage curve electrochemical capacity is continually accessed, and only after the cell is allowed to rest does the XRD spectrum correspond to that of $LiFePO_4$. The discrepancy between the XRD and electrochemical data can be rationalized under the lens of inhomogeneous multi-particle kinetics. The voltage measurements are collected at the electrode scale, and by virtue of the experimental setup, the XRD measurement is more local. Due to some spatial pressure variation as a result of the cell construction (specifically, pressure is relieved near the X-ray window) the XRD measurement is biased, and the $FePO_4$ in that region transforms last possibly due to poorer ionic or electronic wiring (possibly from pressure relief).[85] Moreover, Ouvrard *et al.* specifically note that the cell-level inhomogeneity is influenced by other parameters of the cell construction and also the cycling parameters themselves.[85]

A survey through the literature reveals that different $LiFePO_4$ electrodes (i.e. electrodes with the active mass roughly made of the same material) are capable of giving poor to excellent rate performance. Reducing the particle size to the nano-scale to improve Li transport within active particles is clearly necessary, but the remaining improvements in $LiFePO_4$ rate performance have come from electrode-scale modifications or materials modifications which improve the wiring (e.g. carbon coating and ionically conductive glass coating), as discussed earlier. This finding highlights the importance of optimizing the multi-particle kinetics to access the inherent high rate-capability of the active material. The reason the multi-particle kinetics can dictate the overall rate performance stems from the unusual shape of the single-particle potential (the thermodynamics and kinetics of which are discussed in detail in **Chapter 1** and **Chapter 5**, respectively). Consequently, particles transform sequentially in the slow charging/discharging limit, and given no electrode-scale kinetic constraints, transform in parallel at high-rates, the ideal scenario. This highlights the importance of mitigating electrode-scale inhomogeneity, which if unaddressed ensures ineffectual rate performance due to sequentially charging particles and even worse, possible simultaneous charging and discharging of particles arising from inter-particle Li transport. The key to optimizing the electrode-scale kinetics involves electronically and ionically "wiring" each particle as close to identically as possible, meaning that transport of both Li^+ and e^- is equally unimpeded to each particle. Experimentally, this has been achieved to great success through a combination of carbon addition (through coating

active particles and adding carbon in electrode assembly), coating active particles with Li^+ conducting glasses, varying the electrode thickness, and/or diluting the proportion of active material within the electrode. An effective understanding of the governing mechanism by which electrode-scale modifications enable fast charging and discharging behavior now motivates future work in improving and optimizing electrode assembly and architecture rather than focusing solely on active material synthesis.

Conclusions

In this thesis, we have used first-principles calculations to characterize and understand the intercalation of Li in phospho-olivines, focusing on three specific topics germane to the overall improvement of Li–ion battery performance: the redox voltages and phase behavior of mixed olivines, the particle size dependence of the ionic diffusivity in 1D conductors due to point defect obstacles, and the kinetics of non-equilibrium Li insertion in $LiFePO_4$.

By making minor modifications to an already proven accurate lattice cluster expansion[16] of the Li_xFePO_4 Hamiltonian (parametrized from first-principles calculations), specifically by shifting the electronic point term at random Fe sites to approximate Mn occupation, the experimentally observed phase behavior and electrochemical properties of mixed olivines can be well understood. The formation of an intermediate single-phase region centered at $Li_x(Fe_{1-y}Mn_y)PO_4$ (where $0 < x < 1$ and $0 < y < 1$) and the lowered transition temperature to form solid solution are the result of the dilution of phase-separating interactions. The attractive interaction between Mn^{2+} and Li^+ is diluted by Fe^{3+} in the solid solution and vice versa. Similarly, the observed changes in plateau voltages can be explained by the change in energy of the intermediate solid solution. Due to the unfavorable Li^+ coordination, the Fe^{3+} and Mn^{2+} states in the solid solution have higher energy than in their pure $FePO_4$ or $LiMnPO_4$ phases leading to higher and lower plateau voltages for Fe^{3+}/Fe^{2+} and Mn^{3+}/Mn^{2+} respectively. Although this model provides

insight into the phase behavior and electrochemical properties of the $Li(FeMn)PO_4$ system, the major findings can be equally applied to other mixed olivines and even generalized to describing the effect of random–site substitution in generic phase-separating systems.

Next, the origin of inherently poor rate performance associated with large compared to nano-sized active $LiFePO_4$ particles is identified by modeling the particle size dependence of the ionic diffusivity, specifically the effect of the presence of Li–Fe anti-site defects which obstruct inherently fast 1D Li diffusion in the defect-free crystal. With just small concentrations of point defects, nearly the entirety of the Li capacity of micron-sized particles becomes impeded, and the directional diffusivities as estimated from first-principles calculations now depend on the rate of defect circumvention. Consequently, the fast 1D ionic diffusivity oriented along the [010] direction decreases with increasing defect concentration, and the diffusivity in the orthogonal directions increases, reducing the diffusion anisotropy to good agreement with experimental observations.

Finally, the exceptionally rapid charge and discharge performance observed in nano-$LiFePO_4$ particles despite having to undergo Li phase separation can now be effectively rationalized by identifying the existence of a non-equilibrium but kinetically expedient transformation pathway available with little driving force. Based on Monte Carlo simulations informed by first-principles calculations, an overpotential of only ~ 20 mV is required to access a single-phase transformation path through the non-equilibrium Li_xFePO_4 solid solution. While $LiFePO_4$ is an

example where the transformation path is fundamentally different from the equilibrium thermodynamic behavior, this result also opens up a more rational approach to the search for new electrode materials. Many potentially new Li-storage materials have strong first-order kinetics in their phase transformations and often display very poor kinetics.[145] This work shows that efforts to find new high energy-density materials with reasonable rate capability may have to focus on the potential non-equilibrium paths that are available to the system in a small range of overpotential, as they may be substantially faster than, and different from, the equilibrium path. Such solid-solution non-equilibrium paths can only exist if the phases are topotatically related and if the formation enthalpy of the states with intermediate lithium content is not too high.

References

1. US EPA, C. C. D. U.S. Greenhouse Gas Inventory Report. *epa.gov* at <http://www.epa.gov/climatechange/ghgemissions/usinventoryreport.html>
2. AutoblogGreen -- We Obsessively Cover the Green Scene. *green.autoblog.com* at <http://green.autoblog.com/>
3. Padhi, A., Nanjundaswamy, K. & Goodenough, J. Phospho-olivines as positive-electrode materials for rechargeable lithium batteries. *J Electrochem Soc* **144**, 1188–1194 (1997).
4. Kang, B. & Ceder, G. Battery materials for ultrafast charging and discharging. *Nature* **458**, 190–193 (2009).
5. Padhi, A., Nanjundaswamy, K., Masquelier, C., Okada, S. & Goodenough, J. Effect of structure on the Fe^{3+}/Fe^{2+} redox couple in iron phosphates. *J Electrochem Soc* **144**, 1609–1613 (1997).
6. Iyer, R., Delacourt, C., Masquelier, C., Tarascon, J. & Navrotsky, A. Energetics of $LiFePO_4$ and polymorphs of its delithiated form, $FePO_4$. *Electrochem Solid St* **9**, A46–A48 (2006).
7. Yang, S., Song, Y., Zavalij, P. & Whittingham, M. Reactivity, stability and electrochemical behavior of lithium iron phosphates. *Electrochem Commun* **4**, 239–244 (2002).
8. Arroyo y de Dompablo, M. E. *et al.* Gaining Insights into the Energetics of $FePO_4$ Polymorphs. *Chem Mater* **22**, 994–1001 (2010).
9. Li, G., Azuma, H. & Tohda, M. $LiMnPO_4$ as the cathode for lithium batteries. *Electrochem Solid St* **5**, A135–A137 (2002).
10. Amine, K., Yasuda, H. & Yamachi, M. Olivine $LiCoPO_4$ as 4.8 V electrode material for lithium batteries. *Electrochem Solid St* **3**, 178–179 (2000).
11. Wolfenstine, J. & Allen, J. Ni^{3+}/Ni^{2+} redox potential in $LiNiPO_4$. *J Power Sources* **142**, 389–390 (2005).
12. Zhou, F., Cococcioni, M., Kang, K. & Ceder, G. The Li intercalation potential of $LiMPO_4$ and $LiMSiO_4$ olivines with M = Fe, Mn, Co, Ni. *Electrochem Commun* **6**, 1144–1148 (2004).
13. Chevrier, V., Ong, S., Armiento, R., Chan, M. & Ceder, G. Hybrid density functional calculations of redox potentials and formation energies of transition metal compounds. *Phys Rev B* **82**, (2010).
14. Thackeray, M. M., Johnson, P. J., de Picciotto, L. A., Bruce, P. G. & Goodenough, J. B. Electrochemical extraction of lithium from $LiMn_2O_4$. *Mater Res Bull* **19**, 179–187 (1984).
15. Ménétrier, M., Saadoune, I., Levasseur, S. & Delmas, C. The insulator-metal transition upon lithium deintercalation from $LiCoO_2$: electronic properties and ^7Li NMR study. *J Mater Chem* **9**, 1135–1140 (1999).
16. Zhou, F., Maxisch, T. & Ceder, G. Configurational electronic entropy and the phase diagram of mixed-valence oxides: The case of Li_xFePO_4. *Phys. Rev.*

Lett. **97**, 155704 (2006).
17. Zhou, F., Marianetti, C., Cococcioni, M., Morgan, D. & Ceder, G. Phase separation in Li_xFePO_4 induced by correlation effects. *Phys Rev B* **69**, 201101 (2004).
18. Gu, L. *et al.* Direct Observation of Lithium Staging in Partially Delithiated $LiFePO_4$ at Atomic Resolution. *J Am Chem Soc* **133**, 4661–4663 (2011).
19. Suo, L. *et al.* Highly ordered staging structural interface between $LiFePO_4$ and $FePO_4$. *Phys Chem Chem Phys* **14**, 5363–5367 (2012).
20. Herle, P., Ellis, B., Coombs, N. & Nazar, L. Nano-network electronic conduction in iron and nickel olivine phosphates. *Nat Mater* **3**, 147–152 (2004).
21. Ellis, B. *et al.* Nanostructured materials for lithium-ion batteries: Surface conductivity vs. bulk ion/electron transport. *Faraday Discuss* **134**, 119–141 (2007).
22. Delacourt, C., Wurm, C., Laffont, L., Leriche, J. & Masquelier, C. Electrochemical and electrical properties of Nb- and/or C-containing $LiFePO_4$ composites. *Solid State Ionics* **177**, 333–341 (2006).
23. Ong, S. P., Wang, L., Kang, B. & Ceder, G. Li-Fe-P-O_2 phase diagram from first principles calculations. *Chem Mater* **20**, 1798–1807 (2008).
24. Kim, D.-K. *et al.* Effect of synthesis conditions on the properties of $LiFePO_4$ for secondary lithium batteries. *J Power Sources* **159**, 237–240 (2006).
25. Belharouak, I., Johnson, C. & Amine, K. Synthesis and electrochemical analysis of vapor-deposited carbon-coated $LiFePO_4$. *Electrochem Commun* **7**, 983–988 (2005).
26. Hamelet, S. *et al.* The effects of moderate thermal treatments under air on $LiFePO_4$-based nano powders. *J Mater Chem* **19**, 3979–3991 (2009).
27. Kayyar, A., Qian, H. & Luo, J. Surface adsorption and disordering in $LiFePO_4$ based battery cathodes. *Appl Phys Lett* **95**, 221905 (2009).
28. Xun, S., Chong, J., Song, X., Liu, G. & Battaglia, V. S. $Li_4P_2O_7$ modified high performance $Li_3V_2(PO_4)_3$ cathode material. *J Mater Chem* **22**, 15775 (2012).
29. Van der Ven, A., Garikipati, K., Kim, S. & Wagemaker, M. The Role of Coherency Strains on Phase Stability in Li_xFePO_4: Needle Crystallites Minimize Coherency Strain and Overpotential. *J Electrochem Soc* **156**, A949 (2009).
30. Wagemaker, M., Mulder, F. M. & Van der Ven, A. The Role of Surface and Interface Energy on Phase Stability of Nanosized Insertion Compounds. *Adv Mater* **21**, 2703–+ (2009).
31. Meethong, N., Huang, H.-Y. S., Carter, W. C. & Chiang, Y.-M. Size-dependent lithium miscibility gap in nanoscale $Li_{1-x}FePO_4$. *Electrochem Solid St* **10**, A134–A138 (2007).
32. Maxisch, T. & Ceder, G. Elastic properties of olivine Li_xFePO_4 from first principles. *Phys Rev B* **73**, 174112 (2006).
33. Chen, G., Song, X. & Richardson, T. J. Electron Microscopy Study of the $LiFePO_4$ to $FePO_4$ Phase Transition. *Electrochem Solid St* **9**, A295 (2006).

34. Tan, H. J., Dodd, J. L. & Fultz, B. Thermodynamic and Kinetic Stability of the Solid Solution Phase in Nanocrystalline Li_xFePO_4. *J Phys Chem C* **113**, 20527–20530 (2009).
35. Yamada, A., Chung, S. & Hinokuma, K. Optimized $LiFePO_4$ for lithium battery cathodes. *J Electrochem Soc* **148**, A224–A229 (2001).
36. Huang, H., Yin, S. & Nazar, L. Approaching theoretical capacity of $LiFePO_4$ at room temperature at high rates. *Electrochem Solid St* **4**, A170–A172 (2001).
37. Ravet, N. *et al.* Electroactivity of natural and synthetic triphylite. *J Power Sources* **97-8**, 503–507 (2001).
38. Chung, S., Bloking, J. & Chiang, Y. Electronically conductive phospho-olivines as lithium storage electrodes. *Nat Mater* **1**, 123–128 (2002).
39. Johns, P. A., Roberts, M. R., Wakizaka, Y., Sanders, J. H. & Owen, J. R. How the electrolyte limits fast discharge in nanostructured batteries and supercapacitors. *Electrochem Commun* **11**, 2089–2092 (2009).
40. Takahashi, M., Tobishima, S., Takei, K. & Sakurai, Y. Reaction behavior of $LiFePO_4$ as a cathode material for rechargeable lithium batteries. *Solid State Ionics* **148**, 283–289 (2002).
41. Yu, D. Y. W. *et al.* Study of $LiFePO_4$ by Cyclic Voltammetry. *J Electrochem Soc* **154**, A253–A257 (2007).
42. Prosini, P., Lisi, M., Zane, D. & Pasquali, M. Determination of the chemical diffusion coefficient of lithium in LiFePO4. *Solid State Ionics* **148**, 45–51 (2002).
43. Zhu, Y. & Wang, C. Galvanostatic Intermittent Titration Technique for Phase-Transformation Electrodes. *J Phys Chem C* **114**, 2830–2841 (2010).
44. Franger, S., Le Cras, F., Bourbon, C. & Rouault, H. $LiFePO_4$ synthesis routes for enhanced electrochemical performance. *Electrochem Solid St* **5**, A231–A233 (2002).
45. Liu, H. *et al.* Kinetic study on $LiFePO_4$/C nanocomposites synthesized by solid state technique. *J Power Sources* **159**, 717–720 (2006).
46. Zhu, Y.-R. *et al.* Kinetic study on $LiFePO_4$-positive electrode material of lithium-ion battery. *Ionics* **17**, 437–441 (2011).
47. Morgan, D., Van der Ven, A. & Ceder, G. Li conductivity in Li_xMPO_4 (M = Mn, Fe, Co, Ni) olivine materials. *Electrochem Solid St* **7**, A30–A32 (2004).
48. Islam, M., Driscoll, D., Fisher, C. & Slater, P. Atomic-scale investigation of defects, dopants, and lithium transport in the $LiFePO_4$ olivine-type battery material. *Chem Mater* **17**, 5085–5092 (2005).
49. Nishimura, S.-I. *et al.* Experimental visualization of lithium diffusion in Li_xFePO_4. *Nat Mater* **7**, 707–711 (2008).
50. Sugiyama, J. *et al.* Magnetic and diffusive nature of $LiFePO_4$ investigated by muon spin rotation and relaxation. *Phys Rev B* **84**, (2011).
51. Amin, R., Maier, J., Balaya, P., Chen, D. P. & Lin, C. T. Ionic and electronic transport in single crystalline $LiFePO_4$ grown by optical floating zone technique. *Solid State Ionics* **179**, 1683–1687 (2008).

52. Delacourt, C. *et al.* Toward understanding of electrical limitations (electronic, ionic) in $LiMPO_4$ (M = Fe, Mn) electrode materials. *J Electrochem Soc* **152**, A913–A921 (2005).
53. Maxisch, T., Zhou, F. & Ceder, G. Ab initio study of the migration of small polarons in olivine Li_xFePO_4 and their association with lithium ions and vacancies. *Phys Rev B* **73**, 104301 (2006).
54. Takahashi, Y., Kijima, N., Tokiwa, K., Watanabe, T. & Akimoto, J. Single-crystal synthesis, structure refinement and electrical properties of $Li_{0.5}CoO_2$. *J Phys-Condens Mat* **19**, 436202 (2007).
55. Seid, K. A. *et al.* Multiscale electronic transport mechanism and true conductivities in amorphous carbon–$LiFePO_4$ nanocomposites. *J Mater Chem* **22**, 2641 (2012).
56. Amin, R., Balaya, P. & Maier, J. Anisotropy of electronic and ionic transport in $LiFePO_4$ single crystals. *Electrochem Solid St* **10**, A13–A16 (2007).
57. Tan, H. & Fultz, B. Rapid Electron Dynamics at Fe Atoms in Nanocrystalline $Li_{0.5}FePO_4$ Studied by Mössbauer Spectrometry. *J Phys Chem C* **115**, 7787–7792 (2011).
58. Shi, S. *et al.* Enhancement of electronic conductivity of $LiFePO_4$ by Cr doping and its identification by first-principles calculations. *Phys Rev B* **68**, 195108 (2003).
59. Sun, Y., Lu, X., Xiao, R., Li, H. & Huang, X. Kinetically Controlled Lithium-Staging in Delithiated $LiFePO_4$ Driven by the Fe Center Mediated Interlayer Li–Li Interactions. *Chem Mater* **24**, 4693–4703 (2012).
60. Dodd, J., Yazami, R. & Fultz, B. Phase diagram of $Li_{(x)}FePO_4$. *Electrochem Solid St* **9**, A151–A155 (2006).
61. Srinivasan, V. & Newman, J. Discharge model for the lithium iron-phosphate electrode. *J Electrochem Soc* **151**, A1517–A1529 (2004).
62. Andersson, A. & Thomas, J. The source of first-cycle capacity loss in $LiFePO_4$. *J Power Sources* **97-8**, 498–502 (2001).
63. Meethong, N., Huang, H.-Y. S., Speakman, S. A., Carter, W. C. & Chiang, Y.-M. Strain accommodation during phase transformations in olivine-based cathodes as a materials selection criterion for high-power rechargeable batteries. *Adv Funct Mater* **17**, 1115–1123 (2007).
64. Laffont, L. *et al.* Study of the $LiFePO_4/FePO_4$ two-phase system by high-resolution electron energy loss spectroscopy. *Chem Mater* **18**, 5520–5529 (2006).
65. Ramana, C. V., Mauger, A., Gendron, F., Julien, C. M. & Zaghib, K. Study of the Li-insertion/extraction process in $LiFePO_4/FePO_4$. *J Power Sources* **187**, 555–564 (2009).
66. Woodford, W. H., Carter, W. C. & Chiang, Y.-M. Design Criteria for Electrochemical Shock Resistant Battery Electrodes. *Energ Environ Sci* – (2012).doi:10.1039/c2ee21874g
67. Woodford, W. H., Chiang, Y.-M. & Carter, W. C. 'Electrochemical Shock' of Intercalation Electrodes: A Fracture Mechanics Analysis. *J Electrochem Soc*

157, A1052 (2010).
68. Delmas, C., Maccario, M., Croguennec, L., Le Cras, F. & Weill, F. Lithium deintercalation in $LiFePO_4$ nanoparticles via a domino-cascade model. *Nat Mater* **7**, 665–671 (2008).
69. Balluffi, R. W., Allen, S. M. & Carter, W. C. *Kinetics of Materials.* (Wiley-Interscience, 2005).
70. Porter, D. A. & Easterling, K. E. *Phase Transformations in Metals and Alloys, Third Edition (Revised Reprint).* (CRC Press, 1992).
71. Hong, J., Wang, C. & Kasavajjula, U. Kinetic behavior of $LiFeMgPO_4$ cathode material for Li-ion batteries. *J Power Sources* **162**, 1289–1296 (2006).
72. Allen, J. L., Jow, T. R. & Wolfenstine, J. Analysis of the $FePO_4$ to $LiFePO_4$ phase transition. *J Solid State Electr* **12**, 1031–1033 (2008).
73. Allen, J. L., Jow, T. R. & Wolfenstine, J. Kinetic study of the electrochemical $FePO_4$ to $LiFePO_4$ phase transition. *Chem Mater* **19**, 2108–2111 (2007).
74. Oyama, G., Yamada, Y., Natsui, R.-I., Nishimura, S.-I. & Yamada, A. Kinetics of Nucleation and Growth in Two-Phase Electrochemical Reaction of Li_xFePO_4. *J Phys Chem C* **116**, 7306–7311 (2012).
75. Allen, J. L., Jow, T. R. & Wolfenstine, J. Correction to Kinetic Study of the Electrochemical $FePO_4$to $LiFePO_4$ Phase Transition. *Chem Mater* **24**, 1400–1400 (2012).
76. Ranganathan, S. & Heimendahl, M. The three activation energies with isothermal transformations: applications to metallic glasses. *J Mater Sci* **16**, 2401–2404 (1981).
77. Avrami, M. Kinetics of Phase Change. I General Theory. *J. Chem. Phys.* **7**, 1103 (1939).
78. Brunetti, G. *et al.* Confirmation of the Domino-Cascade Model by $LiFePO_4/FePO_4$ Precession Electron Diffraction. *Chem Mater* **23**, 4515–4524 (2011).
79. Dreyer, W. *et al.* The thermodynamic origin of hysteresis in insertion batteries. *Nat Mater* **9**, 448–453 (2010).
80. Meethong, N. *et al.* Electrochemically Induced Phase Transformation in Nanoscale Olivines $Li_{1-x}MPO_4$ (M = Fe, Mn). *Chem Mater* **20**, 6189–6198 (2008).
81. Tang, M. *et al.* Model for the Particle Size, Overpotential, and Strain Dependence of Phase Transition Pathways in Storage Electrodes: Application to Nanoscale Olivines. *Chem Mater* **21**, 1557–1571 (2009).
82. Tang, M., Carter, W. C. & Chiang, Y.-M. Electrochemically Driven Phase Transitions in Insertion Electrodes or Lithium-Ion Batteries: Examples in Lithium Metal Phosphate Olivines. *Annu Rev Mater Res* **40**, 501–529 (2010).
83. Kao, Y.-H. *et al.* Overpotential-Dependent Phase Transformation Pathways in Lithium Iron Phosphate Battery Electrodes. *Chem Mater* **22**, 5845–5855 (2010).
84. Leriche, J. B. *et al.* An Electrochemical Cell for Operando Study of Lithium Batteries Using Synchrotron Radiation. *J Electrochem Soc* **157**, A606–A610

(2010).
85. Ouvrard, G., Zerrouki, M., Masquelier, C. & Morcrette, M. *Mapping of a Battery Electrode.* (2010).
86. Web of Knowledge - IP & Science - Thomson Reuters. *wokinfo.com* at <http://wokinfo.com/>
87. Malik, R., Zhou, F. & Ceder, G. Phase diagram and electrochemical properties of mixed olivines from first-principles calculations. *Phys Rev B* **79**, 214201 (2009).
88. Chen, Z. & Dahn, J. Reducing carbon in $LiFePO_4$/C composite electrodes to maximize specific energy, volumetric energy, and tap density. *J Electrochem Soc* **149**, A1184–A1189 (2002).
89. Malik, R., Burch, D., Bazant, M. & Ceder, G. Particle Size Dependence of the Ionic Diffusivity. *Nano Lett* **10**, 4123–4127 (2010).
90. Malik, R., Zhou, F. & Ceder, G. Kinetics of non-equilibrium lithium incorporation in $LiFePO_4$. *Nat Mater* **10**, 587–590 (2011).
91. Born, M. & Oppenheimer, R. Zur Quantentheorie der Molekeln. *Ann. Phys.* **389**, 457–484 (1927).
92. Martin, R. M. *Electronic Structure: Basic Theory and Practical Methods (0521782856).* (Cambridge University Press, 2005).
93. Hohenberg, P. Inhomogeneous Electron Gas. *Phys. Rev.* **136**, B864–B871 (1964).
94. Kohn, W. & Sham, L. J. Self-Consistent Equations Including Exchange and Correlation Effects. *Phys. Rev.* **140**, A1133–A1138 (1965).
95. Anisimov, V. I., Zaanen, J. & Andersen, O. K. Band theory and Mott insulators: Hubbard U instead of Stoner I. *Phys Rev B* **44**, 943–954 (1991).
96. Anisimov, V. I., Solovyev, I. V. & Korotin, M. A. Density-functional theory and NiO photoemission spectra. *Phys Rev B* **48**, 16929–16934 (1993).
97. Liechtenstein, A. I. & Zaanen, J. Density-functional theory and strong interactions: Orbital ordering in Mott-Hubbard insulators. *Phys Rev B* **52**, R5467–R5470 (1995).
98. Ceder, G., Aydinol, M. K. & Kohan, A. F. Application of first-principles calculations to the design of rechargeable Li-batteries. *Computational Materials Science* **8**, 161–169 (1997).
99. Wang, L., Maxisch, T. & Ceder, G. A First-Principles Approach to Studying the Thermal Stability of Oxide Cathode Materials. *Chem Mater* **19**, 543–552 (2007).
100. Sanchez, J. M., Ducastelle, F. & Gratias, D. Generalized cluster description of multicomponent systems. *Physica A: Statistical Mechanics and its Applications* **128**, 334–350 (1984).
101. Metropolis, N., Rosenbluth, A. W., Rosenbluth, M. N., Teller, A. H. & Teller, E. Equation of State Calculations by Fast Computing Machines. *J. Chem. Phys.* **21**, 1087–1092 (1953).
102. Zhou, F., Cococcioni, M., Marianetti, C., Morgan, D. & Ceder, G. First-principles prediction of redox potentials in transition-metal compounds with

LDA+U. *Phys Rev B* **70**, (2004).
103. Zhou, F., Kang, K., Maxisch, T., Ceder, G. & Morgan, D. The electronic structure and band gap of $LiFePO_4$ and $LiMnPO_4$. *Solid State Commun* **132**, 181–186 (2004).
104. Yamada, A., Kudo, Y. & Liu, K. Phase diagram of $Li_x(Mn_yFe_{1-y})PO_4$. *J Electrochem Soc* **148**, A1153–A1158 (2001).
105. Yamada, A. *et al.* Electrochemical, Magnetic, and Structural Investigation of the $Li_x(Mn_yFe_{1-y})PO_4$ Olivine Phases. *Chem Mater* **18**, 804–813 (2006).
106. Yamada, A., Kudo, Y. & Liu, K. Reaction mechanism of the olivine-type $Li_x(Mn_{0.6}Fe_{0.4})PO_4$. *J Electrochem Soc* **148**, A747–A754 (2001).
107. Yao, J. *et al.* Characterisation of olivine-type $LiMn_xFe_{1-x}PO_4$ cathode materials. *J Alloy Compd* **425**, 362–366 (2006).
108. Burba, C. A. & Frech, R. Local structure in the Li-ion battery cathode material $Li_x(Mn_yFe_{1-y})PO_4$. *J Power Sources* **172**, 870–876 (2007).
109. Li, G., Azuma, H. & Tohda, M. Optimized $LiMn_yFe_{1-y}PO_4$ as the Cathode for Lithium Batteries. *J Electrochem Soc* **149**, A743 (2002).
110. Li, G., Kudo, Y., Liu, K.-Y., Azuma, H. & Tohda, M. X-Ray Absorption Study of $Li_xMn_yFe_{1-y}PO_4$ ($0 \leq x \leq 1$). *J Electrochem Soc* **149**, A1414 (2002).
111. Molenda, J. *et al.* Diffusional mechanism of deintercalation in $LiFe_{1-y}Mn_yPO_4$ cathode material. *Solid State Ionics* **177**, 2617–2624 (2006).
112. Nakamura, T. *et al.* Apparent diffusion constant and electrochemical reaction in $LiFe_{1-x}Mn_xPO_4$ olivine cathodes. *J Electrochem Soc* **154**, A1118–A1123 (2007).
113. Nakamura, T. *et al.* Electrochemical study on Mn^{2+}-substitution in $LiFePO_4$ olivine compound. *J Power Sources* **174**, 435–441 (2007).
114. Shin, Y.-J., Kim, J.-K., Cheruvally, G., Ahn, J.-H. & Kim, K.-W. $Li(Mn_{0.4}Fe_{0.6})PO4$ cathode active material: Synthesis and electrochemical performance evaluation. *Journal of Physics and Chemistry of Solids* **69**, 1253–1256 (2008).
115. Wang, D., Wang, Z., Huang, X. & Chen, L. Continuous solid solutions $LiFe_{1-x}Co_xPO_4$ and its electrochemical performance. *J Power Sources* **146**, 580–583 (2005).
116. Wang, X. J. *et al.* Li-storage in $LiFe_{1/4}Mn_{1/4}Co_{1/4}Ni_{1/4}PO_4$ solid solution. *Electrochem Commun* **10**, 1347–1350 (2008).
117. Chen, J. & Whittingham, M. Hydrothermal synthesis of lithium iron phosphate. *Electrochem Commun* **8**, 855–858 (2006).
118. Chen, J., Wang, S. & Whittingham, M. S. Hydrothermal synthesis of cathode materials. *J Power Sources* **174**, 442–448 (2007).
119. Yamada, A., Koizumi, H., Sonoyama, N. & Kanno, R. Phase change in Li_xFePO_4. *Electrochem Solid St* **8**, A409–A413 (2005).
120. Delacourt, C., Poizot, P., Tarascon, J. & Masquelier, C. The existence of a temperature-driven solid solution in Li_xFePO_4 for $0 \leq x \leq 1$. *Nat Mater* **4**, 254–260 (2005).
121. Tepesch, P., Garbulsky, G. & Ceder, G. Model for Configurational

Thermodynamics in Ionic Systems. *Phys. Rev. Lett.* **74**, 2272–2275 (1995).
122. Landau, D. P. & Binder, K. *A Guide to Monte Carlo Simulations in Statistical Physics*. (Cambridge University Press, 2009).
123. Yonemura, M., Yamada, A., Takei, Y., Sonoyama, N. & Kanno, R. Comparative kinetic study of olivine Li_xMPO_4 (M = Fe, Mn). *J Electrochem Soc* **151**, A1352–A1356 (2004).
124. Berker, A. N. Absence of temperature-driven first-order phase transitions in systems with random bonds (invited). *J. Appl. Phys.* **70**, 5941–5945 (1991).
125. Nihat Berker, A. Critical behavior induced by quenched disorder. *Physica A: Statistical Mechanics and its Applications* **194**, 72–76 (1993).
126. Hui, K. & Berker, A. Random-field mechanism in random-bond multicritical systems. *Phys. Rev. Lett.* **62**, 2507–2510 (1989).
127. Aizenman, M. & Wehr, J. Rounding of first-order phase transitions in systems with quenched disorder. *Phys. Rev. Lett.* **62**, 2503–2506 (1989).
128. Delacourt, C., Poizot, P., Levasseur, S. & Masquelier, C. Size effects on carbon-free $LiFePO_4$ powders. *Electrochem Solid St* **9**, A352–A355 (2006).
129. Yamada, A., Yonemura, M., Takei, Y., Sonoyama, N. & Kanno, R. Fast charging $LiFePO_4$. *Electrochem Solid St* **8**, A55–A58 (2005).
130. Chen, D. P., Maljuk, A. & Lin, C. T. Floating zone growth of lithium iron (II) phosphate single crystals. *Journal of Crystal Growth* **284**, 86–90 (2005).
131. Fisher, C. A. J., Prieto, V. M. H. & Islam, M. S. Lithium battery materials $LiMPO_4$ (M = Mn, Fe, Co, and Ni): Insights into defect association, transport mechanisms, and doping behavior. *Chem Mater* **20**, 5907–5915 (2008).
132. Chung, S.-Y., Choi, S.-Y., Yamamoto, T. & Ikuhara, Y. Atomic-scale visualization of antisite defects in $LiFePO_4$. *Phys. Rev. Lett.* **100**, 125502 (2008).
133. Chung, S.-Y., Choi, S.-Y., Yamamoto, T. & Ikuhara, Y. Orientation-Dependent Arrangement of Antisite Defects in Lithium Iron(II) Phosphate Crystals. *Angew Chem Int Edit* **48**, 543–546 (2009).
134. Yamada, A. *et al.* Room-temperature miscibility gap in Li_xFePO_4. *Nat Mater* **5**, 357–360 (2006).
135. Heinisch, H. L., Trinkaus, H. & Singh, B. N. Kinetic Monte Carlo studies of the reaction kinetics of crystal defects that diffuse one-dimensionally with occasional transverse migration. *Journal of Nuclear Materials* **367-370**, 332–337 (2007).
136. Boyce, J. B. & Mikkelsen, J. C., Jr. Anisotropic conductivity in a channel-structured superionic conductor: $Li_2Ti_3O_7$. *Solid State Commun* **31**, 741–745 (1979).
137. Reimers, J. N. Electrochemical and In Situ X-Ray Diffraction Studies of Lithium Intercalation in Li_xCoO_2. *J Electrochem Soc* **139**, 2091 (1992).
138. Ohzuku, T. & Makimura, Y. Layered Lithium Insertion Material of $LiCo_{1/3}Ni_{1/3}Mn_{1/3}O_2$ for Lithium-Ion Batteries. *Chemistry Letters* **30**, 642–643 (2001).
139. Kim, D.-H. & Kim, J. Synthesis of $LiFePO_4$ Nanoparticles in Polyol Medium

and Their Electrochemical Properties. *Electrochem Solid St* **9**, A439 (2006).
140. Wang, C., Kasavajjula, U. S. & Arce, P. E. A discharge model for phase transformation electrodes: Formulation, experimental validation, and analysis. *J Phys Chem C* **111**, 16656–16663 (2007).
141. Laffont, L. *et al.* Study of the $LiFePO_4/FePO_4$ two-phase system by high-resolution electron energy loss spectroscopy. *Chem Mater* **18**, 5520–5529 (2006).
142. Delacourt, C., Rodriguez-Carvajal, J., Schmitt, B., Tarascon, J. & Masquelier, C. Crystal chemistry of the olivine-type Li_xFePO_4 system ($0 \leq x \leq 1$). *Solid State Sci* **7**, 1506–1516 (2005).
143. Chen, G., Song, X. & Richardson, T. J. Metastable solid-solution phases in the $LiFePO_4/FePO_4$ system. *J Electrochem Soc* **154**, A627–A632 (2007).
144. Chang, H.-H. *et al.* Study on dynamics of structural transformation during charge/discharge of $LiFePO_4$ cathode. *Electrochem Commun* **10**, 335–339 (2008).
145. Dominko, R., Conte, D. E., Hanzel, D., Gaberscek, M. & Jamnik, J. Impact of synthesis conditions on the structure and performance of Li_2FeSiO_4. *J Power Sources* **178**, 842–847 (2008).
146. Lee, K. T., Kan, W. H. & Nazar, L. F. Proof of Intercrystallite Ionic Transport in $LiMPO_4$ Electrodes (M = Fe, Mn). *J Am Chem Soc* **131**, 6044–+ (2009).
147. Matsui, H., Nakamura, T., Kobayashi, Y., Tabuchi, M. & Yamada, Y. Open-circuit voltage study on $LiFePO_4$ olivine cathode. *J Power Sources* **195**, 6879–6883 (2010).
148. Van der Ven, A. & Wagemaker, M. Effect of surface energies and nano-particle size distribution on open circuit voltage of Li-electrodes. *Electrochem Commun* **11**, 881–884 (2009).
149. Gaberscek, M., K zma, M. & Jamnik, J. Electrochemical kinetics of porous, carbon-decorated $LiFePO_4$ cathodes: separation of wiring effects from solid state diffusion. *Phys Chem Chem Phys* **9**, 1815 (2007).
150. Dominko, R., Gaberscek, M., Bele, A., Mihailovic, D. & Jamnik, J. Carbon nanocoatings on active materials for Li-ion batteries. *J Eur Ceram Soc* **27**, 909–913 (2007).
151. Wang, J. & Sun, X. Understanding and recent development of carbon coating on $LiFePO_4$ cathode materials for lithium-ion batteries. *Energ Environ Sci* **5**, 5163–5185 (2012).
152. Li, H. & Zhou, H. Enhancing the performances of Li-ion batteries by carbon-coating: present and future. *Chem Commun* (2011).
153. Gaberscek, M., Dominko, R. & Jamnik, J. Is small particle size more important than carbon coating? An example study on $LiFePO_4$ cathodes. *Electrochem Commun* **9**, 2778–2783 (2007).
154. Adams, S. & Rao, R. P. Simulated defect and interface engineering for high power Li electrode materials. *Solid State Ionics* **184**, 57–61 (2011).
155. Liu, J., Kunz, M., Chen, K., Tamura, N. & Richardson, T. J. Visualization of

Charge Distribution in a Lithium Battery Electrode. *J. Phys. Chem. Lett.* **1**, 2120–2123 (2010).
156. Shin, H. C. *et al.* Asymmetry between charge and discharge during high rate cycling in $LiFePO_4$ - In situ X-ray diffraction study. *Electrochem Commun* **10**, 536–540 (2008).